SIMULATION OF DUCTILE DAMAGE USING PONTE CASTAÑEDA MICROMECHANICAL MODEL

Thesis by

Hemanth Janarthanam
Matriculation Number - 3010440

Submitted to Institute of Mechanics in partial fulfilment of the requirements
for the Degree of
Master of Science in Computational Mechanics

Offen im Denken

Universität Duisburg Essen

In collaboration with

Fraunhofer Institute for Mechanics of Materials

IWM Report Number: 1406/2015

Thesis committee:

Dr.-Ing. Dominik Brands, UDE, Institute of Mechanics

apl. Prof. Dr.-Ing. Joachim Bluhm, UDE, Professor at Institute of Mechanics

Abstract

Most metals used in structural applications often exhibit ductile damage characteristics, where the crack propagates through the material with accumulation of plastic strain. Microscopically ductile damage consists of void nucleation, void growth and void coalescence. In metal forming process, ductile damage is often a limiting factor. In this work, micromechanically motivated constitutive model proposed by Ponte Castañeda et al. [42] (VAR) for elastoplastic porous material is used to simulate ductile damage in standard bulk forming experiments, namely upsetting test, cylinder with circular notch upsetting test and uniaxial tensile test. The ability of the model to predict void growth with its shape change is analysed. Also, the influence of initial shape of the void on evolution of porosity under different stress triaxialities are studied. Isotropic hardening laws, Thomason based coalescence criteria and new strain induced void nucleation formulation are implemented to the original constitutive equation. The results obtained from VAR model are compared to Gurson model and other phenomenological ductile damage criteria proposed in literature.

Thesis Supervisors

First Supervisor:	Dr.-Ing. Dominik Brands, UDE
Second Supervisor:	apl. Prof. Dr.-Ing. Joachim Bluhm, UDE
External Supervisors:	Dr. Maksim Zapara, Fraunhofer IWM
	Dr. Alexander Butz, Fraunhofer IWM

Acknowledgements

I wish to express my deepest gratitude to my supervisors Dr. Maksim Zapara and Dr. Alexander Butz at Fraunhofer Institute for Mechanics of Materials, and to Dr. Dominik Brands and Professor Dr. Joachim Bluhm at Institute of Mechanics, UDE for their support and guidance during my thesis. I would like to specially thank Dr. Zapara and Dr. Butz for their consistent and continuous encouragement, patience and insightful comments all the way along my thesis. I am grateful to Dr. Dirk Helm and the team for giving me the opportunity to work at Fraunhofer IWM and for valuable discussions. I would also like to thank Professor Bluhm for introducing me to Continuum Mechanics and Dr.Brands for his lectures on Heterogeneous materials, and for advices during my Thesis. I also acknowledge the support from Dr. Ingo Schmidt and Dr. Andreas Trondl of IWM for beneficial inputs and the subroutines, without which the thesis work would have been next to impossible.

I am very grateful to Eva for providing me with the experimental results, helping me with numerical simulations and for putting up with my silly questions. I wish to acknowledge the constant support extended by Rohith in understanding the numerical implementations, the material model and explaining Plasticity in simple words. I would also like to thank my institute roommates Lukas and Maksim for proving me with a good environment to work at. I owe gratitudes to lot of people, that this acknowledgement section cannot be complete. Therefore, I hope to implicitly thank the rest of the team at Fraunhofer IWM and Institute of Mechanics, Universitaät Duisburg Essen.

Finally, but certainly not least, I would like to acknowledge all my friends at Freiburg, Essen and far away friends in India, and my family for encouraging me to pursue my interests and to have made my life memorable. In particular, I would like to express my gratitude to my parents and my sister, for the immense love and care.

Versicherung an Eides Statt

Ich versichere an Eides durch meine untenstehende Unterschrift,

- dass ich die vorliegende Arbeit - mit Ausnahme der Anleitung durch die Betreuer selbstständig ohne frembe Hilfe angefertigt habe und
- dass ich alle Stellen, die wörtlich oder annähernd wörtlich aus fremden Quellen entnommen sind, entsprechend als Zitate gekennzeichnet habe und
- dass ich ausschliesslich die angegebenen Quellen (Literatur, Internetseiten, sonstige Hilfsmittel) verwendet habe und
- dass ich alle enstsprechenden Angaben nach bestem Wissen und Gewissen vorgenommen habe, dass sie der Wahrheit entsprechen und dass ich nichts verschwiegen habe.

Mir ist bekannt, dass ein falsche Versicherung an Eides Statt nach §156 und nach §163 Abs. 1 des Strafgesetzbuches mit Freiheitsstrafe oder Geldstrafe bestraft wird.

Ort, Datum

Unterschrift

Declaration

I declare that this thesis, which I submit to Universität Duisburg Essen in consideration of the award of Master of Science in Computational Mechanics degree is my own personal effort. Where any of the content presented is the result of input or data from a related collaborative research programme this is duly acknowledged in the text such that it is possible to ascertain how much of the work is my own. I have not already obtained a degree in Universität Duisburg Essen or elsewhere on the basis of this work.

Furthermore, I took reasonable care to ensure that the work is original, and, to the best of my knowledge, does not breach copyright law, and has not been taken from other sources except where such work has been cited and acknowledged within the text.

Place, Date

Signature

Contents

List of Figures

List of Tables

List of Symbols

$\bar{\boldsymbol{\sigma}}$	Volumetric average stress
$\bar{\boldsymbol{\varepsilon}}$	Volumetric average strain
$\dot{\boldsymbol{\sigma}}$	Rate of Cauchy stress tensor
$\boldsymbol{\mathcal{C}}$	Spin concentration tensor
$\boldsymbol{\Pi}$	Eshelby's rotation tensor
$\boldsymbol{\sigma}$	Cauchy stress tensor
$\boldsymbol{\sigma}^*$	Eigen stress
$\boldsymbol{\tau}$	Kirchhoff stress tensor
$\boldsymbol{\varepsilon}^*$	Eigen strain
$\boldsymbol{\varepsilon}^e$	Elastic strain
$\boldsymbol{\varepsilon}^p$	Plastic strain
$\boldsymbol{A}$	Strain rate concentration tensor
$\boldsymbol{C}$	Elasticity tensor
$\boldsymbol{D}$	Rate of deformation tensor
$\boldsymbol{D}^e$	elastic rate of deformation tensor
$\boldsymbol{D}^p$	plastic rate of deformation tensor
$\boldsymbol{I}$	Second order identity tensor
$\boldsymbol{J}$	Deviatoric part of fourth order identity tensor
$\boldsymbol{K}$	Volumetric part of fourth order identity tensor
$\boldsymbol{N}$	Flow vector
$\boldsymbol{n}^{(1)}$	Unit vector along a principal axis of ellipsoidal void
$\boldsymbol{n}^{(2)}$	Unit vector along a principal axis of ellipsoidal void

$\boldsymbol{n}^{(3)}$	Unit vector along a principal axis of ellipsoidal void
$\boldsymbol{Q}$	Orthogonal Tensor
$\boldsymbol{R}$	Rotation tensor
$\boldsymbol{S}$	Eshelby's tensor
$\boldsymbol{S}$	Second Piola-Kirchhoff stress tensor
$\boldsymbol{s}$	Deviatoric stress tensor
$\boldsymbol{W}$	Spin tensor
χ	Distance between ligaments
$\dot{\Lambda}$	Plastic multiplier
κ	Elastic bulk modulus
$\mathbb{I}$	Symmetric fourth order identity tensor
μ	Elastic shear modulus
ν	Poisson's ratio
$\overset{\circ}{\boldsymbol{\sigma}}$	Objective rate of Cauchy stress tensor
$\overset{\Delta}{\boldsymbol{\sigma}}$	Green-Naghdi rate of Cauchy stress tensor
$\overset{\nabla}{\boldsymbol{\sigma}}$	Jaumann rate of Cauchy stress tensor
Φ	Yield function
σ_1	1st Principal stress
σ_2	2nd Principal stress
σ_3	3rd Principal stress
σ_{eq}	Equivalent or von Mises stress
σ_m	Mean or Hydrostatic stress
ε^p_{eq}	Equivalent plastic strain
ε_f	Strain at failure
ε_N	Mean nucleation strain
a	semi axis length along $\boldsymbol{n}^{(1)}$ of ellipsoidal void
b	semi axis length along $\boldsymbol{n}^{(2)}$ of ellipsoidal void
c	semi axis length along $\boldsymbol{n}^{(3)}$ of ellipsoidal void

f	Total void volume fraction
f^*	Tveergard and Needleman coalescence parameter
f_c	Critical void volume fraction
f_F	Void volume fraction at fracture
f_g	Void volume fraction due to growth
f_N	Void volume fraction to be nucleated, void nucleation function
f_n	Nucleated void volume fraction
I_1	1st Invariant of Cauchy stress
I_2	2nd Invariant of Cauchy stress
I_3	3rd Invariant of Cauchy stress
J_1	1st Invariant of deviatoric stress
J_2	2nd Invariant of deviatoric stress
J_3	3rd Invariant of deviatoric stress
S_N	Standard deviation void nucleation function
T	Stress triaxiality
w_1	Ellipsoidal void aspect ratio
w_2	Ellipsoidal void aspect ratio

Chapter 1

Introduction

1.1 Introduction

With the advancement in metal working over the last century, the use of metals in structures have exponentially increased. However, it is observed that these structures do not always fullfill the requirements and fail unexpectedly, resulting in monetary losses, and more importantly causes injuries and in some cases loss of human life. To alleviate the amount of damage, a need arises to understand these failure mechanisms to be able to design reliable structures.

Failures can occur due to various reasons, like uncertainties in loading or environment, inadequate design, material defects or improper maintenance. Typically, failure begins with formation of microscopic defects (damage) which then leads to macrocracks and eventually to breakage (fracture). With recent technologies in material science, it is possible to alter the microstructure of metals to strengthen them. But, this process increases the brittleness of the material, and results in catastrophic failures with little warning. Therefore, prediction of damage and fracture is of acute importance to be able to avoid unforeseen incidents.

In metal forming processes, occurrence of failure determines the limit of the manufacturing process. To optimize the process, it is important to understand the failure mechanisms and the correlation between the process and material parameters in the failure occurrence. In cold forming industry, the ability of the numerical model to predict ductile failure is crucial. The complication arises due to very large plastic strains, in which the damage may localize away from the maximum critical strain. This has lead researchers to study ductile damage extensively in the last half century. However the inadequacy of experimental techniques to investigate and quantify the last stages of the failure process makes it difficult to validate the constitutive models.

The increasing experimental techniques and advancement in mechanics and applied mathematics, have collectively lead to development of numerical methods and constitutive models which are capable of predicting damage and fractures. Also, the outburst of computation capabilities, facilitates the investigation of sophisticated real life problems. Over a period of time, various constitutive models and numeri-

cal methods have been proposed in literature. But, there is no one perfect method which is suitable for all applications. Therefore, it is important to investigate them closely and choose the right method based on the application needs.

Metallurgical research have shown that, microscopically, ductile damage consists of three principal stages - void nucleation, growth and coalescence of microvoids [61]. Macroscopically, ductile damage represents a decrease in material strength. Extensive research have been carried out to understand ductile damage. Pioneering work was published by McClintock et al. [50] who analysed the evolution of an isolated cylindrical void in a ductile elastoplastic matrix to understand the role of microvoids. Various material models have been proposed in the literature to predict the influence of microvoids on material degradation, with some considering the load history. The material models can be broadly classified into - phenomenological models (Cockcroft-Latham [24], McClintock [49],[48]) and micromechanics based models (Gurson [38], GTN [63], Gologanu[33], Kailasam & Ponte Castaneda [42]).

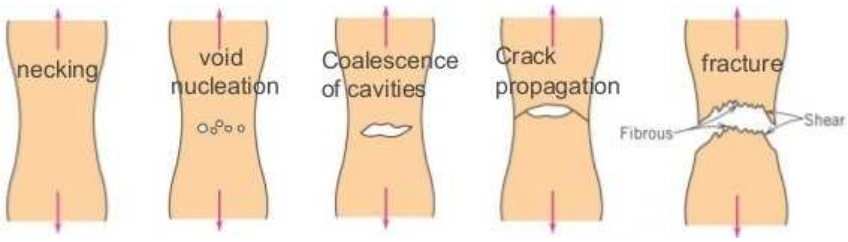

Fig. 1.1.1: Stages in Ductile damage of a moderate ductile material [1]

The observations of Rice & Tracey [57] and McClintock et al.[50] set the foundation for various micromechanics based models. Gurson [38] was the first to propose a damage based yield criterion and flow rule, for a rigid-perfectly plastic porous ductile material using the upper bound theorem of plasticity. Gurson based his approximation on micromechanical analysis of a thick spherical shell with a spherical void, subjected to hydrostatic pressure, to obtain estimates for the effective constitutive behaviour. The approximate yield function is a function of hydrostatic stress which accounts for plastic dilatancy caused by the hydrostatic components of stresses, and lead to better understanding of plastic behaviour in region of high hydrostatic stress. The proposed model accounts for damage by a porosity term, that progressively shrinks the yield surface. The evolution law for the porosity was obtained from the macroscopic continuity equations by assuming in-compressibility of the matrix phase. Gurson assumed the voids to grow spherically, hence the voids were isotropic. This model is known to be accurate for high triaxiality, where the porous material is expected to remain isotropic.

An alternate class of constitutive models for porous materials which accounts for general three-dimensional loading , including void rotation, has been developed by Ponte Castañeda & Zaidman [19] and Kailasam & Ponte Castañeda [43]. These methods were based on the variational (VAR) linear comparison homogenization

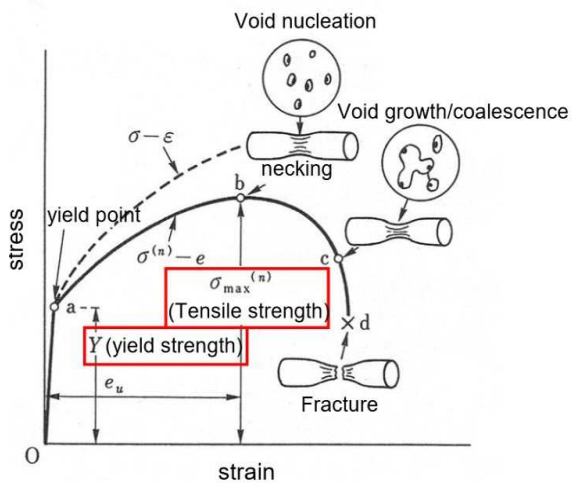

Fig. 1.1.2: Material behaviour under uniaxial tensile test [70]

principles of Ponte Castaneda [16] [17], which allows the estimation of bounds and estimates for nonlinear composites with the given classes of microstructure in terms of corresponding bounds and estimates for linear composites with the same classes of microstructure, together with the estimates of Ponte Castañeda & Willis [18] for porous linear-elastic materials with ellipsoidal microstructure. Kailasam & Ponte Castañeda [42] proposed a general constitutive theory for nonlinear composites with microstructure evolution as a consequence of finite strain boundary conditions. The computational issues in implementation of this model in a FE code was dealt by Aravas & Ponte Castaneda [4] in detail. This model gives an overly stiff predictions at high triaxialities and small porosities [25]. This limitations have been dealt with in the recent works by Danas & Ponte Castañeda [26] and Danas & Aravas [25].

Danas & Ponte Castañeda [26] made use of more accurate second order linear comparison homogenization method of Ponte Castañeda. Danas & Aravas [25] proposed a simple modification to the variational homogenization method(MVAR) for elasto-plastic, rate independent porous materials. It was shown that the MVAR model gave similar results in comparison to Gurson model at high stress triaxialities. These class of models have the advantage of accounting for void orientation and rotation, which plays a crucial role at low stress triaxialities and leads to failure of material at lower displacement values when compared to Gurson models. With the advancement in computational mechanics and numerical methods, considerable research is being carried out in the field of damage mechanics and various new models combining different existing damage models - micromechanical and/or phenomenological (like Zhou et. al. [71] , Cao et. al. [14]) are being proposed.

In this study, VAR micromechanical model proposed by Ponte Castañeda et al. is scrutinized to understand the influence of various parameters in the constitutive equation on the behaviour of the material, and to study its accuracy in predicting damage in bulk forming processes. The material model has already been implemented in ABAQUS-Explicit through VUMAT subroutine at Fraunhofer IWM and used to simulate materials with high porosity undergoing small plastic deformations. The first part of the study is to validate the subroutine for industrial steels

undergoing large deformations (plastic strain > 1.0), to solve any numerical issues encountered during the process, and to extend the subroutine to incorporate various hardening laws, Thomason based coalescence criteria, and to improve void nucleation under complex loading. The latter part of the study deals with parametric analysis of the material model, and to determine its accuracy in damage prediction by comparing the simulation results to experimental results and numerical results obtained from other damage models (micromechanical and phenomenological).

Chapter 2

Theoretical Framework

2.1 Damage Mechanism

As described in the introduction, micromechanically ductile damage consists of three stages - void nucleation, void growth and coalescence. In this section an overview of these stages and the material models which describe them are provided.

2.1.1 Void Nucleation

Void nucleation can be classified into homogeneous and heterogeneous [65]. Homogeneous nucleation occurs within the grains and does not involve precipitation or inclusions. Heterogeneous nucleation occurs at the second phase particles or inclusions. Heterogeneous nucleation is a common occurrence in engineering materials, as most of the engineering materials contain inclusions or second phase particles. Voids are reported to be nucleated by tearing the inclusion from the ductile matrix (debonding) or by cracking of the non deformable inclusion during plastic deformation. Fig.(2.1.1) shows the mechanism of void formation in Aluminum reinforced with Al_2O_3 particles [44].

The inclusions generally fail due to load shedding from matrix material to het-

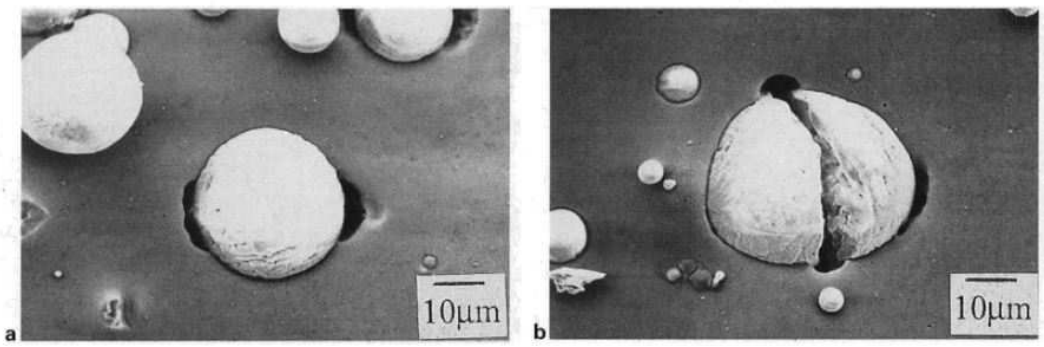

Fig. 2.1.1: a) Debonding of Inclusion b)Cracking of Inclusion in 6061 Aluminum reinforced with Al_2O_3 particles [44]

erogeneity and leads to the formation of crack perpendicular to the applied load.

Strong interface leads to formation of crack in the inclusion and weak interface lead to debonding nucleation. The nucleation mechanism is also influenced by many other parameters like size and shape of inclusion, orientation of inclusion, temperature, stress state, etc [65].

Babout et al.[6] studied the effect of matrix hardness on void nucleation mechanism by *in situ* investigation of void nucleation in *Al* matrix - pure *Al*(soft matrix) and structural *Al* alloy (hard matrix). They observed that in hard matrix, void nucleation was driven by cracking of inclusion and in soft matrix, void nucleation was due to matrix-particle decohesion.

Various models have been proposed in the literature to predict nucleation. These models follow a continuum based approach to model the average nucleation response of an alloy system by determining a critical stress, strain or energy level. Gurland and Plateau [36] were one of the first to propose an energy based nucleation model. They suggested that voids would nucleate when the elastic strain energy that could be released upon decohesion would be comparable to the energy of the surface to be generated. Further Argon et. al. [5] proved that the energy criterion is only a necessary condition, and the actual separation requires reaching the interfacial strength at the interface. They proposed a phenomenological model for void nucleation by particle matrix decohesion , where the critical interface stress can be approximated as the sum of flow and hydrostatic stress.

$$\sigma_p^{max} + \sigma_m = \min(\sigma_c^I, \sigma_c^P) \tag{2.1.1}$$

where $\sigma_{\mathrm{p}}^{max}$ is the maximum principal stress, σ_c^I is the maximum stress that the matrix-particle interface can undergo without decohesion and σ_c^P is the particle strength. This criterion was based on the assumption that inclusion is equiaxed and rigid and plastically non-deformable. Also, it did not account for particle size and shape. Various modification were proposed by Pineau et al., Lee & Mear to account for shape effects and stress concentration factor inside the particle.

Based on the works of Gurson, Gurland [37] and Needleman & Rice [52], Chu & Needleman [23] formulated a two parameter void nucleation criterion which approximately accounts for plastic stress controlled nucleation and plastic strain controlled nucleation. This formulation was based on statistics of particle spacing as discussed by Gurson [38]. Needleman & Rice [52] first proposed a two parameter void nucleation given by

$$\dot{f}_n = M\dot{\bar{\boldsymbol{\sigma}}} + N\dot{\sigma}_{kk}/3 = A\dot{\varepsilon}_{eq}^p + B\dot{\bar{\sigma}}_m \tag{2.1.2}$$

where, $\bar{\boldsymbol{\sigma}}$ is the tensile flow yield stress of the matrix material which can be correlated to equivalent plastic strain. If the nucleation of voids is exclusively controlled by equivalent plastic strain, then $B = 0$ and if the nucleation depends only on maximum stress transmitted across the particle-matrix interface, as suggested by Argon [5], an approximation can be obtained when $A \approx B$. Chu & Needleman proposed formulations for the constants A & B. For the case of strain controlled nucle-

ation, they assumed that there is a mean equivalent plastic strain for nucleation ε_N, and that the nucleation strain is distributed in a normal fashion about the mean. Thus, $B = 0$ and,

$$A = \frac{f_N}{S_N\sqrt{2\pi}}\exp\left[-\frac{1}{2}\left(\frac{\varepsilon^p_{eq} - \varepsilon_N}{S_N}\right)^2\right] \tag{2.1.3}$$

S_N is the standard deviation of the distribution and f_N is the total void volume nucleated in consistent with the void volume fraction of the particles. By varying S_N, a varying range of strain over which voids nucleate can be modeled. Needleman & Rice observed that a narrow range of S_N would cause destabilizing effect. Fig.(2.1.2) shows the effect of S_N on the void nucleation function. For stress controlled nucleation, $A = 0$ and B is given by

$$B = \frac{f_N}{S_N\sqrt{2\pi}}\exp\left[-\frac{1}{2}\left(\frac{\sigma_{eq} + \sigma_m - \varepsilon_N}{S_N}\right)^2\right] \tag{2.1.4}$$

Strain controlled nucleation is the most widely used model in the literature for Gurson class of micro-mechanical models.

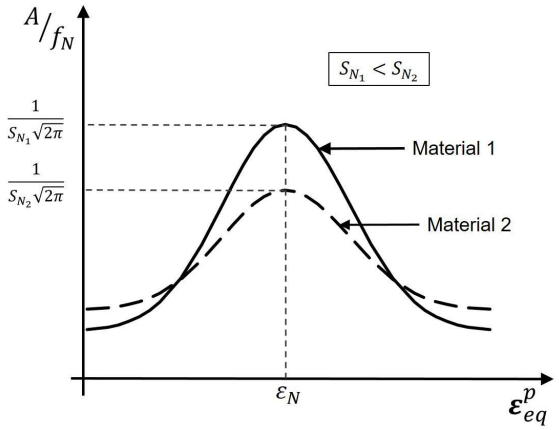

Fig. 2.1.2: Effect of s_N on void nucleation function[64]

2.1.2 Void Growth

The stress free surface of void results in stress and strain concentration in the matrix. Increasing the plastic strain would essentially lead to void growth in the direction of the applied load. McClintock [49] through his analysis of a long circular cylinderical cavity in a non-hardening material, subjected to a tensile stress along the axis, proposed a void growth model which showed an exponential increase of void size with increase in transverse stress. Rice & Tracey [57] analyzed a more realistic model of an isolated void in a remotely uniform stress and strain rate field, to determine the relation between void growth and stress triaxiality(T). They derived the void growth equation in the domain of continuum plasticity which considers separation as a kinematical result of large but localized plastic deformations. Huang modified Rice & Tracey formulation to better capture the void growth at low stress triaxiality

[15]. The resulting void growth rate is expressed as,

$$\dot{f}_g = \begin{cases} 1.28 \exp\left(\frac{3}{2}T\right) \dot{\varepsilon}^p_{eq} & \text{for} \quad T > 1 \\ 1.28\, T^{\frac{1}{4}} \exp\left(\frac{3}{2}T\right) \dot{\varepsilon}^p_{eq} & \text{for} \quad 0.33 \leq T \leq 1 \end{cases} \tag{2.1.5a}$$

Rice & Tracey model highlights the influence of stress triaxiality on void growth, however, this model assumes that the growth rate is independent of the microstructure and the influence of the neighboring voids. Berg [50] proposed a different model which assumed that the void growth could be described by the dilational response of an elastic-plastic continuum containing an imaginary distribution of spherical voids. This approach was later used by Gurson [38] to developed a dilational yield function that depends on von Mises equivalent stress and mean stress. The void growth model proposed by Gurson is given by,

$$\dot{f}_g = (1 - f)\mathrm{tr}(\dot{\boldsymbol{\varepsilon}}^p) = (1 - f)\mathrm{tr}(\boldsymbol{D}) \tag{2.1.6}$$

2.1.3 Void Coalescence

Void coalescence is the final stage in ductile failure mode. It is a sudden and rapid phenomenon where the neighbouring voids link to form a micro crack that propagates quickly and leads to sudden failure. It is a shift from homogeneous deformation to localization of plastic deformation in the intervoid ligaments. Void coalescence is influenced by many parameters like void shape, void orientation, stress triaxiality, void volume fraction, etc. Based on the orientation of the ligaments between the two coalescing voids, two types of localization can occur - Necking and Shear localization.

At low to moderate stress triaxialities, void coalescence occurs due to combination of necking and shear localization, with shear localization having a greater effect. At high triaxialities necking predominates. Macroscopically, ligament failure due to necking results in dimpled fracture surface, while shear localization results in smooth fracture surface as it smeers the voids. Researchers have observed that in various steel and aluminum, nucleation of secondary voids in the intervoid ligaments accelerates and leads to early ligament failure even before the impingement of the larger voids.

Weck [65] carried out an extensive study using high resolution scanning electron microscope (SEM) to understand the coalescence mechanism in Aluminium 5052 containing holes in different orientation. He subject the plates containing holes to a tensile load in vertical directions. Fig.(2.1.3) depicts the necking mechanism when the holes are arranged at 90° to the tensile load and Fig.(2.1.4) depicts the shearing mechanism.

Since coalescence is sudden and quick, it is difficult to formulate a mathematical model that would accurately simulate the two mechanisms. Majority of the proposed

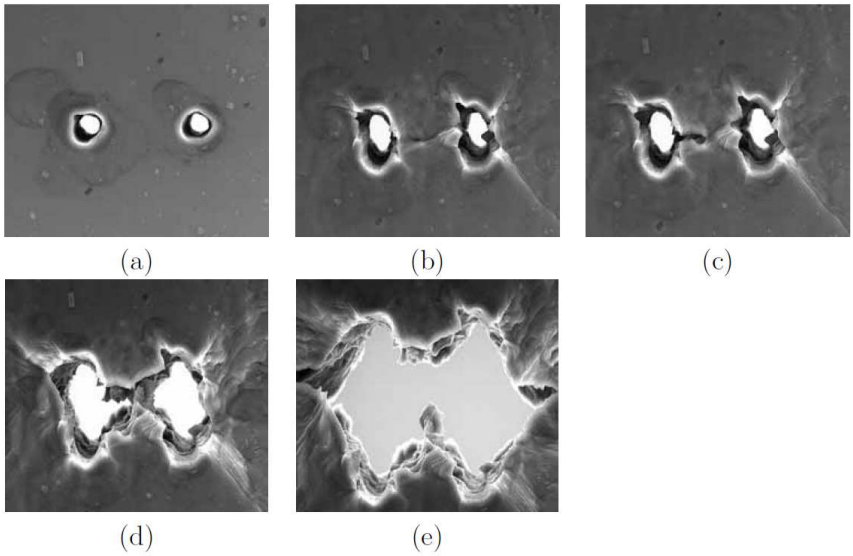

Fig. 2.1.3: Deformation sequence of aluminium alloy 5052 with holes oriented at $90°$ with respect to tensile direction - Necking mechanism [65]

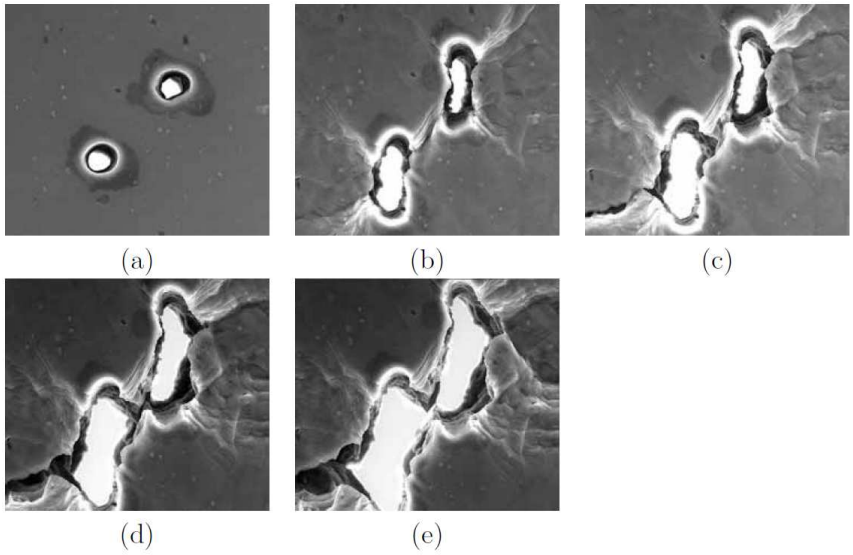

Fig. 2.1.4: Deformation sequence of aluminium alloy 5052 with 2 holes oriented at $45°$ with respect to tensile direction - Shearing mechanism [65]

models consider the coalescence to occur when a material specific geometric parameter reaches a critical value. The parameters could be void shape, porosity and/or void spacing. Tveergard & Needleman [63] proposed a phenomenological model with the assumption that the material failure due to void coalescence occurs at a critical value of void volume fraction(f_c) in accordance to experimental and computation results. This critical value was incorporated into the constitutive equation via the dependence of yield function on void volume fraction(f), in Gurson type damage models. When the void volume fraction reaches a critical, the approximate yield function Φ is modified. The yield function is of the form [63],

$$\Phi = \left(\frac{\sigma_{eq}}{\sigma_Y}\right)^2 + 2f^\star q_1 \cosh\left(\frac{\sigma_{kk}}{2\sigma_Y}\right) - \{1 + (q_1 f^\star)^2\} = 0 \tag{2.1.7}$$

The critical void volume fraction is incorporated by a new coalescence parameter f^*,

$$f^\star = \begin{cases} f, & \text{for } f \leq f_c \\ f_c + \dfrac{\bar{f}_F - f_c}{f_F - f_c}(f - f_c), & \text{for } f_c < f < f_F \\ \bar{f}_F, & \text{for } f > f_F \end{cases} \tag{2.1.8}$$

Here, f_F is the void volume fraction at fracture, which is obtained from the yield function, when the stress carrying capacity vanishes,as

$$\bar{f}_F = 1/q_1 \tag{2.1.9}$$

Embury proposed a geometrical model to predict the fracture of the ligament between two voids. he stipulated that when the void length is equal to the intervoid spacing , shear bands form and the voids coalesce. The strain to failure ε_f is defined given by,

$$\varepsilon_f = \ln\left(\sqrt{\frac{\pi}{6V_f}} - \sqrt{2/3} + \varepsilon_N\right) \tag{2.1.10}$$

Thomason [60] argued that the homogeneous deformation of a ductile material is interrupted by the incipient of plastic limit-load condition, at which point the plastic deformation concentrates in the intervoid matrix over a single sheet of microvoids, which results in a ductile fracture surface. He analysed square prismatic voids in square prismatic unit cells to obtain a closed-form empirical expression of the constraint factor using upper-bound methods. He claimed that replacing an ellipsoidal void with square prismatic void would not lead to serious inaccuracy in the solution when the void volume ratio is less than 0.2. The empirical relation is given by [60]

$$\frac{\sigma_M}{Y} = \frac{F}{(a/b)^n} + \frac{G}{\left(\dfrac{b}{b+d}\right)^m} \tag{2.1.11}$$

In the above equation Y is the uniaxial yield stress, a represents half length of void, b represents half breadth of void and $(b+d)$ represent half breadth of the unit cell. F and G are constants, n and m are exponents. Thomason proposed the following values , $F = 0.1$, $G = 1.2$, $n = 2$ and $m = 0.5$.

Thomason's model is a close approximation of necking mechanism, and is widely used in the literature. It was later modified by various authors ([56], [9], [21], [58]). Pardoen and Hutchinson derived an empirical relation for a cylindrical unit cell containing spheroidal void, as shown in Fig.(2.1.5). They considered a cylindrical disk of elastic-perfectly plastic material welded to rigid platens and constrained against flow at the outer radius. An approximation of limit load for this configuration in terms of average normal stress σ_n was derived in line to Hill's Plane strain analysis of a thin plastic layer welded to and squeezed by two rigid platens. The localisation is assumed to set in when,

$$\frac{\sigma_n}{\sigma_y} = \left[1 - \chi^2\right] \left[\alpha \left(\frac{1-\chi}{\chi w}\right)^2 + \beta \chi^{-1/2}\right] \tag{2.1.12}$$

Where, void aspect ratio w is defined as,

$$w = \frac{R_z}{R_r} \tag{2.1.13}$$

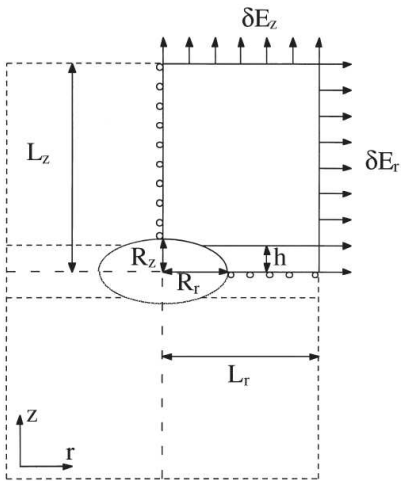

Fig. 2.1.5: Representative Volume Element with geometric parameters, symmetry lines, and boundary conditions [56]

When the initial aspect ratio(λ_0) of the unit cell is 1, the distance between the ligaments(χ) in terms of equivalent plastic strain is given by,

$$\chi = \frac{R_r}{L_r} = \left(\frac{3}{2} f \frac{\lambda}{w}\right)^{1/3}, \quad \text{where} \quad \lambda = \exp\left(\frac{3}{2}\varepsilon_{eq}^p\right) \tag{2.1.14}$$

For flat voids ($W \to 0$), the developed model predicts infinite ductilities. To overcome this drawback, Benzerga introduced a quadratic equation in the denominator based on the unit cell results of Golaganu.

$$\frac{\sigma_n}{\sigma_y} = \left[1 - \chi^2\right] \left[\alpha \left(\frac{\chi^{-1} - 1}{w^2 + 0.1\chi^{-1} + 0.02\chi^{-2}}\right)^2 + 1.3\chi^{-1/2}\right] \tag{2.1.15}$$

The plastic limit load criterion requires knowledge of the void aspect ratios w, spacing ratios χ and the maximum tensile stress transverse to the ligament. In 3D case, a plane exists that is traverse to the ligament and the stress will vary within this plane. The maximum tensile stress in this plane must be determined to evaluate the plastic limit load criterion [22]. Constitute models have been proposed by Chen[22] and Scheyvaerts[58] for the case where voids do not align themselves in the direction of maximum principal stress. Chen[22] proposed a procedure for modeling an arbitrary ellipsoidal void as an axisymmetric void. Consider an arbitrary ellipsoidal void with semi-axes a, b and c with corresponding vectors $\mathbf{n_1}$, $\mathbf{n_2}$ and $\mathbf{n_3}$. The distance

from the center to void surface along the principal loading direction is denoted by R_1. A line-projection of the void is taken with the principal loading direction as the viewing direction to obtain an ellipse with semi-axes R_2 and R_3. The reconstructed geometry of the void is as shown in Fig.(2.1.6) and the equivalent aspect ratio as proposed by Chen is,

$$w_{eq} = \frac{R_1}{\sqrt{R_2 R_3}} \tag{2.1.16}$$

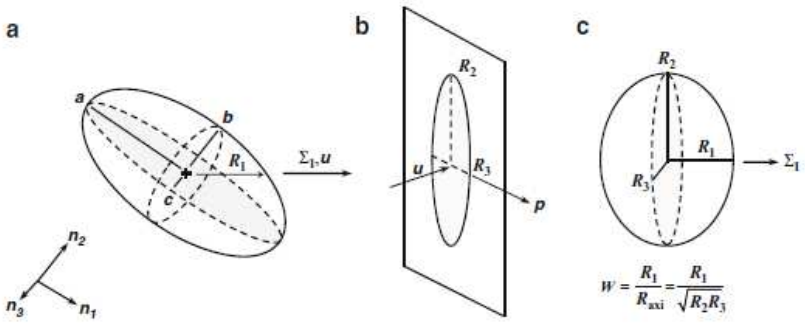

Fig. 2.1.6: Procedure for modelling an arbitrary ellipsoidal void as an axisymmetric void [22]

In VAR model, the semi-axis c and its corresponding vector $\mathbf{n_3}$ is aligned to the loading direction. Hence the equivalent aspect ratio would be defined as,

$$w_{eq} = \frac{c}{\sqrt{ab}} = \sqrt{w_1 w_2} \tag{2.1.17}$$

For an ellipsoidal void, the inter distance between the ligaments χ can be obtained by substituting Eq. (2.1.17) in Eq. (2.1.14).

$$\chi_{eq} = \left(\frac{3}{2} \frac{f}{w_{eq}} \exp\left(\frac{3}{2} \varepsilon_{eq}^{P} \right) \right)^{1/3} \tag{2.1.18}$$

2.2 Overview of damage models

The damage models can be broadly classified into:

1) Phenomenological models

   a) Uncoupled damage models

   b) Coupled damage models

2) Micromechanics based models

2.2.1 Phenomenological models

The phenomenological models can be further categorized into uncoupled damage models and Continuum damage mechanics (CDM) based coupled damage models [15]. In the former approach, failure is predicted to occur when an external variable reaches a critical value without interacting with the constitutive equations. Uncoupled models are easy to implement in an FE software but are not accurate for complex loading conditions and large strains. In the latter approach, the effect of void growth on material behaviour is incorporated by introducing an internal damage variable in the constitutive relation. Void nucleation can also be incorporated by modifying the damage growth law. Lemaitre [48] and Chaboche [20] developed CDM models based on a thermodynamic framework. But, Lemaitre based models were observed to predict the maximum damage locations inaccurately for shear dominated loading. Various extensions have been proposed to these models to increase its efficiency.

2.2.1.1 Uncoupled damage models

Uncoupled damage models, also referred to as damage criteria, implicitly assume that the state of damage of a structure does not influence the state of stress or strain of the material. These models were physically motivated and purely phenomenological. The damage parameter is computed using an integral of a stress state function, which is strain path dependent or independent, based on the model. It takes the general form,

$$\int_0^{\bar{\varepsilon}_f} f(\boldsymbol{\sigma}) d\varepsilon_{eq}^p \text{ or } \int_0^{\bar{\varepsilon}_f} f(\boldsymbol{\varepsilon}) d\varepsilon_{eq}^p = D_c \tag{2.2.1}$$

$\bar{\varepsilon}_f$ is the equivalent plastic strain just at the moment of fracture and D_c is the material constant that defines the onset of fracture. Cockcroft-Latham proposed a criterion based on the tensile strain energy density considering the magnitude of the highest normal tensile stress σ_{max}, given by

$$D_c = \int_0^{\bar{\varepsilon}_f} \sigma_{max} d\varepsilon_{eq}^p \tag{2.2.2}$$

Cockcroft-Latham damage model is often used to predict the initiation of crack and is widely used bulk forming industry. The normalized Cockcroft-Latham damage criterion is defined as,

$$D_c = \int_0^{\bar{\varepsilon}_f} \frac{\sigma_{max}}{\sigma_{eq}} d\varepsilon_{eq}^p \tag{2.2.3}$$

McClintock proposed a model which also included the minimum principal stress and the hardening parameters. According to McClintock

$$f(\boldsymbol{\sigma}) = \frac{\sqrt{3}}{2(1-n)} \sinh\left(\frac{\sqrt{3}}{2(1-n)} \frac{\sigma_1 + \sigma_2}{\sigma_{eq}}\right) + \frac{3}{4} \frac{\sigma_1 - \sigma_2}{\sigma_{eq}} \tag{2.2.4}$$

Rice & Tracey based their damage model on stress triaxiality,

$$f(\boldsymbol{\sigma}) = \exp\left(\frac{3}{2}T\right) \tag{2.2.5}$$

Johnson & Cook [41] proposed a damage model which accounted for path dependency by accumulating damage as the deformation proceeds. The damage indicator depends on strain, strain rate, temperature and pressure.

$$f(\boldsymbol{\sigma}) = \frac{1}{\bar{\varepsilon}_f}, \qquad \bar{\varepsilon}_f = [C_1 + C_2 \exp(C_3 T)]\,[1 + C_4 \ln(\dot{\varepsilon}^*)]\,[1 + C_5 t^*] \tag{2.2.6}$$

where $\dot{\varepsilon}^*$ and t^* are dimensionless strain rate and homologous temperature respectively.

The uncoupled damage models are easy to implement in a FE program and requires minimal computation power. Since they do not influence the material properties, the accuracy of the results are questionable. Their major weakness is the application to complex loading paths outside the identification zone.

2.2.1.2 Coupled damage models

For complex loading paths, such as non-proportional loading or anisothermal, stress distribution and stress triaxiality changes enhanced by the damage is an accelerating factor in structural failure. Close to the rupture condition, the error from uncoupled constitutive equations are in the order of 10 -50% [47]. To predict the damage accurately the continuum equilibrium must be solved in a fully coupled manner with the damage parameters. From physical point of view, this coupling is due to the nature of damage. Damage results in decrease of elasticity modulus, density and plastic strain-hardening. The basic constituents of these damage models are,

1) an equation relating the damage variable and apparent stiffness

2) a loading function specifying the elastic domain

3) a law governing the evolution of damage variable

Lemaitre [47] proposed a continuum based coupled damage model which was derived from a thermodynamic framework. He assumed a scalar damage variable $D(0 \leq D \leq 1)$ which describes isotropic damage as internal variable. D represents the surface density of interaction of micro-cracks and micro-cavities with any plane in the body. The criterion for micro-crack initiation is $D = D_c$, D_c is of the order 0.2 to 0.8 depending upon the material. He derived the state laws of the state variables as well as the dissipation phenomenon from a convex thermodynamic potential ψ of the form,

$$\psi = \psi(\boldsymbol{\varepsilon}^e, t, \alpha, p, D) \tag{2.2.7}$$

α and p are are the internal variables associated with anisotropic hardening X and isotropic hardening R respectively. The effective stress $\boldsymbol{\sigma}'$ is defined as,

$$\boldsymbol{\sigma}' = \frac{\boldsymbol{\sigma}}{1-D} \tag{2.2.8}$$

The elasticity law is given by,

$$\boldsymbol{\sigma} = \rho \frac{\partial \psi}{\partial \varepsilon^e} \tag{2.2.9}$$

The thermodynamic potential defines a variable Y associated with D, which is analogous to elastic strain energy.

$$Y = -\frac{\sigma_{eq}^2}{2E(1-D)^2}\left[\frac{2}{3}(1+\nu) + 3(1-2\nu)T^2\right] \tag{2.2.10}$$

The evolution equations of the internal variables are obtained from Clausius-Duhem inequality. The evolution equation of the damage variable is given by,

$$\dot{D} = \dot{\Lambda}\frac{\partial \Phi}{\partial Y} = \left(\frac{-Y}{S_0}\right)^{s_0} \frac{\dot{\Lambda}}{1-D} \tag{2.2.11}$$

S_0 and s_0 are temperature dependent material constants , which must be identified for each type of damage. It is also important to note that the standard Lemaitre model is symmetric with respect to stress state. Lemaitre model is being continuously investigated and various modifications are proposed to improve its accuracy under shear loading.

2.2.2 Micromechanics based damage models

As described in the introduction, these models are based on microstructure consideration. The influence of ductile damage in the yield condition is taken into account by introducing the porosity term and mean stress in the yield function. Von Mises plasticity model is independent of mean stress and predict plastic incompressibility and therefore could not show the dilatancy evident in porous ductile materials. Here a short overview of Gurson model is described, as the results from VAR model would be compared to Gurson model in later sections. Gurson [38] proposed the yield function to be of the form,

$$\Phi = \left(\frac{\sigma_{eq}}{\sigma_y}\right)^2 + 2f\cosh\left(\frac{3\sigma_m}{2\sigma_y}\right) - 1 - f^2 \tag{2.2.12}$$

The evolution equation of the void volume fraction is obtained from continuity equation as,

$$\dot{f}_g = (1-f)\dot{\varepsilon}_{kk}^p \tag{2.2.13}$$

Several extensions and modifications (Tvergaard & Needleman [63] , Gao et al. [32]) were proposed to the original Gurson model to improve its accuracy and to simulate the complete damage process by accounting for interaction, nucleation and coalescence of voids. Tvergaard [62] introduced 3 constants (q_1, q_2 and q_3) in the Gurson

yield function to account for interaction between neighboring voids based on analysis of a material containing a doubly periodic array of circular cylindrical voids under plane strain conditions. Chu & Needleman [23] incorporated two parameter void nucleation which allows for plastic strain controlled and stress controlled nucleation to be modeled. Tvergaard and Needleman [63] later proposed a modification to capture the rapid deterioration of stiffness after localization. This model is generally referred to as Gurson-Tvergaard-Needleman (GTN) model in literature. The Gurson class of models are proved to be inaccurate for low tri-axiality loading conditions and shear dominated models, where the void growth mechanism is inactive. Xue [69] and Nahshon & Hutchinson [51] proposed a phenomenological modification by including the effect of third stress invariant in GTN model to improve it's accuracy under shear loading. However, this model was proved to over predict the damage under high stress triaxialities conditions, which was an advantage of the original Gurson model. Consequently, Nielsen and Tvergaard [53] proposed a modification to Nahshon-Hutchinson model, to allow for damage accumulation under shear loading to be active only for low stress triaxialities [30]. A recent shear modification for Gurson class model was proposed by Zhou et. al. [71] by combining damage mechanics concepts of Lemaitre with the GTN void growth model. But the proposed modifications did not account for void shape or void orientation, which would be key to accurately predict damage under complex loading conditions.

Tvergaard & Needleman[63] modified the Gurson yield function to take the form,

$$\Phi = \left(\frac{\sigma_{eq}}{\sigma_y}\right)^2 + 2q_1\, f^* \cosh\left(q_2 \frac{3\sigma_m}{2\sigma_y}\right) - 1 - q_3 f^{*2} \tag{2.2.14}$$

They suggested the constants q_1, q_2 and q_3 to take the values 1.5, 1.0 and q_1^2 respectively, and f^* is the critical coalescence parameter as described in Eq. (2.1.8) in section 2.1.3. Gurson yield function could be obtained from the above equation by setting the constants to unity. The evolution of void volume fraction is given as,

$$\dot{f} = \dot{f}_n + \dot{f}_g \tag{2.2.15}$$

Gologanu, Leblond & Devaux [33][34] porposed (GLD model) a Gurson based constitutive model which accounted for void shape effects by considering a perfectly plastic material with aligned spheroidal voids subjected to axisymmetric loading condition. Several extensions have been proposed for this class of models to account for ellipsoidal voids , final void coalescence and void rotations. Pardoen and Hutchinson [56] combined GLD model with Thomason [60] coalescence model to accurately predict the formation of crack prior to existence and the crack growth after formation. Recently, Schevyaerts [58] proposed a modification to account for void orientation and void rotation by introducing a new state variable to account for void rotation based on the work of Kailasam and Ponte Castañeda [43]. But, this model was proved only for plane strain simple shear conditions.

Based on type of nucleation model, i.e. stress dependent or strain dependent nucleation, corresponding formulation from Section 2.1.1 should be used for $\dot{f}_n$, and

$\dot{f}_g$ is as given by Eq. (2.2.13). Fig.(2.2.1) shows the yield locus of a von Mises yield function and Gurson yield function. It can be seen that as the porosity increases, the yield locus shrinks due to which the stress carrying capacity of the material reduces.

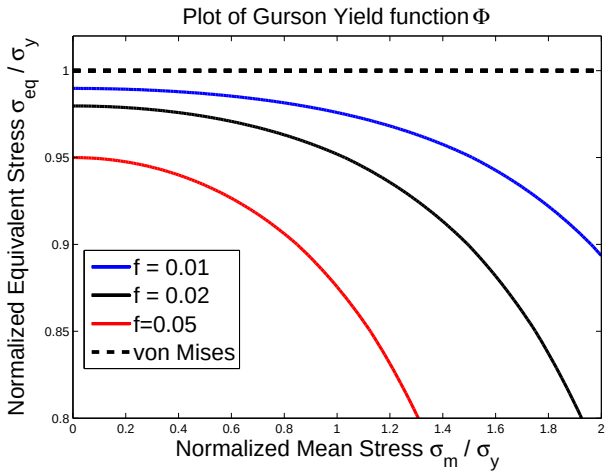

Fig. 2.2.1: Comparison of Yield surface of von-Mises plasticity and Gurson model (at different void volume fraction)

2.3 Theoretical Background

2.3.1 Stresses and Strains

2.3.1.1 Hydrostatic and Deviatoric Stresses

Any state of stress can be additively decomposed into hydrostatic stress (mean stress) $\sigma_m \boldsymbol{I}$ and deviatoric stress $\boldsymbol{s}$. In index notations it is given by [2],

$$\sigma_{ij} = \sigma_m \delta_{ij} + s_{ij} \tag{2.3.1}$$

$$\sigma_m = \frac{\sigma_{11} + \sigma_{22} + \sigma_{33}}{3} \tag{2.3.2}$$

The hydrostatic stress accounts for pure tension or compression and it remains unchanged with a change in coordinate system. While, deviatoric stress accounts only pure shear and the principal direction of stresses coincides with the principal directions of the deviatoric stresses. The deviatoric stress invariants are given by,

$$J_1 = s_{11} + s_{22} + s_{33}$$

$$J_2 = -(s_{11}s_{22} + s_{22}s_{33} + s_{33}s_{11} - s_{12}^2 - s_{23}^2 - s_{31}^2)$$

$$J_3 = s_{11}s_{22}s_{33} - s_{11}s_{23}^2 - s_{22}s_{31}^2 - s_{33}s_{12}^2 + 2s_{12}s_{23}s_{31}$$

The second invariant can also expressed in terms of principal stresses as,

$$J_2 = \frac{1}{6}\left[(\sigma_1 - \sigma_2)^2 + (\sigma_2 - \sigma_3)^2 + (\sigma_3 - \sigma_1)^2\right] \tag{2.3.4}$$

Stress triaxiality under different loading conditions [46]		
Loading	2D-Plane stress	3D
Uniaxial Tension	0.33	0.33
Uniaxial Compression	-0.33	-0.33
Biaxial Tension	0.66	0.66
Biaxial Compression	-0.66	-0.66
Triaxial Tension	-	∞
Triaxial Compressio	-	$-\infty$
Pure Shear	0	0

Table 2.3.1: Stress triaxiality observed under different loading conditions

2.3.1.2 Equivalent Stress

Equivalent stress or von Mises stress is a stress at which yielding is predicted to occur in isotropic ductile materials. It is derived from the distortion-energy theory for ductile materials which states that yielding occurs when the distortion strain energy per unit volume reaches or exceeds the distortion strain energy per unit volume for yield in simple tension or compression of the same material. In deviatoric stress space the equivalent stress is given [2],

$$\sigma_{eq} = \sqrt{\frac{3}{2}\boldsymbol{s} : \boldsymbol{s}} = \sqrt{3J_2} \tag{2.3.5}$$

In terms of non principal stress components and principal stresses,

$$\sigma_{eq} = \frac{1}{\sqrt{2}}\left[(\sigma_1 - \sigma_2)^2 + (\sigma_2 - \sigma_3)^2 + (\sigma_3 - \sigma_1)^2\right]^{1/2}$$

$$\sigma_{eq} = \frac{1}{\sqrt{2}}\left[(\sigma_x - \sigma_y)^2 + (\sigma_y - \sigma_z)^2 + (\sigma_z - \sigma_x)^2 + 6(\tau_{xy}^2 + \tau_{yz}^2 + \tau_{zx}^2)\right]^{1/2}$$

2.3.1.3 Stress Triaxiality

A material's strain and ductile fracture strongly depends on the existing state of stress in individual areas of the material. In most general case, the state of stress is determined by the 6 stress components or 3 principal stresses. Using the state of stress tensor to identify unequivocally individual stresses during shaping process is cumbersome. As a practical approach, stress triaxiality (T) is used to identify the state of stress and is defined as the ratio of mean stress to equivalent stress [2]. Stress triaxiality is varied over a wide range covering most practical situations.

$$T = \frac{\sigma_m}{\sigma_{eq}} \tag{2.3.7}$$

The effect of stress triaxiality on metals is strong and has been widely documented. Higher the triaxiality lower the fracture strain. Higher levels of stress triaxiality are achieved in cracked specimens with the maximum expected to be around 3.0 ahead of the crack tip of a strain hardening material under plane strain condition [10].

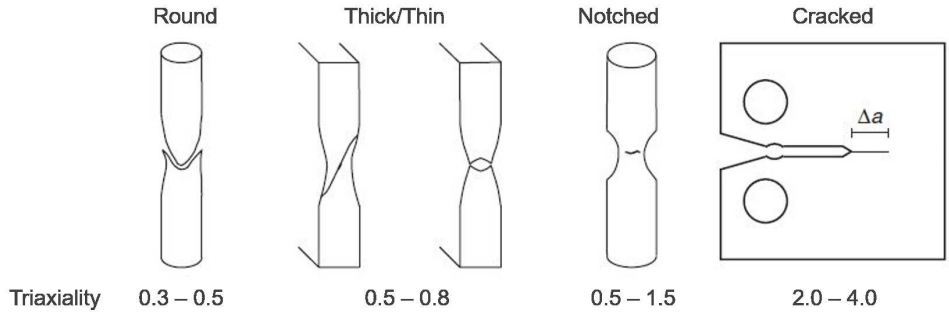

Fig. 2.3.1: Specimens used in ductile fracture experiments with corresponding triaxialities [10]

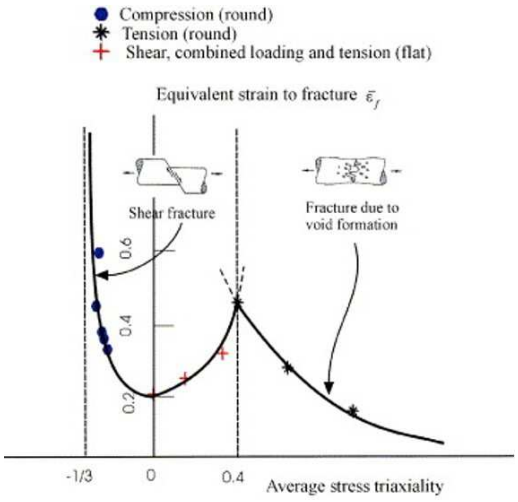

Fig. 2.3.2: Dependence of equivalent strain to fracture on stress triaxialities for aluminum alloy 2024-T351 [7]

2.3.1.4 Equivalent Plastic Strain

To account for hardening, a quantity that describes the deformation history of a material which increase during plastic deformation, is required. Equivalent plastic strain is most widely used quantity in this regard. For an isotropic, von Mises material, the equivalent plastic strain ε^p_{eq} is derived from equivalent plastic strain rate $\dot{\varepsilon^p_{eq}}$ which is defined analogous to von Mises yield criterion as [2],

$$\dot{\varepsilon_{eq}}^{p} = \sqrt{\frac{2}{3}\dot{\varepsilon}^p_{ij}\dot{\varepsilon}^p_{ij}} \tag{2.3.8}$$

The equivalent plastic strain is the integral of the equivalent plastic strain rate,

$$\varepsilon^p_{eq} = \int_0^t \dot{\varepsilon}^p_{eq} dt \tag{2.3.9}$$

2.3.1.5 Objective stress rates

A fundamental axiom of constitutive theory is the principal of material objectivity which states that a physical quantity is objective if it is independent of an observer. A quantity is said to be objective if it satisfies the following condition [11],

$$\begin{array}{rc} \text{Tensor:} & \boldsymbol{A}^* = \boldsymbol{Q}\boldsymbol{A}\boldsymbol{Q}^T \\ \text{vector:} & \boldsymbol{u}^* = \boldsymbol{Q}\boldsymbol{u} \\ \text{scalar:} & a^* = a \end{array}$$

where, $\boldsymbol{Q}$ is a rotation tensor, the components $(\ )^*$ are in a rotated frame. Cauchy stress tensor ($\boldsymbol{\sigma}$), Kirchhoff stress tensor ($\boldsymbol{\tau}$) and second Piola-Kirchhoff stress tensor ($\boldsymbol{S}$) are material objective stresses. But, the rates of objective stress tensors are not necessarily objective. The material time derivative of Cauchy stress tensor ($\boldsymbol{\sigma}$) is not objective, and is given by

$$\dot{\boldsymbol{\sigma}} = \boldsymbol{Q}\dot{\boldsymbol{\sigma}}\boldsymbol{Q}^T + \dot{\boldsymbol{Q}}\boldsymbol{\sigma}\boldsymbol{Q}^T + \boldsymbol{Q}\boldsymbol{\sigma}\dot{\boldsymbol{Q}}^T \tag{2.3.10}$$

In order to ensure material objectivity in the formulation of finite strain constitutive equations which depend on stress rates, it is important to define objective stress rates. They are obtained by suitably modifying the material time derivative. Many different objective rates of stress are proposed in the literature depending on the choice of rotation tensor. Jaumannn rate and Green Naghdi rate are used often in constitutive equations. Jaumann rate of Cauchy stress $\left(\overset{\nabla}{\boldsymbol{\sigma}}\right)$ is defined as [13],

$$\overset{\nabla}{\boldsymbol{\sigma}} = \dot{\boldsymbol{\sigma}} - \boldsymbol{W}\boldsymbol{\sigma} + \boldsymbol{\sigma}\boldsymbol{W} \tag{2.3.11}$$

where $\boldsymbol{W}$ is the skew-symmetric part of velocity gradient known as spin tensor.

$$\boldsymbol{W} = \boldsymbol{L}_{skew}, \qquad \boldsymbol{L} = \dot{\boldsymbol{F}}\boldsymbol{F}^{-1} \tag{2.3.12}$$

Green-Naghdi rate $\left(\overset{\triangle}{\boldsymbol{\sigma}}\right)$ is obtained by pulling back $\boldsymbol{\sigma}$ to reference configuration, taking the material time derivative of $\boldsymbol{\sigma}$ in reference configuration, and pushing forward the derivative to deformed configuration [27].

$$\overset{\triangle}{\boldsymbol{\sigma}} = \dot{\boldsymbol{\sigma}} - \boldsymbol{\Omega}\boldsymbol{\sigma} + \boldsymbol{\sigma}\boldsymbol{\Omega} \tag{2.3.13}$$

where $\boldsymbol{\Omega}$ is the skew symmetric tensor which depends on the rotation tensor $\boldsymbol{R}$, given by,

$$\boldsymbol{\Omega} = \dot{\boldsymbol{R}}\boldsymbol{R}^T \tag{2.3.14}$$

2.3.2 Theory of Rate independent Elasto-Plasticity

The theory of plasticity provides a general framework for the continuum constitutive description of the behaviour of materials which undergo permanent (plastic) deformation. The theory deals with the calculation of stress and strain in plastic deformations, and not, as a literal interpretation suggests, the physical description

of plasticity. There are two major outcomes of the theory - first, to develop explicit relation between stress and strain to agree with the experimental observations, and second, to develop mathematical techniques to compute non uniform distribution of stress and strain in a plastically deformed body [40]. This theory is restricted to materials where the permanent deformation does not depend on the rate of loading, and is often referred to as rate independent theory of plasticity.

In case of elastic constitutive equation the stress $\boldsymbol{\sigma}$ depends only on the strain $\boldsymbol{\varepsilon}$ and not on the history. But in case of Elasto-Plastic constitutive material models, the stress also depends on the past history. Hence, additional variables know as internal variables or plastic internal variables $\boldsymbol{q}$ are introduced in to the constitutive equations. When the evolution of plastic strains is zero, the internal variables do not evolve. A classical rate independent Plasticity constitutive model has the following basic components:

a) Decomposition of the elastoplastic strain

b) Elastic stress-strain relation

c) a yield surface, which defines the elastic domain

d) a plastic flow rule defining the evolution of the plastic strain

e) a hardening law

f) loading/unloading condition

g) consistency condition

2.3.2.1 Additive decomposition of Strain tensor

It is assumed that the strain tensor can be decomposed in to the elastic $\boldsymbol{\varepsilon^e}$ and plastic $\boldsymbol{\varepsilon^p}$ strain tensors. [2]

$$\boldsymbol{\varepsilon} = \boldsymbol{\varepsilon^e} + \boldsymbol{\varepsilon^p} \tag{2.3.15}$$

The elastic strain tensor from the above equation can be written as $\boldsymbol{\varepsilon^e} = \boldsymbol{\varepsilon} - \boldsymbol{\varepsilon}^p$. The corresponding rate form of the additive split is given as,

$$\dot{\boldsymbol{\varepsilon}} = \dot{\boldsymbol{\varepsilon}}^e + \dot{\boldsymbol{\varepsilon}}^p \tag{2.3.16}$$

From computational point of view, the incremental form is also very important. The incremental form of the strain tensor is given by,

$$\mathrm{d}\boldsymbol{\varepsilon} = \mathrm{d}\boldsymbol{\varepsilon}^e + \mathrm{d}\boldsymbol{\varepsilon}^p \tag{2.3.17}$$

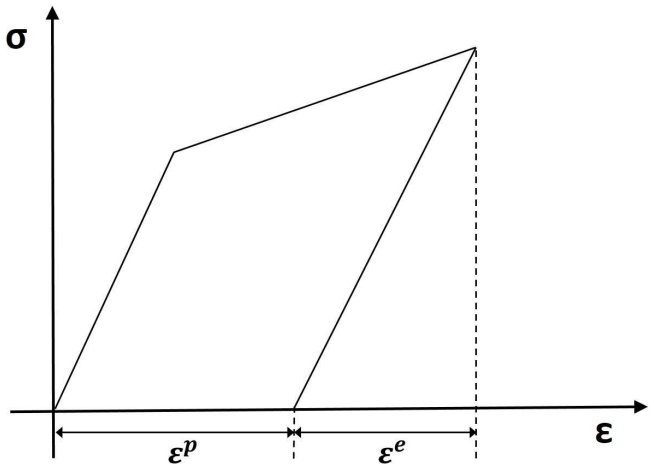

Fig. 2.3.3: Uniaxial tensile stress strain curve of a linear isotropic hardening material with strain decomposition

2.3.2.2 Elastic Stress strain relation

The stress tensor $\boldsymbol{\sigma}$ is related to the elastic strain $\boldsymbol{\varepsilon}^e$ by means of a stored energy function $\mathbf{W}$. For a linear elastic material , the energy function is given by, $\mathbf{W}=\frac{1}{2}\boldsymbol{\varepsilon}^e : \boldsymbol{C} : \varepsilon^e$. Here $\boldsymbol{C}$ is the elastic modulus. The stress-strain relation is given by [2],

$$\boldsymbol{\sigma} = \boldsymbol{C}(\varepsilon - \varepsilon^p) \tag{2.3.18}$$

In incremental form, it is given by

$$\mathrm{d}\boldsymbol{\sigma} = \boldsymbol{C}(\mathrm{d}\varepsilon - \mathrm{d}\varepsilon^p) \tag{2.3.19}$$

2.3.2.3 Yield Criterion and Yield Surface [2]

Plastic flow would occur when the stresses attain a certain critical value. This critical value is defined by the yield function Φ. The yield function is negative when the material deforms elastically , and reaches zero when plastic flow is imminent. The plastic flow occurs when,

$$\Phi(\boldsymbol{\sigma}, \boldsymbol{q}) = 0 \tag{2.3.20}$$

Any stress lying in the elastic domain or on its surface is know as plastically admissible domain, which is given by,

$$\bar{\mathscr{E}} = \{\boldsymbol{\sigma} | \Phi(\boldsymbol{\sigma}, \boldsymbol{q}) \leq 0\} \tag{2.3.21}$$

The yield surface gives the set of stresses for which plastic yielding may occur, and it defines the boundary of the elastic domain.

2.3.2.4 Plastic Flow Rule [2]

The flow rule defines the magnitude and direction of the plastic strain increment $\mathrm{d}\varepsilon^{\mathrm{p}}$ for a given increment of all stress components during yielding. The direction of

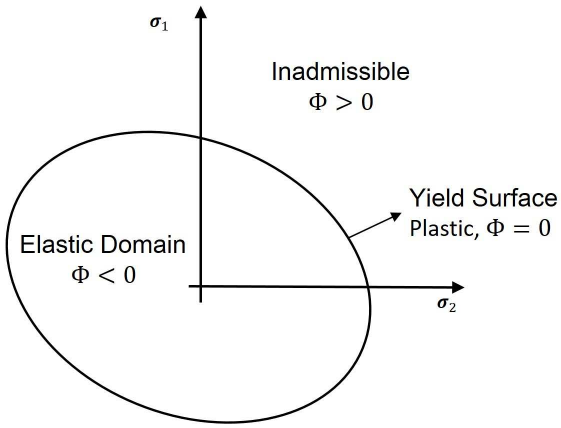

Fig. 2.3.4: Yield Surface [2]

the plastic flow is determined by the normality rule which states that $\mathrm{d}\varepsilon^{\mathrm{p}}$ is normal to the yield surface at the point. The flow rule is usually defined in terms of non negative, convex flow potential Ψ, which is assumed to take the form,

$$\Psi = \Psi(\boldsymbol{\sigma}, \boldsymbol{q}) \qquad \text{and} \qquad \Psi(0,0) = 0 \tag{2.3.22}$$

The flow vector $\boldsymbol{R}$ is defined as the derivative of the flow potential with respect to stress tensor $\boldsymbol{\sigma}$,

$$\boldsymbol{R} = \frac{\partial \Psi}{\partial \boldsymbol{\sigma}} \tag{2.3.23}$$

Models which use yield function as the flow potential ,i.e., $\Psi = \Phi$, are called asso-

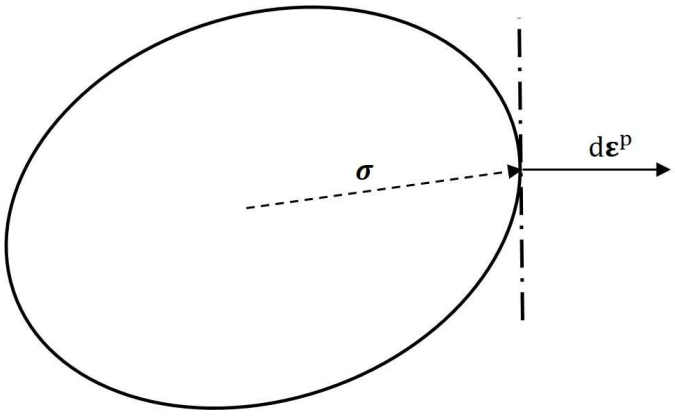

Fig. 2.3.5: Geometrical interpretation of normality rule [2]

ciative plasticity model. Most of the ductile materials can be defined by associative plastic models. The flow vector in this case is given by,

$$\boldsymbol{N} = \frac{\partial \Phi}{\partial \boldsymbol{\sigma}} \tag{2.3.24}$$

The plastic flow rule relates the evolution of plastic strain to the flow vector,

$$\dot{\varepsilon}^p = \dot{\Lambda}\boldsymbol{N} \tag{2.3.25}$$

$$\mathrm{d}\varepsilon^{\mathrm{p}} = \mathrm{d}\Lambda\mathrm{N} \tag{2.3.26}$$

Where $\dot{\Lambda}$ is know as plastic multiplier or the consistency parameter. It provides means to determine the amount of plastic flow and hardening such that the condition $\Phi = 0$ is conserved.

2.3.2.5 Hardening Law [2]

Due to plastic straining, the resistance of the material to plastic flow increases. Which implies that the size and shape of the yield surface changes due to plastic loading. Practically this change is arbitrary and is difficult to describe accurately. Hardening is often described by two types of hardening, isotropic hardening and kinematic hardening. In case of isotropic hardening the yield surface retains its shape but only increases in size. But, in case of kinematic hardening the yield surface retains its shape and size, merely translates in stress space.
The hardening law defines the evolution of the hardening variables. It relates the evolution to a hardening modulus $\boldsymbol{H}$.

$$\dot{\boldsymbol{q}} = \dot{\Lambda}\boldsymbol{H} \tag{2.3.27}$$

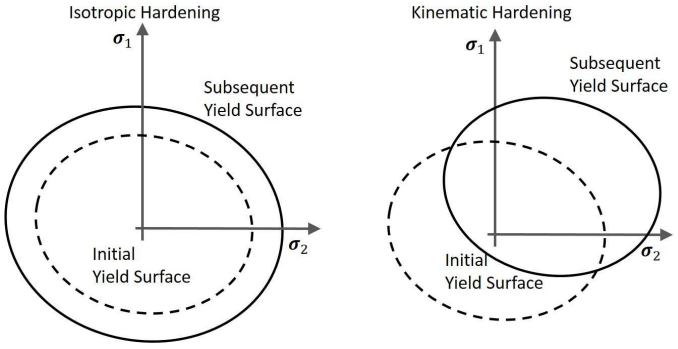

Fig. 2.3.6: Change of yield surface during Isotropic and Kinematic Hardening [2]

2.3.2.6 Loading/Unloading and Consistency Condition

The plastic multiplier $\dot{\Lambda}$ introduced in the flow rule, is assumed to be a non negative parameter. And, for any stress to be admissible, its absolute value must be less than or equal to the yield stress. These conditions impart the following unilateral constraints,

$$\dot{\Lambda} \geq 0 \tag{2.3.28a}$$

$$\boldsymbol{\Phi} \leq 0 \tag{2.3.28b}$$

Within the elastic domain ($\Phi > 0$), the increment of plastic strain is zero, which implies $\dot{\Lambda} = 0$. And, on the yield surface ($\Phi = 0$), $\dot{\varepsilon}^p \neq 0$, which implies $\dot{\Lambda} > 0$. This

leads us to the additional constraint,

$$\dot{\Lambda}\boldsymbol{\Phi} = 0 \tag{2.3.29}$$

Eq. (2.3.28) and Eq. (2.3.29) together are know as the Kuhn-Tucker condition.

An explicit equation for determination of the plastic multiplier has not been introduced yet. As stated above the plastic multiplier vanishes during elastic straining. But, during plastic straining it can assume any non-negative value. Taking a derivative of Eq. (2.3.29), we obtain,

$$\dot{\Lambda}\dot{\boldsymbol{\Phi}} = 0 \tag{2.3.30}$$

Eq. (2.3.30) is referred to as consistency condition in literature. Additionally, on the yield surface, the plastic multiplier is non-zero. Hence,

$$\dot{\boldsymbol{\Phi}} = 0 \tag{2.3.31}$$

2.3.3 Finite Strain Plasticity

An extension of the infinitesimal theory of plasticity to large strain is not straight forward, and a number of alternative formulations have been proposed. These formulations can be classified in to hypoelastic-plastic model and the hyperelastic-plastic models. In hypoelastic based constitutive formulations, the standard infinitesimal elastoplastic models are extended to the finite strain range by reformulating the original evolution equations in terms of suitable objective strain rates. In these formulations basic questions about proper kinematic description of plastic flow, characterization of elastic behaviour and choice of adequate stress and strain measures arises. Also, special care must be exercised to preserve the fundamental principle of objectivity of the integration algorithm. This lead to the development of objectively incremental algorithms which add significantly to the computational cost of the analysis. Hyperelastic models were developed to overcome the drawbacks of the former. It is based on hyperelastic description in conjunction with multiplicative decomposition of deformation gradient. In these models, the requirement of incremental objectivity is trivially satisfied. Of late, hyperelastic formulations are gaining wide spread acceptance and have been proven successful for wide range of applications [27].

2.3.3.1 Hypoelastic - Plastic Models [27]

In this section a brief overview of hypoelastic-plastic formulation is provided, as the constitutive model discussed in later sections is based on the same. A large class of hypoelastic materials is encompassed in the linear relation between objective stress rate $\overset{\circ}{\boldsymbol{\sigma}}$ and rate of deformation $\boldsymbol{D}$,

$$\overset{\circ}{\boldsymbol{\sigma}} = \overset{\circ}{\boldsymbol{\mathcal{C}}} : \boldsymbol{D} \tag{2.3.32}$$

$\boldsymbol{C}$ is the corresponding forth order elastic moduli which depends on the stress and must be an objective function. In a hypoelastic-plastic model, the rate of deformation is additively decomposed into elastic and plastic components,

$$\boldsymbol{D} = \boldsymbol{D}^e + \boldsymbol{D}^p \tag{2.3.33}$$

The elastic response is,

$$\overset{\circ}{\boldsymbol{\sigma}} = \boldsymbol{C} : (\boldsymbol{D} - \boldsymbol{D}^p) \tag{2.3.34}$$

The plastic flow rule is given in terms of the plastic rate of deformation,

$$\boldsymbol{D}^p = \dot{\Lambda}\frac{\partial \Phi}{\partial \boldsymbol{\sigma}} = \dot{\Lambda}\boldsymbol{N} \tag{2.3.35}$$

The consistency condition,

$$\dot{\Phi} = \frac{\partial \Phi}{\partial \boldsymbol{\sigma}} : \dot{\boldsymbol{\sigma}} + \frac{\partial \Phi}{\partial \boldsymbol{q}}.\dot{\boldsymbol{q}} \tag{2.3.36}$$

$$\Rightarrow \dot{\Phi} = \frac{\partial \Phi}{\partial \boldsymbol{\sigma}} : \left(\overset{\circ}{\boldsymbol{\sigma}} + \boldsymbol{W}\boldsymbol{\sigma} - \boldsymbol{\sigma}\boldsymbol{W}\right) + \frac{\partial \Phi}{\partial \boldsymbol{q}}.\dot{\boldsymbol{q}} \tag{2.3.37}$$

For an isotropic model, the product of $\boldsymbol{\sigma}$ and $\partial\Phi/\partial\boldsymbol{\sigma}$ are commutative. Also, considering the symmetry of $\boldsymbol{\sigma}$, and skew-symmetry of $\boldsymbol{W}$, it can shown that,

$$\frac{\partial \Phi}{\partial \boldsymbol{\sigma}} : (\boldsymbol{W}\boldsymbol{\sigma} - \boldsymbol{\sigma}\boldsymbol{W}) = 0 \tag{2.3.38}$$

Hence the consistency condition reduces to,

$$\dot{\Phi} = \frac{\partial \Phi}{\partial \boldsymbol{\sigma}} : \overset{\circ}{\boldsymbol{\sigma}} + \frac{\partial \Phi}{\partial \boldsymbol{q}}.\dot{\boldsymbol{q}} \tag{2.3.39}$$

For detailed explanation on Hypoelasticity and hyper-elasticity, please refer [27].

2.3.4 Mechanics of Heterogeneous Materials - A brief overview

At a certain (smaller) length scale, all real materials appear inhomogeneous, i.e. they consist of distinguishable phases. These phases may be cracks, voids, particles, grain boundaries, fibres in a laminate, irregularities in a crystal lattice, etc[35]. Each phase exhibits different mechanical properties and orientations [45]. The length scale at which a material is considered inhomogeneous is not explicit, it depends on the material and its application. For example, concrete and wood exhibit inhomogeneity at a larger scale in comparison to high strength steel, whose properties are governed by a complex microstructure at a much smaller scale. Mechanics of heterogeneous material deals with the micromechanical study of the behaviour of each phase and its influence on overall properties of the material.

2.3.4.1 Homogenization and Representative volume element (RVE)

For a certain microscopic volume of the material, the heterogeneous microstructure can be considered macroscopically as homogeneous, with spatially constant effective properties, which accounts for the microstructure in an averaged sense. This micro-to-macro transition is know as homogenization[35]. The effective properties of the homogenized material are obtained from various micromechanical material models like Voigt and Reuss, Self Consistent, Dilute Distribution, and Hashin- Shtrikman. The volume at which homogenization has been introduced, is known as Representative Volume element (RVE) in the literature. It is an average representation of the entire material - structurally and statistically. An RVE has to be statistically homogeneous, i.e. any arbitrary volume of the microstructure with the same dimensions of an RVE should lead to the same macroscopic properties. To effectively apply the concept of an RVE, one of the requirement is the existence of two length scales - a macroscopic length scale L, that defines the infinitesimal vicinity, and the microscopic length scale l, that characterizes the smallest significant dimension of the micro-heterogeneity [29]. The ratio of the length scale is given by $L/l >> 1$. The size of an RVE must be much greater than the characteristic length of the inhomogeneity, but should be smaller in comparison to the macro scale. Hence it must satisfy the condition,

$$l << d << L \tag{2.3.40}$$

The assumption of statistical homogeneity allows the isolation of an RVE [45].

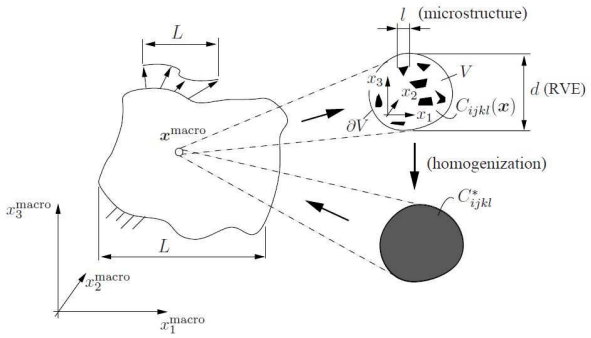

Fig. 2.3.7: Homogenization and Length scale [35]

There exists a definitive surface displacement and surface tractions on the boundary of an RVE, and definitive stress field and strain field with in the RVE. The mechanical behaviour of the effective homogenized material is described by a constitutive law, which is obtained from the detailed fields of the RVE through an averaging procedure. When the macroscopic homogeneous stress and homogeneous strains are applied on the RVE of volume V, the average stress and average strain is defined as[8],

$$\bar{\sigma}_{ij} = \frac{1}{V}\int_V \sigma_{ij} dV \tag{2.3.41}$$

$$\bar{\varepsilon}_{ij} = \frac{1}{V}\int_V \varepsilon_{ij} dV \tag{2.3.42}$$

Average Stress and Average Strain Theorem

To obtain the locally distributed stress and strain fields in the RVE, we have to solve the microscopic boundary value problem with suitable boundary conditions[29] ,

$$\text{div}\boldsymbol{\sigma} = 0 \tag{2.3.43}$$

A homogeneous strain field can be produced by applying linear displacements on boundary S and a homogeneous stress field can be obtained by applying a traction t_i,

$$u_i(S) = \varepsilon^0_{ij} x_j \tag{2.3.44}$$

$$t_i(S) = \sigma^0_{ij} n_j \tag{2.3.45}$$

where, ε^0_{ij} and σ^0_{ij} are constant homogeneous strain and stress respectively.
The average strain theorem states that the macroscopic strain (volumetric average) is equal to constant homogeneous strain applied on the boundary.

$$\bar{\varepsilon}_{ij} = \varepsilon^0_{ij} \tag{2.3.46}$$

Analogously, the average stress theorem states that the macroscopic stress (volumetric average) is equal to the homogeneous microscopic stress at the boundary.

$$\bar{\sigma}_{ij} = \sigma^0_{ij} \tag{2.3.47}$$

Hill Condition

The underlying principal in most of the analytical models which predict the homogenized macroscale response of heterogeneous material in small strain linear elasticity framework, is the Hill condition. It states that the averaged macroscopic strain energy density is equal to microscopic strain energy density in an RVE [29].

$$\langle \boldsymbol{\sigma} \cdot \boldsymbol{\varepsilon} \rangle = \bar{\boldsymbol{\sigma}} \cdot \bar{\boldsymbol{\varepsilon}} \tag{2.3.48}$$

2.3.4.2 Inclusion and Eshelby Tensor

Consider a homogeneous linear elastic solid of volume V and surface S with elastic constant C_{ijkl} as shown in Fig.(2.3.8). The sub region V would exhibit a stress free permanent deformation ε^*_{ij}, if not for the constraints imposed by the surrounding material. Then the material in the V is known as inclusion and the material in Ω is known as matrix. It is to be noted that the inclusion and the matrix are associated with the same elasticity, if the elasticity are different, then the material in V would be know as inhomogeneity. The stress free strain ε^*_{ij} is also known as eigenstrain. The eigenstrain in the matrix is equal to zero and is non zero in the inclusion.
For infinitesimal deformation in linear elasticity, the total strain is the sum of elastic

strain and eigenstrain,

$$\varepsilon_{ij} = \varepsilon^e_{ij} + \varepsilon^*_{ij} \tag{2.3.49}$$

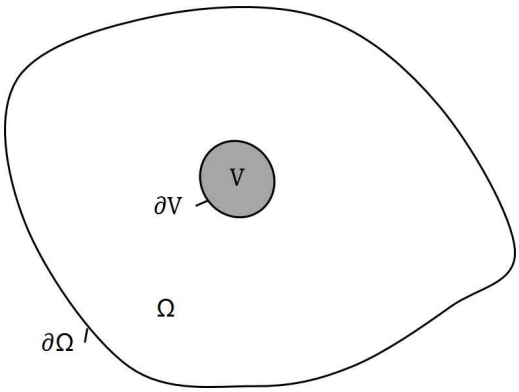

Fig. 2.3.8: Inclusion and Matrix [66]

Eshelby [31] proposed a method to solve the elastic state of ellipsoidal inclusion and the matrix with the help of a set of imaginary cutting, straining and welding operations. He used the superposition principal of linear elasticity. The procedure the author used is as follows,

Step 1: Remove the inclusion from the matrix, and allow it to undergo the stress-free strain ε^*_{ij}. The stress, strain and displacement in the matrix are zero at this stage, and the stress in inclusion is zero. The strain and displacement in the inclusion are given by,

$$\varepsilon_{ij} = \varepsilon^*_{ij} \qquad \text{and} \qquad u_i = \varepsilon^*_{ij} x_j \tag{2.3.50}$$

Step 2: Apply the surface traction $-\sigma^*_{ij} n_j$ to ∂V , to bring back the inclusion to its original shape. The Eigenstress is given by Hooke's law,

$$\sigma^*_{ij} = C_{ijkl} \varepsilon^*_{ij} \tag{2.3.51}$$

Now reweld the inclusion into the matrix. The surface force becomes a layer of body force.

Step 3: To relax the body force, apply a traction of $+\sigma^*_{ij} n_j$ to ∂V. Now the body is free from external force but is in a state of self-stress. Let u^c_{ij} be the constrained displacement due to afore mentioned traction. This can be expressed in terms Green's function of a elastic body.

To obtain the stresses and strains in the entire body, the constrained field must be determined. The constrained strain is nothing but the total strain inside the inclusion and the matrix. The constrained strain in the matrix or inclusion is given by,

$$\varepsilon^c_{ij} = \frac{1}{2}\left(u^c_{i,j} + u^c_{j,i}\right) \tag{2.3.52}$$

The stress in the matrix is derived from Hooke's law as,

$$\sigma_{ij}^{c} = C_{ijkl}\varepsilon_{kl}^{c} \tag{2.3.53}$$

Eshelby's tensor $\boldsymbol{S}$ relates the constrained strain in the inclusion to eigenstrain,

$$\varepsilon_{ij}^{c} = S_{ijkl}\varepsilon_{ij}^{*} \tag{2.3.54}$$

Where, S_{ijkl} is referred to as Eshelby's tensor. It satisfies minor symmetries, but it does not satisfy the major symmetry.

$$S_{ijkl} = S_{jikl} = S_{ijlk}, \qquad \text{but} \qquad S_{ijkl} \neq S_{klij} \tag{2.3.55}$$

The stress in the inclusion is given by,

$$\sigma_{ij} = C_{ijkl}(\varepsilon_{kl}^{c} - \varepsilon_{kl}^{*}) \tag{2.3.56}$$

Eshelby[31] derived the components of $\boldsymbol{S}$ in terms of elliptic integrals of first and second kinds of amplitude and modulus for an isotropic material with ellipsoidal inclusion. Let the semi axes of the inclusion be a, b and c which is aligned with material coordinate axis x, y and z and assume that $a > b > c$.

$$S_{1111} = Qa^2 I_{aa} + RI_a,$$

$$S_{1122} = Qb^2 I_{ab} + RI_a,$$

$$S_{1133} = Qc^2 I_{ac} + RI_a,$$

$$S_{1212} = Q\frac{1}{2}(a^2 + b^2)I_{ab} + R\frac{1}{2}(I_a + I_b),$$

$$S_{1112} = S_{1223} = S_{1232} = 0$$

$$Q = \frac{3}{8\pi(1-\nu)}; \qquad R = \frac{1-2\nu}{8\pi(1-\nu)}; \qquad \frac{1}{3}Q + R = \frac{1}{4\pi}$$

$$I_a = \frac{4\pi abc}{(a^2-b^2)\sqrt{a^2-c^2}}\left(F(\theta,k) - E(\theta,k)\right)$$

$$I_c = \frac{4\pi abc}{(b^2-c^2)\sqrt{a^2-c^2}}\left(\frac{b\sqrt{a^2-c^2}}{ac} - E(\theta,k)\right)$$

$$\theta = \sin^{-1}\sqrt{\left(1 - \frac{c^2}{a^2}\right)}, \qquad k = \sqrt{\frac{a^2-b^2}{a^2-c^2}}$$

$$F(\theta,k) = \int_0^{\theta} \frac{dw}{\sqrt{1-k^2\sin^2 w}}$$

$$E(\theta,k) = \int_0^{\theta} \sqrt{1-k^2\sin^2 w}\, dw$$

$$I_a + I_b + I_c = 4\pi,$$

$$I_{aa} + I_{ab} + I_{ac} = \frac{4\pi}{3a^2},$$

$$a^2 I_{aa} + b^2 I_{ab} + c^2 I_{ac} = I_a,$$

$$I_b = 4\pi - I_a - I_c$$

$$I_{ab} = \frac{I_b - I_a}{3(a^2 - b^2)},$$

$$I_{aa} = \frac{4\pi}{3a^2} - I_{ab} - I_{ac}$$

The other non-zero components of the Eshelby tensor $\boldsymbol{S}$ and other components of I_{ij} are obtained by cyclic permutations of the above formulas.

Eshelby also proposed a relation for uniform rotation W^c in the inclusion in terms of eigenstrain and Eshelby's rotation tensor Π_{ijkl},

$$W^c_{ij} = \Pi_{ijkl}\varepsilon^*_{kl} \tag{2.3.58}$$

The rotation tensor Π_{ijkl} determines the spin of an isolated void in an infinite linear viscous matrix. The rotation tensor is symmetric with respect to the first two indices and skew-symmetric with respect to the last two. Also, the only non-zero components are Π_{1212}, Π_{2323} & Π_{3131}.

$$\Pi_{3131} = -\Pi_{1331} = \frac{I_a - I_c}{8\pi} \tag{2.3.59}$$

The above formulas for computation of Eshelby tensors are valid only when the axes of the coordinate system are parallel to the principal axes of the ellipsoid[31]. For any other system, the new components of the tensors have to computed using the general transformation laws.

2.3.4.3 Hashin-Shtrikman variational principal and bounds

As pointed out in the previous subsection, the effective properties of a material can be derived using different analytical methods. The effective property is not unique, as each analytical method leads to a different solution. It is important to know how good the obtained effective properties are. One way to reduce the space of possible solution is to obtain the bounds in which the properties could possibly lie. The variational bounds are obtained from the principal of minimum potential. Hashin-Shtrikman bounds are much narrow in comparison to other bounds like Voigt and Reuss. In this study, we restrict ourselves to Hashin-Shtrikman varational principal and bounds, pertaining to its usage in the constitutive model.

In this approach an appropriate auxiliary field which represents the deviation from a reference solution is considered to derive the bounds as opposed to other

methods where the total stress and strain fields are considered. This allows for more accurate approximations. A possible auxiliary field would be stress polarization $\boldsymbol{\tau}(x)$. It describes the deviation of the true stress in a heterogeneous material $\sigma_{ij} = C_{ijkl}\varepsilon_{kl}$ from the stress that would results when the true strain ε_{kl} acts on the homogeneous comparison material [35].

$$\boldsymbol{\tau}_(x) = \{\boldsymbol{C}(x) - \boldsymbol{C}^0\}\boldsymbol{\varepsilon}(x) \tag{2.3.60}$$

where, $\boldsymbol{C}^0$ is the elastic constant of the homogeneous comparison material. The strain $\boldsymbol{\varepsilon}(x)$ can be expressed in terms of fluctuation strain $\tilde{\boldsymbol{\varepsilon}}$ which is defined as,

$$\tilde{\boldsymbol{\varepsilon}} = \boldsymbol{\varepsilon} - \boldsymbol{\varepsilon}^0 \tag{2.3.61}$$

The stress difference is then defined as,

$$\tilde{\boldsymbol{\sigma}} = \boldsymbol{\sigma} - \boldsymbol{\sigma}^0 = \boldsymbol{C}(x)\boldsymbol{\varepsilon} - \boldsymbol{C}^0(x)\boldsymbol{\varepsilon}^0 \tag{2.3.62}$$

The difference field must satisfy the governing equation,

$$\tilde{\sigma}_{ij,j} = 0, \qquad \tilde{u}_i|_{\partial V} = 0 \tag{2.3.63}$$

The polarization is then given by,

$$\boldsymbol{\tau}_(x) = \{\boldsymbol{C}(x) - \boldsymbol{C}^0\} : \{\boldsymbol{\varepsilon}^0 + \tilde{\boldsymbol{\varepsilon}}\} \tag{2.3.64}$$

The solution to the governing equation Eq. (2.3.63) can be formally written as $\tilde{\boldsymbol{\varepsilon}}(\boldsymbol{\tau}(x))$. This gives the equation for $\boldsymbol{\tau}(x)$ which depends on macrostrain,

$$-\{\boldsymbol{C} - \boldsymbol{C}^0\}^{-1} : \boldsymbol{\tau} + \tilde{\boldsymbol{\varepsilon}}(\boldsymbol{\tau}) + \boldsymbol{\varepsilon}^0 = 0 \tag{2.3.65}$$

The above equation is equivalent to the Hashin-Shtrikman variational principle given by [35],

$$F(\hat{\boldsymbol{\tau}}) = \frac{1}{V}\int_V \{-\hat{\boldsymbol{\tau}} : (\boldsymbol{C} - \boldsymbol{C}^0)^{-1} : \hat{\boldsymbol{\tau}} + \hat{\boldsymbol{\tau}} : \tilde{\varepsilon}(\hat{\boldsymbol{\tau}}) + 2\hat{\boldsymbol{\tau}} : \boldsymbol{\varepsilon}^0\} dV = 0 \tag{2.3.66}$$

To obtain the effective properties $\tilde{\boldsymbol{C}}$, the stationary value of the above functional has to be computed. The stationary value is obtained to be,

$$F(\boldsymbol{\tau}) = \boldsymbol{\varepsilon}^0 : \left[\tilde{\boldsymbol{C}} - \boldsymbol{C}^0\right] : \boldsymbol{\varepsilon}^0 \tag{2.3.67}$$

$F(\boldsymbol{\tau})$ is maximum if $(\boldsymbol{C} - \boldsymbol{C}^0)$ is positive definite and minimum if $(\boldsymbol{C} - \boldsymbol{C}^0)$ is negative definite. Due to the boundary conditions in Eq. (2.3.63), the average value of strain fluctuation vanishes for any arbitrary $\hat{\boldsymbol{\tau}}$, i.e.

$$\frac{1}{V}\int_V \langle\hat{\boldsymbol{\tau}}\rangle : \tilde{\boldsymbol{\varepsilon}} dV = 0 \tag{2.3.68}$$

Hence, the variational principle can be written as

$$F(\hat{\boldsymbol{\tau}}) = \frac{1}{V}\int_V \{-\hat{\boldsymbol{\tau}} : (\boldsymbol{C} - \boldsymbol{C}^0)^{-1} : \hat{\boldsymbol{\tau}} + (\langle\hat{\boldsymbol{\tau}}\rangle - \hat{\boldsymbol{\tau}}) : \tilde{\varepsilon}(\hat{\boldsymbol{\tau}}) + 2\hat{\boldsymbol{\tau}} : \boldsymbol{\varepsilon}^0\} dV = 0 \tag{2.3.69}$$

Let us apply the variational principle to a matrix comprising of n distinct type of inclusions, with moduli $\boldsymbol{C}^{(r)}$, with volume concentrations $c^{(r)}$. The moduli of the matrix is taken as $\boldsymbol{C}^{n+1}$ with the volume concentration $c^{(n+1)}$. The material is taken to be statistically isotropic and stress polarization is given by a piece constant approximation $\hat{\boldsymbol{\tau}}(\boldsymbol{x}) = \boldsymbol{\tau}_r = const$ in $V^{(r)}$. When al the phases in the material are isotropic and the distribution of the inclusions in the infinite domain are isotropic, then making use of isotropic Eshelby tensor $\boldsymbol{S}$, the average fluctuation strain $\tilde{\boldsymbol{\varepsilon}}_r$ is given by,

$$\tilde{\boldsymbol{\varepsilon}}_r = -\boldsymbol{S} : (\boldsymbol{C}^0)^{-1} : \boldsymbol{\tau}_r \tag{2.3.70}$$

The variational functional then reduces to,

$$F(\boldsymbol{\tau}_r) = \sum_{r=1}^{n+1} c^{(r)} \boldsymbol{\tau}_r : \left(\boldsymbol{C}^{(r)} - \boldsymbol{C}^0\right)^{-1} : \boldsymbol{\tau}_r - \sum_{r=1}^{n+1} c^{(r)} (\langle \hat{\boldsymbol{\tau}} \rangle - \boldsymbol{\tau}_r) : \boldsymbol{S} : (\boldsymbol{C}^0)^{-1} : \boldsymbol{\tau}_r + 2 \langle \hat{\boldsymbol{\tau}} \rangle : \boldsymbol{\varepsilon}^0 \tag{2.3.71}$$

The above equation can be reformulated as,

$$\begin{aligned} F(\boldsymbol{\tau}_r) = \sum_{r=1}^{n+1} c^{(r)} \boldsymbol{\tau}_r : \left[\left(\boldsymbol{C}^{(r)} - \boldsymbol{C}^0\right)^{-1} + \boldsymbol{S} : (\boldsymbol{C}^0)^{-1} \right] : \boldsymbol{\tau}_r - \\ \sum_{r=1}^{n+1} \sum_{s=1}^{n+1} c^{(r)} c^{(s)} \boldsymbol{\tau}_r : \boldsymbol{S} : (\boldsymbol{C}^0)^{-1} : \boldsymbol{\tau}_s - 2 \sum_{r=1}^{n+1} c^{(r)} \boldsymbol{\tau}_r : \boldsymbol{\varepsilon}^0 \end{aligned} \tag{2.3.72}$$

To obtain the bounds from Eq. (2.3.67), the values of $\boldsymbol{\tau}_r$ should be chosen in such that the functional $F(\boldsymbol{\tau}_r)$ becomes extremal.

$$\frac{\partial F}{\partial \boldsymbol{\tau}_r} = 0 \tag{2.3.73}$$

This yields $n+1$ equations for obtaining appropriate values of $\boldsymbol{\tau}_r$,

$$\boldsymbol{\tau}_r : \left[\left(\boldsymbol{C}^{(r)} - \boldsymbol{C}^0\right)^{-1} + \boldsymbol{S} : (\boldsymbol{C}^0)^{-1} \right] - \langle \hat{\boldsymbol{\tau}} \rangle : \boldsymbol{S} : (\boldsymbol{C}^0)^{-1} = \boldsymbol{\varepsilon}_0 \tag{2.3.74}$$

The upper and lower bounds of the effective properties are obtained by substituting the above equation in Eq. (2.3.67). The effective elastic constant is given by,

$$\begin{aligned} \tilde{\boldsymbol{C}} = \left(\sum_{r=1}^{n+1} c^{(r)} \boldsymbol{C}^{(r)} \left[\mathbb{I} + \boldsymbol{S} : (\boldsymbol{C}^0)^{-1} : (\boldsymbol{C}^{(r)} - \boldsymbol{C}^0) \right]^{-1} \right) \times \\ \left(\sum_{s=1}^{n+1} c^{(s)} \left[\mathbb{I} + \boldsymbol{S} : (\boldsymbol{C}^0)^{-1} : (\boldsymbol{C}^{(s)} - \boldsymbol{C}^0) \right]^{-1} \right)^{-1} \end{aligned} \tag{2.3.75}$$

The above result is Walpole's generalization of Hashin and Shtrikman's results [68].

In this study, determination of effective properties for a matrix containing vacuous inclusions (voids) is trivial. Let the volume V consist of a matrix with elastic constant $\boldsymbol{C}_M = \boldsymbol{C}$, and a vacuous inclusion with elastic constant $\boldsymbol{C}_v = 0$ and volume fraction $c^{(v)} = f$. Also, let the elastic constant of the equivalent linear homogeneous

volume be the same as that of the matrix in inhomogeneous volume V i.e. $\boldsymbol{C}^0 = \boldsymbol{C}$. Then the equivalent elastic constant is derived as,

$$\tilde{\boldsymbol{C}} = \left(c^{(v)}\boldsymbol{C}_v\left[\mathbb{I} + \boldsymbol{S} : \boldsymbol{C}_M^{-1} : (\boldsymbol{C}_v - \boldsymbol{C}_M)\right]^{-1} + c^{(M)}\boldsymbol{C}_M\left[\mathbb{I} + \boldsymbol{S} : \boldsymbol{C}_M^{-1} : (\boldsymbol{C}_M - \boldsymbol{C}_M)\right]^{-1}\right) \times \left(c^{(v)}\left[\mathbb{I} + \boldsymbol{S} : \boldsymbol{C}_M^{-1} : (\boldsymbol{C}_v - \boldsymbol{C}_M)\right]^{-1} + c^{(M)}\left[\mathbb{I} + \boldsymbol{S} : \boldsymbol{C}_M^{-1} : (\boldsymbol{C}_M - \boldsymbol{C}_M)\right]^{-1}\right)^{-1}$$

$$\tilde{\boldsymbol{C}} = \left((1-f)\boldsymbol{C} : [\mathbb{I}]^{-1}\right)\left(f\left[\mathbb{I} + \boldsymbol{S} : \boldsymbol{C}_M^{-1} : -\boldsymbol{C}_M\right]^{-1} + (1-f)\left[\mathbb{I}\right]^{-1}\right)^{-1}$$

$$\tilde{\boldsymbol{C}} = \left[\frac{f}{(1-f)}\left[\boldsymbol{C} : (\mathbb{I} - \boldsymbol{S})\right]^{-1} + \boldsymbol{C}^{-1}\right]^{-1} \tag{2.3.76}$$

The pioneering work of Hill[39] is very important in this context. Hill gave a theoretical solution for the internal inhomogeneities of stress and strain in an arbitrarily deformed aggregate of elasto-plastic crystals. He defined the quantity $\boldsymbol{Q}$ as,

$$\boldsymbol{Q} = \boldsymbol{C} : (\mathbb{I} - \boldsymbol{S}) \tag{2.3.77}$$

$\boldsymbol{Q}$ exhibits both minor and major symmetries. Substituting $\boldsymbol{Q}$ in Eq. (2.3.76),

$$\tilde{\boldsymbol{C}} = \left[\frac{f}{(1-f)}\boldsymbol{Q}^{-1} + \boldsymbol{C}^{-1}\right]^{-1} \tag{2.3.78}$$

The inverse of the above relation, in terms of compliance tensor $\tilde{\boldsymbol{M}}$ also holds. The solution for $\tilde{\boldsymbol{M}}$ is later used in the constitutive equation.

$$\tilde{\boldsymbol{M}} = \boldsymbol{M} + \frac{f}{(1-f)}\boldsymbol{Q}^{-1} \tag{2.3.79}$$

The analytical expression for calculation of non-zero components of $\boldsymbol{Q}$ for a coordinate system parallel to the principal axes of an ellipsoid is given by [4],

$$Q_{1111} = \frac{\mu}{4\pi(1-\nu)}(8\pi - I_a - 3a^2 I_{aa}), \tag{2.3.80}$$

$$Q_{1122} = \frac{\mu}{8\pi(1-\nu)}(16\pi\nu + (1-4\nu)(I_a + I_b) - 3(a^2+b^2)I_{ab}), \tag{2.3.81}$$

$$Q_{1212} = \frac{\mu}{8\pi(1-\nu)}(8\pi(1-\nu) - (1-2\nu)(I_a + I_b) - 3(a^2+b^2)I_{ab}), \tag{2.3.82}$$

The variables in the formulae are described in Subsection(2.3.4.2).
Hill[39] also introduced the concept of concetration-factor tensors $\boldsymbol{A}$ and $\boldsymbol{B}$, which relates the average strain rate and stress rate in an inclusion r to overall uniform strain rate and stress rate respectively.

$$\boldsymbol{D}^{(r)} = \boldsymbol{A}^{(r)} : \bar{\boldsymbol{D}} \qquad \text{and} \qquad \dot{\boldsymbol{\sigma}}^{(r)} = \boldsymbol{B}^{(r)} : \dot{\bar{\boldsymbol{\sigma}}} \tag{2.3.83}$$

The average strain-rate and spin over phase r from Hashin-Shtrikman variational principal is given by [43],

$$\bar{\boldsymbol{D}}^{(r)} = \bar{\boldsymbol{D}} - \frac{1}{c^{(r)}} \sum_{s=1}^{n+1} \boldsymbol{E}^{(rs)} \boldsymbol{\tau}^s \quad \text{and} \quad \bar{\boldsymbol{W}}^{(r)} = \bar{\boldsymbol{W}} - \frac{1}{c^{(r)}} \sum_{s=1}^{n+1} \boldsymbol{F}^{(rs)} \boldsymbol{\tau}^s \tag{2.3.84}$$

Where $\boldsymbol{E}^{rs}$ and $\boldsymbol{F}^{rs}$ are symmetric fourth-order tensors. In terms of strain concentration tensor $\boldsymbol{A}$, the Hashin-Shtrikman estimate given in Eq. (2.3.75) can be expressed as,

$$\tilde{\boldsymbol{C}} = \sum_{r=1}^{n+1} c^{(r)} \boldsymbol{C}^{(r)} \boldsymbol{A}^{(r)} \tag{2.3.85}$$

where,

$$\boldsymbol{A}^{(r)} = \hat{\boldsymbol{A}}^{(r)} \left(\sum_{s=1}^{n+1} c^{(s)} \hat{\boldsymbol{A}}^s \right)^{-1} \tag{2.3.86}$$

$$\hat{\boldsymbol{A}} = [\mathbb{I} + \boldsymbol{S} : \boldsymbol{C}^{0^{-1}} : (\boldsymbol{C}^{(r)} - \boldsymbol{C}^0)]^{-1} \tag{2.3.87}$$

The strain rate concentration tensor satisfies the relation,

$$\sum_{r=1}^{n+1} c^{(r)} \boldsymbol{A}^{(r)} = \mathbb{I} \tag{2.3.88}$$

In our case, the concentration tensor in void phase is,

$$\boldsymbol{A}^{(v)} = \hat{\boldsymbol{A}}^{(v)} \left[(1-f) \hat{\boldsymbol{A}}^{(M)} + f \hat{\boldsymbol{A}}^{(v)} \right] \tag{2.3.89}$$

But,

$$\hat{\boldsymbol{A}}^{(v)} = [\mathbb{I} - \boldsymbol{S}]^{-1} \qquad \text{and} \qquad \hat{\boldsymbol{A}}^{(M)} = \mathbb{I} \tag{2.3.90}$$

Hence, the concentration tensor reduces to

$$\boldsymbol{A}^{(v)} = [\mathbb{I} - (1-f)\boldsymbol{S}]^{-1} \tag{2.3.91}$$

Kailasam and Ponte Castañeda [43] introduced the concept of spin-concentration tensor $\boldsymbol{\mathcal{C}}^{(r)}$, analogous to strain-rate concentration tensor

$$\bar{\boldsymbol{W}}^{(r)} = \bar{\boldsymbol{W}} - \boldsymbol{\mathcal{C}}^{(r)} \bar{\boldsymbol{D}} \tag{2.3.92}$$

where,

$$\sum_{r=1}^{n+1} c^{(r)} \boldsymbol{C}^{(r)} = 0 \tag{2.3.93}$$

For a two-phase particulate composite, the spin concentration tensor in second phase is given by,

$$\boldsymbol{\mathcal{C}}^{(2)} = (1 - c^{(2)}) \boldsymbol{\Pi} \left[\boldsymbol{C}^{(2)} - \boldsymbol{C}^{(1)} \right] [\boldsymbol{A}^{(2)}] \tag{2.3.94}$$

For a porous material, the second phase is vacuous, and considering our previous assumptions, the spin concentration tensor reduces to,

$$\boldsymbol{\mathcal{C}}^{(2)} = -(1-f)\boldsymbol{\Pi} : \boldsymbol{A}^{(2)} \tag{2.3.95}$$

2.3.4.4 Effective Properties of nonlinear heterogeneous material

The rigorous bounds for effective properties of nonlinear heterogeneous materials was first provided by Talbot and Willis who extended the Hashin-Shtrikman variational principles to include nonlinear behaviour of materials[16]. Ponte Castañeda extended the Talbot-Willis variational principle to finite elasticity which provided bounds for wide range of nonlinear elastic materials. Later on he proposed an alternate variational principal that provided the estimates of effective energy potential of nonlinear materials in terms of equivalent linear materials with the same microstructural distribution. This variational principal is the base for the constitutive model described in the preceding sections.

For an n phase matrix in volume V with each phase occupying a subdomain $V^{(r)}$, the stress potential $U(\boldsymbol{\sigma}, \boldsymbol{x})$ is expressed in terms of n homogeneous phase potentials $U^{(r)}(\boldsymbol{\sigma})$ by,

$$U(\boldsymbol{\sigma}, \boldsymbol{x}) = \sum_{r=1}^{n} \chi^{(r)}(\boldsymbol{x}) U^{(r)}(\boldsymbol{\sigma}) \tag{2.3.96}$$

where $\chi^{(r)}$ is characteristic function of phase r,

$$\chi^{(r)} = \begin{cases} 1 & \text{if} \quad \boldsymbol{x} \in V^{(r)} \\ 0 & \text{otherwise} \end{cases} \tag{2.3.97}$$

Here, the phases are assumed to be isotropic, hence the potentials $U^{(r)}(\boldsymbol{\sigma})$ depend on stress through the three principal invariants. A further assumption is that the potential depends on stress through the two invariants Equivalent stress (σ_{eq}) and mean stress (σ_m).
The behaviour of nonlinear viscous material under large deformations is characterized by the relation,

$$\boldsymbol{D} = \frac{\partial U(\boldsymbol{\sigma}, \boldsymbol{x})}{\partial \boldsymbol{\sigma}} \tag{2.3.98}$$

U can take the common power-law form,

$$U(\boldsymbol{\sigma}, \boldsymbol{x}) = \frac{\sigma_y(\boldsymbol{x})}{n+1} \left(\frac{\sigma_{eq}}{\sigma_y(\boldsymbol{x})} \right)^{n+1} \tag{2.3.99}$$

$n = 1$ describes a linear viscous material and $n = \infty$ describes a rigid-perfectly J_2 plastic material with tensile yield stress σ_y. The effective stress-strain-rate relation is given by,

$$\bar{\boldsymbol{D}} = \frac{\partial \tilde{U}(\bar{\boldsymbol{\sigma}})}{\partial \bar{\boldsymbol{\sigma}}} \tag{2.3.100}$$

where, $\bar{\boldsymbol{\sigma}}$ is the average stress, $\bar{\boldsymbol{D}}$ average strain rate, and $\tilde{U}$ is the effective energy potential. According to principle of minimum complementary energy introduced by Hill, for a strictly convex nonlinear potential $U(\boldsymbol{\sigma}, \boldsymbol{x})$, the effective potential must satisfy the following condition,

$$\tilde{U}(\bar{\boldsymbol{\sigma}}) = \min_{\boldsymbol{\sigma} \in S(\boldsymbol{\sigma})} \int_V U(\boldsymbol{\sigma}, \boldsymbol{x}) dv = \inf_{\boldsymbol{\sigma} \in S(\boldsymbol{\sigma})} \bar{U}(\boldsymbol{\sigma}) \tag{2.3.101}$$

where,

$$S(\boldsymbol{\sigma}) = \{\boldsymbol{\sigma} | \nabla \cdot \boldsymbol{\sigma} = 0 \text{ in } V, \text{ and } \boldsymbol{\sigma}\boldsymbol{n} = \bar{\boldsymbol{\sigma}}\boldsymbol{n} \text{ on } \partial V\} \tag{2.3.102}$$

is the admissible stress corresponding to the uniform stress $\bar{\boldsymbol{\sigma}}$ on the boundary. Since the effective stress-strain-rate relation depends is related to effective energy potential, the information regarding the effective energy potential $\tilde{U}(\bar{\boldsymbol{\sigma}})$ is crucial. For linear behaviour ($n = 1$), the effective potential is given in terms of effective elasticity tensor,

$$\tilde{U}(\bar{\boldsymbol{\sigma}}) = \frac{1}{2} \bar{\boldsymbol{\sigma}} \cdot (\tilde{\boldsymbol{C}}^{-1} \bar{\boldsymbol{\sigma}}) \tag{2.3.103}$$

Similarly, for a rigid perfect solid, the effective stress potential is given by,

$$\tilde{U}(\bar{\boldsymbol{\sigma}}) = \begin{cases} 0 & \text{if } \bar{\boldsymbol{\sigma}} \in \tilde{P}, \\ \infty & \text{otherwise} \end{cases} \tag{2.3.104}$$

The boundary $\tilde{P}$ is defined by the effective yield function,

$$\tilde{\Phi}(\bar{\boldsymbol{\sigma}}) = 0 \tag{2.3.105}$$

which gives us,

$$\bar{\boldsymbol{D}} = \dot{\Lambda} \frac{\partial \tilde{\Phi}(\bar{\boldsymbol{\sigma}})}{\partial \bar{\boldsymbol{\sigma}}} \tag{2.3.106}$$

Ponte Castañeda Variational Principle

For a nonlinear heterogeneous material, Ponte Castañeda [16] proposed a new variational formulation for the effective potential in Eq.(2.3.101) in terms of effective potential of equivalent class of linear comparison heterogeneous material, with the same phase distribution. This variational formulation gives the lower bounds for the effective stress potentials of nonlinear heterogeneous materials. The stress potential for each phase of the linear comparison material is assumed to be quadratic,

$$\hat{U}^{(r)}(\boldsymbol{\sigma}) = \frac{1}{6\mu^{(r)}} \sigma_{eq}^2 + \frac{1}{2\kappa^{(r)}} \sigma_m^2 \tag{2.3.107}$$

where, $\mu^{(r)}$ and $\kappa^{(r)}$ are the shear and bulk modulus of the linear isotropic composite. To account for nonlinearity in the original stress potential, which is of higher order than quadratic form, Ponte Castañeda defined the set of functions,

$$V^{(r)}(\mu^{(r)}, \kappa^{(r)}) = \sup_{\boldsymbol{\sigma}} \left\{ \hat{U}^{(r)}(\boldsymbol{\sigma}) - U^{(r)}(\boldsymbol{\sigma}) \right\} \tag{2.3.108}$$

where $U^{(r)}(\boldsymbol{\sigma})$ is the potential of actual nonlinear phase. The proposed variational principal takes the form,

$$\tilde{U}(\bar{\boldsymbol{\sigma}}) \geq \max_{\mu^{(r)},\kappa^{(r)}>0} \left\{ \tilde{\hat{U}}(\bar{\boldsymbol{\sigma}}) - \sum_{r=1}^{n} c^{(r)} V^{(r)}(\mu^{(r)}, \kappa^{(r)}) \right\} \tag{2.3.109}$$

$\tilde{\hat{U}}(\bar{\boldsymbol{\sigma}})$ is the effective potential of the linear comparison material. The bounds of the effective potential of the linear comparison material can be obtained from the well developed linear homogenization techniques. Eq.2.3.109 can be reformulated as

$$\tilde{U}(\bar{\boldsymbol{\sigma}}) \geq \max_{\mu^{(r)},\kappa^{(r)}>0} \left\{ \frac{1}{2}\bar{\boldsymbol{\sigma}} \cdot (\tilde{\boldsymbol{C}}^{-1}\bar{\boldsymbol{\sigma}}) - \sum_{r=1}^{n+1} c^{(r)} V^{(r)}(\mu^{(r)}, \kappa^{(r)}) \right\} \tag{2.3.110}$$

$\tilde{\boldsymbol{C}}^{-1}$ denotes the upper bound for effective elasticity tensor of the linear material with same distribution of microstructure as the non linear material. For example, the Hashin Shtrikman bounds introduced in the previous section can be used for $\tilde{\boldsymbol{C}}^{-1}$. Hence, a linear upper bound for effective elasticity tensor of an equivalent linear material can be used to derive the lower bounds of effective stress potential of the nonlinear material. For a perfectly plastic and power law material, the variables depend only on shear modulus. Hence Eq.2.3.110 reduces to,

$$\tilde{U}(\bar{\boldsymbol{\sigma}}) \geq \max_{\mu^{(r)}>0} \left\{ \frac{1}{2}\bar{\boldsymbol{\sigma}} \cdot (\tilde{\boldsymbol{C}}^{-1}\bar{\boldsymbol{\sigma}}) - \sum_{r=1}^{n+1} c^{(r)} V^{(r)}(\mu^{(r)}) \right\} \tag{2.3.111}$$

The effective stress strain rate relation for a nonlinear material can be written as [43],

$$\bar{\boldsymbol{\sigma}} = \tilde{\boldsymbol{C}}(\hat{\mu})\bar{\boldsymbol{D}} \tag{2.3.112}$$

Where $\hat{\mu}$ is obtained from the stationary condition,

$$\frac{1}{2}\bar{\boldsymbol{\sigma}} \cdot \left[\delta\tilde{\boldsymbol{C}}^{-1}(\hat{\mu})\bar{\boldsymbol{\sigma}}\right] - \left\langle \frac{\partial V(\hat{\mu})}{\partial \mu}\delta\mu \right\rangle = 0 \tag{2.3.113}$$

For a 2 phase nonlinear material with volume fractions $c^{(1)}$ and $c^{(2)}$, and stress potentials $U^{(1)}(\boldsymbol{\sigma})$ and $U^{(2)}(\boldsymbol{\sigma})$, the variational principle gives the following lower bound,

$$\tilde{U}(\bar{\boldsymbol{\sigma}}) \geq \max_{\mu^{(r)},\kappa^{(r)}>0} \left\{ \frac{1}{2}\bar{\boldsymbol{\sigma}} \cdot (\tilde{\boldsymbol{C}}^{-1}\bar{\boldsymbol{\sigma}}) - \sum_{r=1}^{2} c^{(r)} V^{(r)}(\mu^{(r)}, \kappa^{(r)}) \right\} \tag{2.3.114}$$

In the context of this study, one of the phases in the nonlinear heterogeneous material is considered to be vacuous (porous material) and the matrix is considered to be incompressible and isotropic. The stress potential of the vacuous phase is given by $U^{(2)} = 0$ and the stress potential of the matrix is assumed to be of the form $U^{(1)}(\boldsymbol{\sigma}) = \varphi(\sigma_{eq}^2)$. Then stress potential of the linear comparison incompressible matrix will take the form,

$$\hat{U}^{(1)}(\boldsymbol{\sigma}) = \frac{1}{6\mu^{(1)}}\sigma_{eq}^2 \tag{2.3.115}$$

The effective stress potential is then given by,

$$\tilde{U}(\bar{\boldsymbol{\sigma}}) \geq \left\{ \tilde{\hat{U}}(\bar{\boldsymbol{\sigma}}) - c^{(1)} V^{(1)} \right\} \tag{2.3.116}$$

Which can be reformulated into,

$$\tilde{U}(\bar{\boldsymbol{\sigma}}) \geq c^{(1)} \left\{ \frac{1}{c^{(1)}} \tilde{\hat{U}}(\bar{\boldsymbol{\sigma}}) - V^{(1)}(\mu^{(r)}) \right\} \tag{2.3.117}$$

For a linear composite with ellipsoidal microstructure, Hashin-Shtrikman estimates described in the previous section can be used for $\tilde{\hat{U}}$. Also, let f be the volume fraction of the vacuous phase, then $(1-f)$ is the volume fraction of the matrix. The above equation then reduces to [19],

$$\tilde{U}(\bar{\boldsymbol{\sigma}}) \geq (1-f)\varphi\left(\frac{H}{1-f}\right) \tag{2.3.118}$$

where,

$$\frac{1}{6\mu^{(1)}} H = \frac{1}{2}\,\bar{\boldsymbol{\sigma}} \cdot \left\{ \left[\frac{f}{(1-f)} \left[\boldsymbol{C} : (\mathbb{I} - \boldsymbol{S}) \right]^{-1} + \boldsymbol{C}^{-1} \right] \bar{\boldsymbol{\sigma}} \right\} \tag{2.3.119}$$

The lower bounds on the potentials provide the upper bounds on the ultimate yield surface. The effective yield surface can be obtained from Eq. (2.3.104), i.e., by equating the above equation to zero, and considering Eq. (2.3.105), we obtain the upper bound of yield surface to be,

$$\tilde{\Phi} = \frac{H}{1-f} - \sigma_y^2 = \frac{1}{1-f} \bar{\boldsymbol{\sigma}} \cdot \tilde{\boldsymbol{m}} \bar{\boldsymbol{\sigma}} - \sigma_y^2 \tag{2.3.120}$$

2.4 Description of the Constitutive Model

In the following section, the elastic-plastic constitutive model for porous metals as proposed by Kailasam & Ponte Castañeda [42], and Aravas & Ponte Castañeda [4] is described. The structure followed in this section is similar to the structure followed by the authors in their original paper.

The constitutive model is an extension of initial models of Ponte Castañeda and group, which was developed for a rigid-perfectly plastic material. For porous metals, it is assumed that the vacuous inclusions do not store any energy and hence the elastic effect in the material is solely due to the elastic properties of the matrix phase. In comparison to plastic deformation, the elastic deformation is considered to be small. These considerations facilitate the evaluation of elastic and plastic response of the material individually, and to be clubbed later on to generate the complete elastic-plastic response. It is observed that, under finite deformation, the evolution of microstructure in the material is only due to plastic deformation [42].

The constitutive equations are derived using Ponte Castañeda variational principle introduced in the previous section, i.e. the effective properties of nonlinear

porous material is obtained in terms of effective properties of an equivalent linear comparison composite with the same distribution of microstructure. The effective properties of the equivalent linear comparison composite is in turn obtained from Hashin-Shtrikamn estimates for particulate microstructures developed by Willis [68], and Ponte Castañeda & Willis [18].

The vacuous inclusions, referred to as voids henceforth, are assumed to be initially ellipsoidal in shape and are uniformly distributed in an isotropic metal matrix. At every material point in the homogenized metal, a representative local ellipsoidal void is defined. The porosity of the metal is quantified by the void volume fraction f.

$$f = \frac{\text{Total volume of voids}}{\text{Volume of the heterogeneous material}} \tag{2.4.1}$$

Let a,b and c be the half lengths of the principal axes of the voids, and $\boldsymbol{n}^{(1)}$, $\boldsymbol{n}^{(2)}$ and $\boldsymbol{n}^{(3)}$ be the unit vectors along the principal axes. The unit vector in the third direction satisfies,

$$\boldsymbol{n}^{(3)} = \boldsymbol{n}^{(1)} \times \boldsymbol{n}^{(2)} \tag{2.4.2}$$

It is difficult and cumbersome to account for evolution of size of voids through the lengths of principal axes directly. An approximation, which is much simpler and less time consuming would be to consider the aspect ratios of the principal axes. The aspect ratios w_1 and w_2 are given by,

$$w_1 = \frac{c}{a} \qquad \text{and} \qquad w_2 = \frac{c}{b} \tag{2.4.3}$$

To make use of the simplified linear-elastic estimates of Willis[68], it is necessary that the ellipsoidal inclusions be aligned and the two point correlation function which describes the distribution of void centres be ellipsoidal i.e. the shape and orientation of the two-point correlation function which describes the distribution of voids is identical to the shape and orientation of voids themselves. It is to be noted that the voids and the distributions of their centres are assumed to have identical aspect ratios (in Fig.(2.4.1) $c/b = C/B$). Due to this restriction, the voids and their distribution function evolve identically when the material deforms. Hence, the porous material maintains local orthotropic symmetry, with the axes of orthotropy aligned with the principal axes of voids.

The internal variables that characterize the local state of homogenized porous metal are,

$$s = \left\{\varepsilon^p_{eq}, f, w_1, w_2, \boldsymbol{n}^{(1)}, \boldsymbol{n}^{(2)}, \boldsymbol{n}^{(3)}\right\} \tag{2.4.4}$$

The rate of deformation $\boldsymbol{D}$ at every point in the homogenized porous material is additively decomposed in to elastic and plastic part.

$$\boldsymbol{D} = \boldsymbol{D}^e + \boldsymbol{D}^p \tag{2.4.5}$$

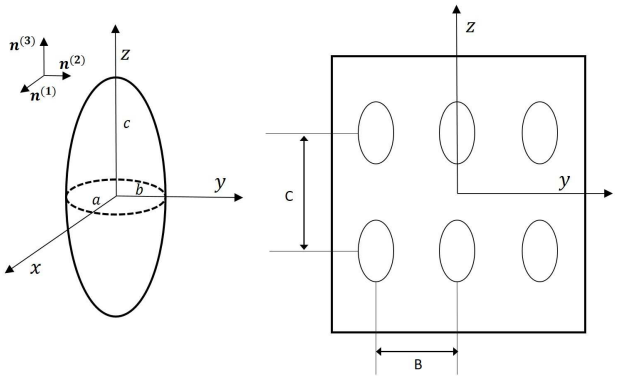

Fig. 2.4.1: Void Geometry and distribution of voids in the matrix [19]

2.4.1 Elastic Constitutive Relation

Hypoelastic formulation as introduced in 2.3.3.1, is used to describe the elastic part of rate-of-deformation tensor.

$$\boldsymbol{D}^e = \boldsymbol{M}^e : \overset{\circ}{\boldsymbol{\sigma}} \tag{2.4.6}$$

where $\boldsymbol{M}^e$ is the effective compliance tensor and $\overset{\circ}{\boldsymbol{\sigma}}$ is a corotational rate of Cauchy stress tensor, corotational with the spin of the voids $\boldsymbol{\omega}$ relative to a fixed laboratory frame.

$$\overset{\circ}{\boldsymbol{\sigma}} = \dot{\boldsymbol{\sigma}} - \boldsymbol{\omega}\cdot\boldsymbol{\sigma} + \boldsymbol{\sigma}\cdot\boldsymbol{\omega} \tag{2.4.7}$$

Due to the assumption of ellipsoidal symmetric distribution of voids, the generic Hashin-Shtrikman estimate proposed by Willis[68] (Eq.2.3.79) could be used for the effective compliance tensor ($\tilde{\boldsymbol{M}} = \boldsymbol{M}^e$).

$$\boldsymbol{M}^e = \boldsymbol{M} + \frac{f}{(1-f)}\boldsymbol{Q}^{-1} \tag{2.4.8}$$

Here $\boldsymbol{Q}$ is the Eshelby tensor defined in Eq.2.3.77 and $\boldsymbol{M}$ is the elastic compliance tensor of the matrix material, which is given by the inverse of elastic modulus $\boldsymbol{C}$. For an isotropic material,

$$\boldsymbol{C} = 2\mu\boldsymbol{K} + 3\kappa\boldsymbol{J} \implies \boldsymbol{M} = \frac{1}{2\mu}\boldsymbol{K} + \frac{1}{3\kappa}\boldsymbol{J} = \frac{1}{2\mu}\left(\boldsymbol{K} + \frac{1-2\nu}{1+\nu}\boldsymbol{J}\right) \tag{2.4.9}$$

μ, κ and ν are the elastic shear modulus, bulk modulus and Poisson's ratio of the matrix. $\boldsymbol{K}$ and $\boldsymbol{J}$ are the volumetric and deviatoric 4th order identity tensors given by,

$$\mathrm{J} = \frac{1}{3}\boldsymbol{I}\otimes\boldsymbol{I} \qquad \text{and} \qquad \boldsymbol{K} = \mathbb{I} - \frac{1}{3}\boldsymbol{I}\otimes\boldsymbol{I} \tag{2.4.10}$$

It is to be noted that $\mathbb{I}$ is the symmetric fourth order identity tensor, as the stress and strain tensors are in symmetric space. A derivative of a symmetric second order tensor with respect to itself would result in a symmetric fourth order identity tensor. For any arbitrary fourth order identity tensor $\boldsymbol{A}$,

$$\frac{\partial \boldsymbol{A}^{sym}}{\partial \boldsymbol{A}^{sym}} = \mathbb{I} \tag{2.4.11}$$

where,

$$\mathbb{I}_{ijkl} = (\delta_{ik}\delta_{jl} + \delta_{il}\delta_{jk})/2 \tag{2.4.12}$$

In voigt notation, $\boldsymbol{J}$ and $\boldsymbol{K}$ are given by,

$$\boldsymbol{J} = \begin{bmatrix} 1 & 1 & 1 & 0 & 0 & 0 \\ 1 & 1 & 1 & 0 & 0 & 0 \\ 1 & 1 & 1 & 0 & 0 & 0 \\ 0 & 0 & 0 & 0 & 0 & 0 \\ 0 & 0 & 0 & 0 & 0 & 0 \\ 0 & 0 & 0 & 0 & 0 & 0 \end{bmatrix} \tag{2.4.13}$$

$$\boldsymbol{K} = \begin{bmatrix} 2/3 & -1/3 & -1/3 & 0 & 0 & 0 \\ -1/3 & 2/3 & -1/3 & 0 & 0 & 0 \\ -1/3 & -1/3 & 2/3 & 0 & 0 & 0 \\ 0 & 0 & 0 & 1/2 & 0 & 0 \\ 0 & 0 & 0 & 0 & 1/2 & 0 \\ 0 & 0 & 0 & 0 & 0 & 1/2 \end{bmatrix} \tag{2.4.14}$$

Some important observations are,

1) Eshelby tensor $\boldsymbol{S}$ satisfies the conditions for minor symmetries, and it depends on Poisson's ratio ν , aspect ratios (w_1, w_2) and void principal axes ($\boldsymbol{n}_1$, $\boldsymbol{n}_2$, $\boldsymbol{n}_3$)

2) Eshelby tensor $\boldsymbol{Q}$ exhibits minor and major symmetries, and depends on shear modulus ν, Poisson's ratio ν , aspect ratios (w_1, w_2) and void principal axes ($\boldsymbol{n}_1$, $\boldsymbol{n}_2$, $\boldsymbol{n}_3$)

3) The effective compliance tensor $\boldsymbol{M}^e$ depends on void volume fraction f, and shape and orientation of the voids. The effective compliance tensor evolves with change in micro-structure hence it accounts for the influence of microstructure in the elastic regime.

2.4.2 Yield Condition and Plastic Flow Rule

Using the variational principle proposed by Ponte Castañeda [16], the upper bound for effective yield function was derived in Section 2.3.4.4 (Eq.2.3.120). Here, the effective yield function depends on the internal variables, and considering isotropic hardening of the matrix material, the effective yield function is given by,

$$\Phi(\boldsymbol{\sigma}, \boldsymbol{s}) = \frac{1}{1-f}\boldsymbol{\sigma} : \boldsymbol{m} : \boldsymbol{\sigma} - \sigma_y^2(\varepsilon_{eq}^p) \tag{2.4.15}$$

It is important to note that the yield function is isotropic. σ_y is the yield function of the matrix under uniaxial tension. The yield function depends of equivalent plastic strain ε_{eq}^p which accounts for the isotropic hardening. $\boldsymbol{m}$ is a normalized effective viscous compliance tensor of linear comparison porous material. Since the matrix phase is taken to be incompressible in plastic region, Poisson's ratio has to be set to

$\nu = 1/2$.

$$\begin{aligned}\boldsymbol{m} &= \boldsymbol{m}\left(f, w_1, w_2, \boldsymbol{n}^{(1)}, \boldsymbol{n}^{(2)}, \boldsymbol{n}^{(3)}\right) \\ &= 3\mu \boldsymbol{M}^e|_{\nu=1/2} \\ &= 3\mu \left(\frac{1}{2\mu}\left(\boldsymbol{K} + \frac{1-2\nu}{1+\nu}\boldsymbol{J}\right) + \frac{f}{(1-f)}\boldsymbol{Q}^{-1}\right)_{\nu=1/2}\end{aligned} \tag{2.4.16}$$

Hence,

$$\boldsymbol{m} = \frac{3}{2}\boldsymbol{K} + \frac{3f}{1-f}\mu \boldsymbol{Q}^{-1}|_{\nu=1/2} \tag{2.4.17}$$

The numerical complications in evaluating $\boldsymbol{Q}$ at $\nu = 1/2$ can be avoided by using the explicit equations given in Section 2.3.4. The plastic rate-of-deformation is obtained from the normality rule (Eq.2.3.35),

$$\boldsymbol{D}^p = \dot{\Lambda}\boldsymbol{N} \tag{2.4.18}$$

where,

$$\boldsymbol{N} = \frac{\partial \Phi}{\partial \boldsymbol{\sigma}} = \frac{2}{1-f}\boldsymbol{m} : \boldsymbol{\sigma} \tag{2.4.19}$$

Special Case: Spherical Voids

The yield function can be reduced to a simpler form when the aspect ratios are $w_1 = w_2 = 1$. In this case the Eshelby tensor $\boldsymbol{Q}$ is given by [4],

$$\boldsymbol{Q}(\mu, \nu) = 2\mu\left(\frac{7-5\nu}{15(1-\nu)}\boldsymbol{K} + \frac{2(1+\nu)}{3(1-\nu)}\boldsymbol{J}\right) \tag{2.4.20}$$

Therefore,

$$\boldsymbol{Q}^{-1}(\mu, \nu) = \frac{1}{2\mu}\left(\frac{15(1-\nu)}{7-5\nu}\boldsymbol{K} + \frac{3(1-\nu)}{2(1+\nu)}\boldsymbol{J}\right) \tag{2.4.21}$$

$$\boldsymbol{Q}^{-1}(\mu, \nu)|_{\nu=1/2} = \frac{1}{2\mu}\left(\frac{5}{3}\boldsymbol{K} + \frac{1}{2}\boldsymbol{J}\right) \tag{2.4.22}$$

Substituting in Eq.2.4.17, for spherical case we obtain,

$$\boldsymbol{m} = \frac{3+2f}{2(1-f)}\boldsymbol{K} + \frac{3f}{4(1-f)}\boldsymbol{J} \tag{2.4.23}$$

The yield function is then given by,

$$\Phi(\boldsymbol{\sigma}, \boldsymbol{s}) = \frac{1}{1-f}\boldsymbol{\sigma} : \left[\frac{3+2f}{2(1-f)}\boldsymbol{K} + \frac{3f}{4(1-f)}\boldsymbol{J}\right] : \boldsymbol{\sigma} - \sigma_y^2(\varepsilon_{eq}^p) \tag{2.4.24}$$

Using tensor operations, it can be shown that,

$$\boldsymbol{\sigma} : \boldsymbol{J} : \boldsymbol{\sigma} = 3\sigma_m^2 \quad \text{and} \quad \boldsymbol{\sigma} : \boldsymbol{K} : \boldsymbol{\sigma} = \frac{2}{3}\sigma_{eq}^2 \tag{2.4.25}$$

The yield function reduces to,

$$\Phi(\boldsymbol{\sigma}, \boldsymbol{s}) = \left(1 + \frac{2}{3}f\right)\left(\frac{\sigma_{eq}}{1-f}\right)^2 + \frac{9}{4}f\left(\frac{\sigma_m}{1-f}\right)^2 - \sigma_y^2(\varepsilon_{eq}^p) \tag{2.4.26}$$

2.4.3 Evolution of Internal Variables

With deformation of the material, the internal variables evolve and alter the macroscopic behaviour of the material i.e., the microstructure evolution are coupled to the constitutive relations. Here, the internal variables are assumed to evolve only under plastic deformation. This approximation is justified, because the elastic deformation in porous metals are to small. The evolution equations are determined from the kinematic relations. It is also assumed that the evolution of the internal variables are characterized by the corresponding average of plastic deformation rate and spin in the voids. The averages are obtained from the homogenization procedure discussed in the previous sections.

2.4.3.1 Evolution of equivalent plastic strain

Macroscopic plastic work in material is given by,

$$\boldsymbol{W} = \boldsymbol{\sigma} : \boldsymbol{D}^p = \dot{\Lambda}\boldsymbol{\sigma} : \boldsymbol{N} \tag{2.4.27}$$

Plastic work on the microscopic level depends on the rate of equivalent plastic strain,

$$\bar{\boldsymbol{W}} = (1-f)\sigma_y(\varepsilon_{eq}^p)\dot{\varepsilon}_{eq}^p \tag{2.4.28}$$

Due to equilibrium, the work done on the macroscopic level should be equal to the corresponding microscopic work. The evolution of equivalent plastic strain is obtained from this condition,

$$\dot{\varepsilon}_{eq}^p = \dot{\Lambda}\frac{\boldsymbol{\sigma} : \boldsymbol{N}}{(1-f)\sigma_y(\varepsilon_{eq}^p)} = \dot{\Lambda} g_1(\boldsymbol{\sigma}, \boldsymbol{s}) \tag{2.4.29}$$

where,

$$g_1(\boldsymbol{\sigma}, \boldsymbol{s}) = \frac{\boldsymbol{\sigma} : \boldsymbol{N}}{(1-f)\sigma_y(\varepsilon_{eq}^p)} \tag{2.4.30}$$

2.4.3.2 Evolution of void volume fraction

Evolution equation of void volume fraction can be derived from the continuity equation. For any material point $\boldsymbol{x}$ in continuum, balance of mass is given by [11],

$$\dot{\rho} + \rho \mathrm{div}(\dot{\boldsymbol{x}}) = 0 \tag{2.4.31}$$

Since the vacuous phase hs zero density, density of the heterogeneous material is equal to the density of the matrix. The effective density per unit volume of the heterogeneous material in terms of density of the matrix phase ρ_M,

$$\bar{\rho} = (1-f)\rho_M \tag{2.4.32}$$

Therefore,

$$\dot{\bar{\rho}} = -\dot{f}\rho_M + (1-f)\dot{\rho}_M \tag{2.4.33}$$

Since matrix material is incompressible in plastic region, the rate of change of density of the matrix would be zero ($\dot{\rho}_M = 0$). Hence,

$$\dot{\bar{\rho}} = -\dot{f}\rho_M \tag{2.4.34}$$

Also,

$$\mathrm{div}(\dot{\boldsymbol{x}}) = \nabla\dot{\boldsymbol{x}} \cdot \boldsymbol{I} = \boldsymbol{L} \cdot \boldsymbol{I} = \mathrm{trace}(\boldsymbol{L}) \tag{2.4.35}$$

But,

$$\begin{aligned} \mathrm{trace}(\boldsymbol{L}) &= \mathrm{tr}(\boldsymbol{D} + \boldsymbol{W}) \\ &= \mathrm{tr}(\boldsymbol{D}), \quad \text{since} \quad \mathrm{tr}(\boldsymbol{W}) = 0 \end{aligned} \tag{2.4.36}$$

Substituting in balance of mass, we obtain,

$$-\dot{f}\,\rho_M + (1-f)\,\rho_M\,\mathrm{tr}(\boldsymbol{D}) = 0$$

$$\dot{f} = (1-f)\mathrm{tr}(\boldsymbol{D})$$

Change of void volume fraction due to elastic deformation is assumed to be small and recoverable. Hence, $\dot{f}$ depends only on the plastic rate of deformation,

$$\begin{aligned} \dot{f} &= (1-f)\mathrm{tr}(\boldsymbol{D}^p) \\ &= (1-f)D^p_{kk} \\ &= \dot{\Lambda}(1-f)N_{kk} \\ &= \dot{\Lambda}g_2(\boldsymbol{\sigma}, \boldsymbol{s}) \end{aligned} \tag{2.4.38}$$

Where,

$$g_2(\boldsymbol{\sigma}, \boldsymbol{s}) = (1-f)N_{kk} \tag{2.4.39}$$

The initial VAR model does not account for void nucleation. In this study, strain controlled void nucleation was coupled with the constitutive equation. The void evolution due to void growth is given by

$$\dot{f}_g = \dot{\Lambda}g_2(\boldsymbol{\sigma}, \boldsymbol{s}) \tag{2.4.40}$$

And the strain controlled nucleation as described in Section 2.1 is given by

$$\dot{f}_n = A\dot{\varepsilon}^p_{eq}, \quad A = \frac{f_N}{S_N\sqrt{2\pi}}\exp\left[-\frac{1}{2}\left(\frac{\varepsilon^p_{eq} - \varepsilon_N}{S_N}\right)^2\right] \tag{2.4.41}$$

The evolution of porosity is then

$$\dot{f} = \dot{f}_g + \dot{f}_n \tag{2.4.42}$$

2.4.3.3 Evolution of local aspect ratios

To determine the evolution equations of aspect ratios, it is important to recall the computation of average deformation rate in phase r of a heterogeneous material introduced in Section 2.3.4.3. Accordingly, the average deformation rate in the local ellipsoidal void $\boldsymbol{D}^v$ is given by,

$$\boldsymbol{D}^v = \boldsymbol{A} : \boldsymbol{D}^p \tag{2.4.43}$$

Where the concentration tensor $\boldsymbol{A}$ is evaluated at $\nu = 1/2$.

$$\boldsymbol{A} = \left[\mathbb{I} - (1-f)\boldsymbol{S}|_{\nu=1/2}\right] \tag{2.4.44}$$

Applying product rule to aspect ratio w_1,

$$\begin{aligned} \dot{w}_1 &= \left(\frac{c}{a}\right)' \\ &= \frac{\dot{c}}{a} - \frac{c}{a^2}\dot{a} \\ &= \frac{c}{a}\left(\frac{\dot{c}}{c} - \frac{\dot{a}}{a}\right) \\ &= w_1\left(\frac{\dot{c}}{c} - \frac{\dot{a}}{a}\right) \end{aligned} \tag{2.4.45}$$

$\dot{c}$ is nothing but the plastic rate-of-deformation in the void along principal axis $\boldsymbol{n}^{(3)}$. Hence, the above equation can be reformulated in terms of rate of deformation of voids [4],

$$\begin{aligned} \dot{w}_1 &= w_1\left(\boldsymbol{n}^{(3)} \cdot \boldsymbol{D}^v \cdot \boldsymbol{n}^{(3)} - \boldsymbol{n}^{(1)} \cdot \boldsymbol{D}^v \cdot \boldsymbol{n}^{(1)}\right) \\ &= w_1(\boldsymbol{n}^{(3)}\boldsymbol{n}^{(3)} - \boldsymbol{n}^{(1)}\boldsymbol{n}^{(1)}) : \boldsymbol{D}^v \end{aligned} \tag{2.4.46}$$

Substituting Eq.2.4.43 we get,

$$\dot{w}_1 = \dot{\Lambda} w_1(\boldsymbol{n}^{(3)}\boldsymbol{n}^{(3)} - \boldsymbol{n}^{(1)}\boldsymbol{n}^{(1)}) : \boldsymbol{A} : \boldsymbol{N} = \dot{\Lambda} g_3(\boldsymbol{\sigma}, \boldsymbol{s}) \tag{2.4.47}$$

where,

$$g_3(\boldsymbol{\sigma}, \boldsymbol{s}) = w_1(\boldsymbol{n}^{(3)}\boldsymbol{n}^{(3)} - \boldsymbol{n}^{(1)}\boldsymbol{n}^{(1)}) : \boldsymbol{A} : \boldsymbol{N} \tag{2.4.48}$$

Similarly, the evolution equation for w_2 is determined to be,

$$\dot{w}_2 = \dot{\Lambda} w_2(\boldsymbol{n}^{(3)}\boldsymbol{n}^{(3)} - \boldsymbol{n}^{(2)}\boldsymbol{n}^{(2)}) : \boldsymbol{A} : \boldsymbol{N} = \dot{\Lambda} g_4(\boldsymbol{\sigma}, \boldsymbol{s}) \tag{2.4.49}$$

where,

$$g_4(\boldsymbol{\sigma}, \boldsymbol{s}) = w_2(\boldsymbol{n}^{(3)}\boldsymbol{n}^{(3)} - \boldsymbol{n}^{(2)}\boldsymbol{n}^{(2)}) : \boldsymbol{A} : \boldsymbol{N} \tag{2.4.50}$$

2.4.3.4 Evolution of Orientation Vectors

The average spin in the local ellipsoidal void $\boldsymbol{W}^v$ is given by Eq.2.3.92.

$$\boldsymbol{W}^v = \boldsymbol{W} - \boldsymbol{\mathcal{C}} : \boldsymbol{D}^p \tag{2.4.51}$$

where, $\boldsymbol{W}$ is the spin of the continuum and $\boldsymbol{\mathcal{C}}$ is the spin concentration tensor as introduced previously.

$$\boldsymbol{\mathcal{C}} = -(1-f)\boldsymbol{\Pi} : \boldsymbol{A} \tag{2.4.52}$$

$\boldsymbol{\Pi}$ is the Eshelby rotation tensor which depends on aspect ratios and orientation vectors.
The evolution of unit vectors of the ellipsoid along the principal axes is given by,

$$\dot{\boldsymbol{n}}^{(i)} = \boldsymbol{\omega} \cdot \boldsymbol{n}^{(i)} \tag{2.4.53}$$

$\boldsymbol{\omega}$ is an antisymmetric tensor which represents the spin of Eulerian axes of average deformation of the void. The change of void orientation which is corotational to the spin of the voids is given by,

$$\overset{\circ}{\boldsymbol{n}}^{(i)} = 0 \tag{2.4.54}$$

For a coordinate frame coincident with the local principal axes of the voids, $\boldsymbol{\omega}$ is given by [4],

$$\omega_{ij}^{'} = W_{ij}^{v'} + \frac{w_i^2 + w_j^2}{w_i^2 - w_j^2} D_{ij}^{v'}, \quad i \neq j, \quad w_i \neq w_j \tag{2.4.55}$$

With respect to a fixed Cartesian coordinate system (global coordinate system), $\boldsymbol{\omega}$ is given by,

$$\begin{aligned} \boldsymbol{\omega} = \boldsymbol{W}^v + \frac{1}{2} \sum_{i,j=1}^{3} \frac{w_i^2 + w_j^2}{w_i^2 - w_j^2} \left[(\boldsymbol{n}^{(i)}\boldsymbol{n}^{(j)} + \boldsymbol{n}^{(j)}\boldsymbol{n}^{(i)}) : \boldsymbol{D}^v \right] \boldsymbol{n}^{(i)}\boldsymbol{n}^{(j)}, \\ i \neq j, \quad w_i \neq w_j, \quad w_3 = 1 \end{aligned} \tag{2.4.56}$$

Substituting for void rate of deformation $\boldsymbol{D}^v$ (Eq.2.4.43) and void spin $\boldsymbol{W}^v$ (Eq.2.4.51), the above equation reduces to,

$$\begin{aligned} \boldsymbol{\omega} &= \boldsymbol{W} - \dot{\Lambda} \left[\boldsymbol{\mathcal{C}} : \boldsymbol{N} - \frac{1}{2} \sum_{i,j=1}^{3} \frac{w_i^2 + w_j^2}{w_i^2 - w_j^2} \left[(\boldsymbol{n}^{(i)}\boldsymbol{n}^{(j)} + \boldsymbol{n}^{(j)}\boldsymbol{n}^{(i)}) : \boldsymbol{A} : \boldsymbol{N} \right] \boldsymbol{n}^{(i)}\boldsymbol{n}^{(j)} \right], \\ &\qquad i \neq j, \quad w_i \neq w_j, \quad w_3 = 1 \\ &= \boldsymbol{W} - \boldsymbol{W}^p \end{aligned} \tag{2.4.57}$$

where $\boldsymbol{W}_p$ is know as the plastic spin of the continuum relative to the microstructure,

$$\boldsymbol{W}_p = \dot{\Lambda} \boldsymbol{\Omega}^p \tag{2.4.58a}$$

$$\begin{aligned} \boldsymbol{\Omega}^p = \boldsymbol{\mathcal{C}} : \boldsymbol{N} - \frac{1}{2} \sum_{i,j=1}^{3} \frac{w_i^2 + w_j^2}{w_i^2 - w_j^2} \left[(\boldsymbol{n}^{(i)}\boldsymbol{n}^{(j)} + \boldsymbol{n}^{(j)}\boldsymbol{n}^{(i)}) : \boldsymbol{A} : \boldsymbol{N} \right] \boldsymbol{n}^{(i)}\boldsymbol{n}^{(j)}, \\ i \neq j, \quad w_i \neq w_j, \quad w_3 = 1 \end{aligned} \tag{2.4.58b}$$

For a coordinate system which is aligned along the principal axes of the void, the components of $\boldsymbol{\Omega}^p$ are given by,

$$\Omega_{ij}^{p'} = \left(\mathcal{C}'_{ijkl} - \frac{w_i^2 + w_j^2}{w_i^2 - w_j^2} A'_{ijkl} \right) N'_{kl}, \qquad i \neq j,\ w_i \neq w_j,\ w_3 = 1, \text{ (no sum over i \& j)} \tag{2.4.59}$$

When any two aspect ratios are equal (for example $w_1 = w_2$ or $w_1 = w_3$), the material becomes locally transversely isotropic along the third direction, and $\boldsymbol{W}_p$ becomes indeterminate. Under such conditions the corresponding component of $\boldsymbol{W}_p$ can be set to zero without loss of accuracy [4]. For special case when the voids are spherical, $\boldsymbol{\Pi} = 0$, $\boldsymbol{\mathcal{C}} = 0$ and $\boldsymbol{W}_p = 0$. In these cases the material is locally isotropic. During implementation in FE-program, it is important to take care of such special conditions to avoid numerical oscillations and convergence issues.

2.4.3.5 Computation of Plastic Multiplier

The plastic multiplier is obtained from the consistency condition of the yield function. The consistency condition states that the time derivative of yield function should be stationary.

$$\dot{\Phi}(\boldsymbol{\sigma}, \boldsymbol{s}) = 0 \tag{2.4.60}$$

$$\dot{\Phi} = \frac{\partial \Phi}{\partial \boldsymbol{\sigma}} : \dot{\boldsymbol{\sigma}} + \frac{\partial \Phi}{\partial \varepsilon_{eq}^p} \dot{\varepsilon}_{eq}^p + \frac{\partial \Phi}{\partial f} \dot{f} + \sum_{n=1}^{2} \frac{\partial \Phi}{\partial w_n} \dot{w}_n + \sum_{p=1}^{3} \frac{\partial \Phi}{\partial \boldsymbol{n}^{(p)}} \dot{\boldsymbol{n}}^{(p)} \tag{2.4.61}$$

Since the yield function is isotropic, the consistency condition can be written in terms of corotational derivatives as,

$$\dot{\Phi} = \frac{\partial \Phi}{\partial \boldsymbol{\sigma}} : \overset{\circ}{\boldsymbol{\sigma}} + \frac{\partial \Phi}{\partial \varepsilon_{eq}^p} \dot{\varepsilon}_{eq}^p + \frac{\partial \Phi}{\partial f} \dot{f} + \sum_{n=1}^{2} \frac{\partial \Phi}{\partial w_n} \dot{w}_n + \sum_{p=1}^{3} \frac{\partial \Phi}{\partial \boldsymbol{n}^{(p)}} \overset{\circ}{\boldsymbol{n}}^{(p)} \tag{2.4.62}$$

Substituting Eq.2.4.54 we obtain,

$$\begin{aligned} \dot{\Phi} &= \frac{\partial \Phi}{\partial \boldsymbol{\sigma}} : \overset{\circ}{\boldsymbol{\sigma}} + \frac{\partial \Phi}{\partial \varepsilon_{eq}^p} \dot{\varepsilon}_{eq}^p + \frac{\partial \Phi}{\partial f} \dot{f} + \sum_{n=1}^{2} \frac{\partial \Phi}{\partial w_n} \dot{w}_n \\ &= \boldsymbol{N} : \overset{\circ}{\boldsymbol{\sigma}} + \frac{\partial \Phi}{\partial \varepsilon_{eq}^p} \dot{\Lambda} g_1 + \frac{\partial \Phi}{\partial f} \dot{\Lambda} g_2 + \frac{\partial \Phi}{\partial w_1} \dot{\Lambda} g_3 + \frac{\partial \Phi}{\partial w_2} \dot{\Lambda} g_4 \\ &= \boldsymbol{N} : \overset{\circ}{\boldsymbol{\sigma}} - \dot{\Lambda} H \end{aligned} \tag{2.4.63}$$

where H is defined as the hardening modulus given by,

$$H = -\left(\frac{\partial \Phi}{\partial \varepsilon_{eq}^p} g_1 + \frac{\partial \Phi}{\partial f} g_2 + \frac{\partial \Phi}{\partial w_1} g_3 + \frac{\partial \Phi}{\partial w_2} g_4 \right) \tag{2.4.64}$$

When $H > 0$, the material is said to instantaneously harden, the yield surface expands. When $H < 0$, the material softens, the yield surface shrinks. When $H = 0$,

the material exhibits instantaneous perfect-plastic behaviour. Finally, the plastic multiplier is given by,

$$\dot{\Lambda} = \frac{1}{H}\boldsymbol{N} : \overset{\circ}{\boldsymbol{\sigma}} \qquad \text{for } H \neq 0 \tag{2.4.65}$$

We know that the effective yield function is given by,

$$\begin{aligned}\Phi(\boldsymbol{\sigma}, \boldsymbol{s}) &= \frac{1}{1-f}\boldsymbol{\sigma} : \boldsymbol{m} : \boldsymbol{\sigma} - \sigma_y^2(\varepsilon_{eq}^p) \\ &= \frac{1}{1-f}\boldsymbol{\sigma} : \left(\frac{3}{2}\boldsymbol{K} + \frac{3f}{1-f}\mu\boldsymbol{Q}^{-1}|_{\nu=1/2}\right) : \boldsymbol{\sigma} - \sigma_y^2(\varepsilon_{eq}^p)\end{aligned} \tag{2.4.66}$$

Taking the derivative of yield function with respect to void volume fraction f using product rule, and by simplifying the equation further, we obtain,

$$\frac{\partial \Phi}{\partial f} = \frac{3}{(1-f)^2}\boldsymbol{\sigma} : \left(\frac{1}{2}\boldsymbol{K} + \frac{1+f}{1-f}\mu\boldsymbol{Q}^{-1}|_{\nu=1/2}\right) : \boldsymbol{\sigma} \tag{2.4.67}$$

The derivatives of yield function with respect to aspect ratios are discussed in detail by Aravas and Ponte Castañeda [4].

2.4.3.6 Rate form of the elastoplastic equations

From the elastic constitutive relation we have,

$$\boldsymbol{D}^e = \boldsymbol{M}^e : \overset{\circ}{\boldsymbol{\sigma}} \Rightarrow \overset{\circ}{\boldsymbol{\sigma}} = \boldsymbol{C}^e : \boldsymbol{D}^e \tag{2.4.68}$$

But, the elastic rate-of-deformation is given by,

$$\boldsymbol{D}^e = \boldsymbol{D} - \boldsymbol{D}^p = \boldsymbol{D} - \dot{\Lambda}\boldsymbol{N} \tag{2.4.69}$$

Hence,

$$\begin{aligned}\overset{\circ}{\boldsymbol{\sigma}} &= \boldsymbol{C}^e : \boldsymbol{D} - \dot{\Lambda}\boldsymbol{C}^e : \boldsymbol{N} \\ &= \boldsymbol{C}^e : \boldsymbol{D} - \frac{1}{H}\boldsymbol{N} : \overset{\circ}{\boldsymbol{\sigma}}\boldsymbol{C}^e : \boldsymbol{N} \\ &= \boldsymbol{C}^e : \boldsymbol{D} - \frac{1}{L}\left(\boldsymbol{N} : \boldsymbol{C}^e : \boldsymbol{D}\right)\boldsymbol{C}^e : \boldsymbol{N} \\ &= \left(\boldsymbol{C}^e - \frac{1}{L}\boldsymbol{C}^e : \boldsymbol{N}\boldsymbol{N} : \boldsymbol{C}^e\right) : \boldsymbol{D}\end{aligned} \tag{2.4.70}$$

where,

$$L = H + \boldsymbol{N} : \boldsymbol{C}^e : \boldsymbol{N} \tag{2.4.71}$$

2.5 A note on numerical issues and extension of ABAQUS VUMAT Subroutine

2.5.1 Numerical Issues

The VAR constitutive model was implemented in ABAQUS-Explicit through VUMAT subroutine at Fraunhofer IWM, Freiburg. However, this subroutine was not qualified for metals undergoing large deformations, as in the case of metal forming applications. In this section, the numerical issues encountered during this specific application is discussed.

2.5.1.1 Element Closure

When metals with low initial porosity were subjected to extreme compression loads, i.e. when the ratio of final height of the specimen to its initial height was less than 0.5, the elements distorted abnormally, and collapsed. This phenomenon is know as Element closure in this context. Fig.(2.5.1) describes the phenomenon of element closure in an axisymmetric upsetting test simulation. For this simulation, axisymmetric continuum stress/displacement, 4-node, reduced-integration CAX4R element is used.

It was further observed in other types of Axisymmetric and 3D reduced and full

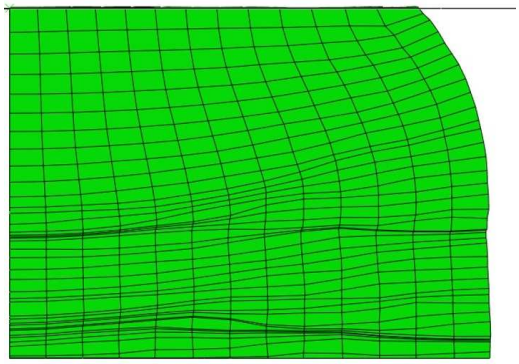

Fig. 2.5.1: Element closure phenomenon

integration elements. Use of full integration element rules out the possibility of hour glass effect [64], which rules out hour glass effect as the possible cause. It was determined that this phenomenon was due to improper evaluation of Eshelby tensors. Here, the Eshelby tensors in the void frame are obtained by evaluating the integral equations [4] in Mathematica software package, for a certain range and distribution of aspect ratios. This data set is made available to the subroutine. For unevaluated aspect ratios within the range, the Eshelby tensors are obtained by linear interpolation within the subroutine.

$$\boldsymbol{S} = \frac{1}{4\pi w_1 w_2} \int_{|\xi|=1} \boldsymbol{H}(\boldsymbol{\xi}) : \boldsymbol{C} \frac{dS(\boldsymbol{\xi})}{|\boldsymbol{Z}^{-1} \cdot \boldsymbol{\xi}|^3} \tag{2.5.1}$$

where

$$(\boldsymbol{H}(\xi):\boldsymbol{C})_{ijkl}(\xi,\nu)=\frac{1}{2|\xi|^2}(\delta_{ik}\xi_j\xi_l+\delta_{jk}\xi_i\xi_l+\delta_{il}\xi_j\xi_k+\delta_{jl}\xi_i\xi_k) \\ -\frac{1}{|\xi|^4}\frac{1}{1-\nu}\xi_i\xi_j\xi_k\xi_l+\frac{1}{|\xi|^2}\frac{\nu}{1-\nu}\xi_i\xi_j\delta_{kl} \tag{2.5.2a}$$

$$\boldsymbol{Z}=w_1\boldsymbol{n}^{(1)}\boldsymbol{n}^{(1)}+w_2\boldsymbol{n}^{(2)}\boldsymbol{n}^{(2)}+\boldsymbol{n}^{(3)}\boldsymbol{n}^{(3)} \tag{2.5.2b}$$

Eshelby tensor $\boldsymbol{\Pi}$ is given by

$$\boldsymbol{\Pi}=\frac{1}{4\pi w_1 w_2}\int_{|\xi=1|}\hat{\boldsymbol{H}}(\boldsymbol{\xi}):\boldsymbol{C}\frac{dS(\boldsymbol{\xi})}{|\boldsymbol{Z}^{-1}\cdot\boldsymbol{\xi}|^3} \tag{2.5.3}$$

where

$$(\hat{\boldsymbol{H}}(\boldsymbol{\xi}):\boldsymbol{C})_{ijkl}(\boldsymbol{\xi})=\frac{1}{2|\xi|^2}(\delta_{ik}\xi_j\xi_l-\delta_{jk}\xi_i\xi_l+\delta_{il}\xi_j\xi_k-\delta_{jl}\xi_i\xi_k) \tag{2.5.4}$$

And the Eshelby tensor $\boldsymbol{Q}$ is written in the form

$$\frac{1}{\mu}\boldsymbol{Q}=\frac{1}{4\pi w_1 w_2}\int_{|\xi|=1}\boldsymbol{E}(\boldsymbol{\xi})\frac{dS(\boldsymbol{\xi})}{|\boldsymbol{Z}^{-1}\cdot\boldsymbol{\xi}|^3} \tag{2.5.5}$$

where

$$E_{ijkl}(\boldsymbol{\xi},\nu)=\delta_{ik}\delta_{jl}+\delta_{il}\delta_{jk}-\frac{1}{|xi|^2}(\delta_{ik}\xi_j\xi_l+\delta_{jk}\xi_i\xi_l+\delta_{il}\xi_j\xi_k+\delta_{jl}\xi_i\xi_k) \\ -\frac{2\nu}{1-\nu}\left[\delta_{ij}\delta_{kl}-\frac{1}{|\xi|^2}(\delta_{ij}\xi_k\xi_l+\delta_{kl}\xi_i\xi_j)\right]+\frac{2}{|\xi|^4}\frac{1}{1-\nu}\xi_i\xi_j\xi_k\xi_l \tag{2.5.6}$$

Under large strains, the aspect ratios of the voids were observed to exceed the ranges used to calculate the Eshelby tensors, which lead to numerical difficulties. To troubleshoot this issue, the voids are assumed to be closed if the aspect ratios are greater than 10^2 or less than 10^{-2}. Once the aspect ratios attain these limits, the subroutine skips the calculation of Eshelby tensors and the evolution of void aspect ratios are set to zero ($g_3 = g_4 = 0$). Also, a lower limit of 10^{-4} is set for void volume fraction (f), as suggested by Kailasam and Ponte Castañeda [42]. Fig.(2.5.2) shows that the element closure phenomenon is resolved.

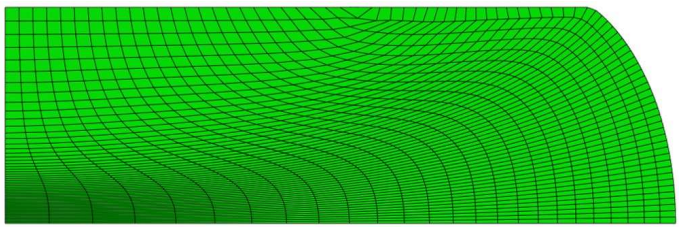

Fig. 2.5.2: Upsetting test simulation which depicts the resolved element closure phenomenon

2.5.1.2 Convergence issue of Cutting Plane algorithm

As stated previously, the subroutine uses cutting plane algorithm to solve the local problem of plasticity. Since the time step width in explicit simulations are small (of order 10^{-7}), the number of cutting plane iterations required for convergence should be in the range of 3-5. In the subroutine, the maximum number of possible cutting plane iterations for each time step is provided as an input variable. Once this limit is reached, the numerical calculation exits the cutting plane loop and the converged results from the previous time step are assumed to be the solution for the current time step as well. This approximation is justified as the time step width is small, and doesn't lead to abrupt changes in results. In the following simulations, a maximum limit of 20 iterations are set for the cutting plane algorithm.

Irrespective of type of loading (Tension or Compression), it was observed that the cutting plane algorithm failed to converge when the aspect ratios were equal to 1 i.e. when w_1 or $w_2 = 1$ and the results obtained were not plausible. Fig.(2.5.3) and Fig.(2.5.4) describe the numerical results of Upsetting and Uniaxial Tensile test respectively. It can be observed that the material points where the aspect ratios are close to 1, require more iterations in cutting plane loop, and eventually leads to divergence of the solution.

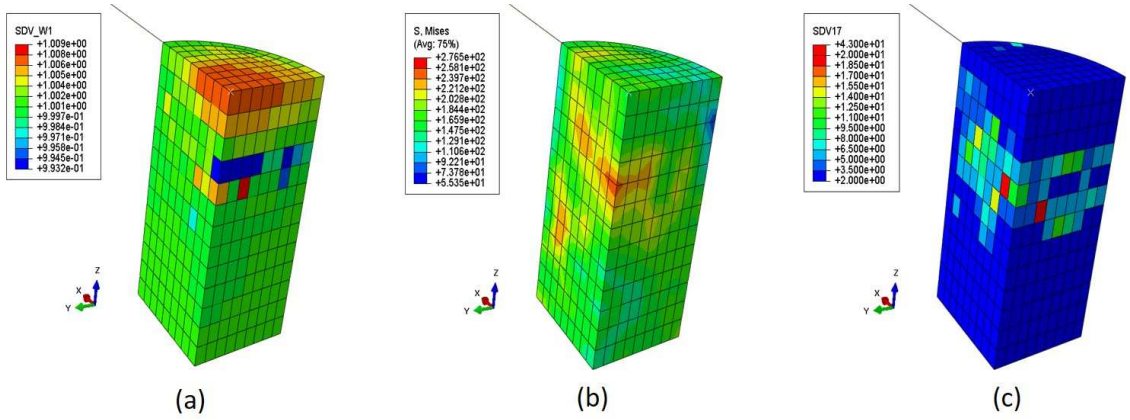

Fig. 2.5.3: Simulation results of upsetting test, which describes the numerical oscillations due to non convergence of cutting plane algorithm. a)Aspect ratio w_1 b)Field output of von mises stress distribution in elements c) Number of cutting plane iterations required at each material point

This issue is linked to the calculation of the plastic spin $\boldsymbol{W}^p$ given by Eq.2.4.58a. In the calculation of $\boldsymbol{\Omega}^p$, the imaginary third aspect ratio (w_3) is taken as 1.

$$\boldsymbol{\Omega}^p = \boldsymbol{\mathcal{C}} : \boldsymbol{N} - \frac{1}{2}\sum_{i,j=1}^{3} \frac{w_i^2 + w_j^2}{w_i^2 - w_j^2} \left[(\boldsymbol{n}^{(i)}\boldsymbol{n}^{(j)} + \boldsymbol{n}^{(j)}\boldsymbol{n}^{(i)}) : \boldsymbol{A} : \boldsymbol{N} \right] \boldsymbol{n}^{(i)}\boldsymbol{n}^{(j)}, \qquad (2.5.7)$$
$$i \neq j, \quad w_i \neq w_j, \quad w_3 = 1$$

At any point during the calculation, when the aspect ratios are equal to each other ($w_1 = 1$ or $w_2 = 1$ or $w_1 = w_2$), the denominator in the second term is equal

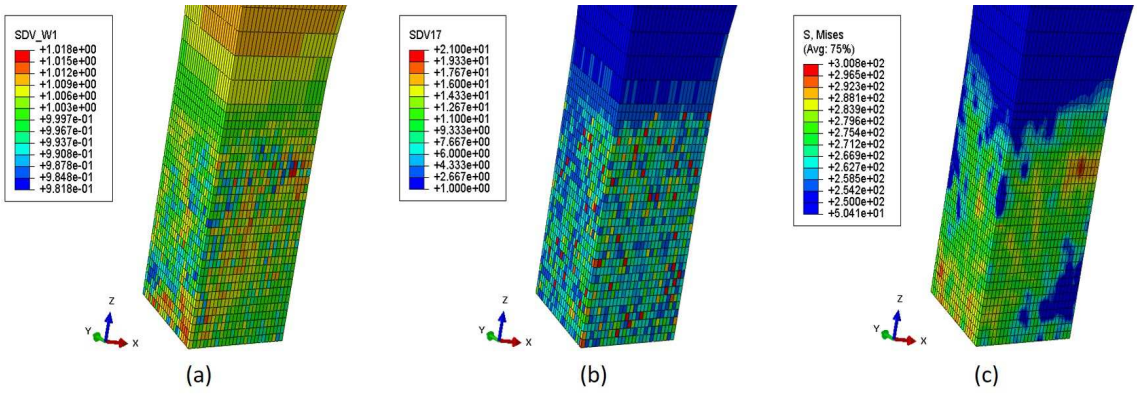

Fig. 2.5.4: Simulation results of uniaxial tensile test, which describes the numerical oscillations due to non convergence of cutting plane algorithm. a) Aspect ratio $w1$ b) Number of cutting plane iterations required at each material point c) Field output of von mises stress distribution in elements

to zero, which results in indeterminate $\boldsymbol{W}_p$. To overcome this numerical issue, the plastic spin tensor W_p and the corresponding terms of $\mathcal{C}_{ijkl}$ are set to zero when the difference between the aspect ratios are less than 10^{-2}.

$$\boldsymbol{W}^p = 0 \quad \text{and} \quad \mathcal{C}_{ijkl} = 0 \quad \text{when} \quad w_i - w_j \leq 10^{-2},\ i \neq j \tag{2.5.8}$$

Also, for the case where the voids are spherical, the yield surface is taken to be the equation derived in Section 2.4.2 [4].

$$\Phi(\boldsymbol{\sigma}, \boldsymbol{s}) = \left(1 + \frac{2}{3}f\right)\left(\frac{\sigma_{eq}}{1-f}\right)^2 + \frac{9}{4}f\left(\frac{\sigma_m}{1-f}\right)^2 - \sigma_y^2(\varepsilon_{eq}^p) \quad \text{when} \quad w_i - 1.0 \leq 10^{-2}, \quad i = 1, 2 \tag{2.5.9}$$

2.5.1.3 Example from literature

To measure the accuracy of the subroutine with changes, a plane strain extrusion process described in Kailasam and Ponte Castañeda [42] is simulated. The parametric dimension of the extruded part is described in Fig.(2.5.5).

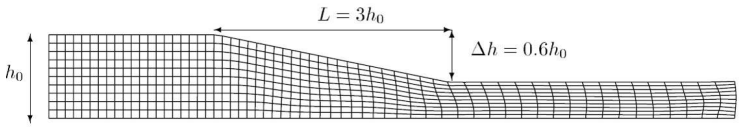

Fig. 2.5.5: Dimension of Extruded part

A material with initial porosity of $f = 0.15$ with spherical voids is used for this simulation. The matrix material is considered to be elastic - perfect plastic with a Young's modulus of $E = 300\sigma_y$ and Poisson's ratio $\nu = 0.49$. The specimen is considered to be symmetric about the axes. The effect of fristion between the metal and die interface is neglected. The material deforms in $\boldsymbol{n}^{(2)}$ - $\boldsymbol{n}^{(3)}$ plane. Fig.(2.5.6) gives a comparison of void volume fraction between the old version of subroutine,

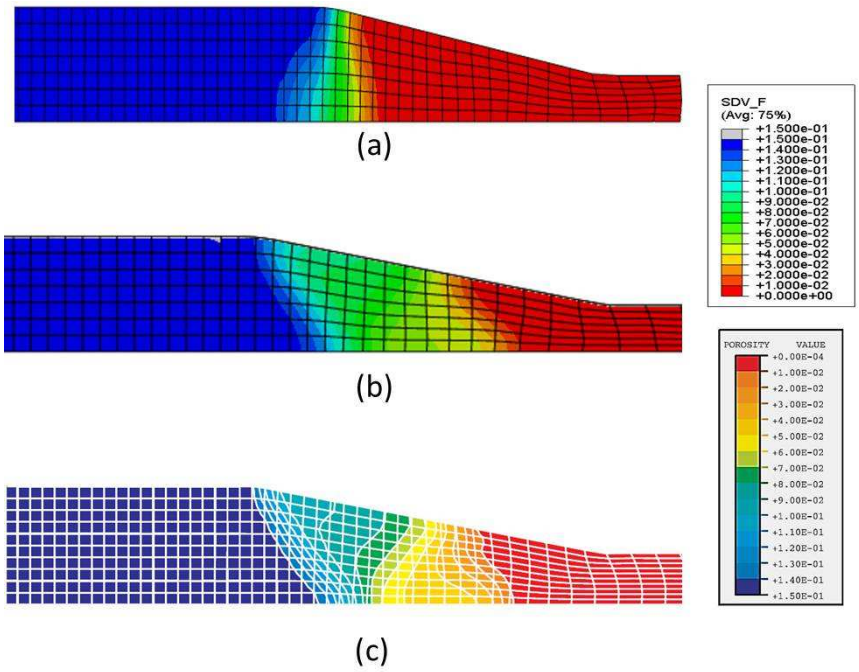

Fig. 2.5.6: Void volume fraction a)Old version of subroutine b) revised version of subroutine c) literature [42]

the revised version and the results from literature.

The variation of porosity along the bottom row of elements along the extruded specimen is shown in Fig.(2.5.7). This plot is closely in agreement with the results from literature. The void volume fraction predicted by VAR model is lower than the Gurson model. The VAR model predicts that the voids close even before exiting the die. The distribution of aspect ratio in the extruded part is given in Fig.(2.5.8). It is observed that the aspect ratios of the voids are very small after extrusion and the longest axis of the void is aligned in the direction of extrusion. It can been seen that the results obtained from the revised version of subroutine agree closely to the literature results.

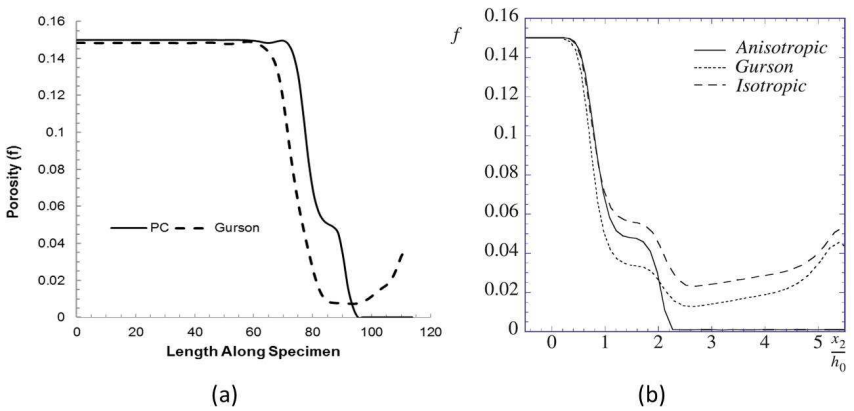

Fig. 2.5.7: Variation of void volume fraction along the bottom row of elements a) VUMAT subroutine b) Literature

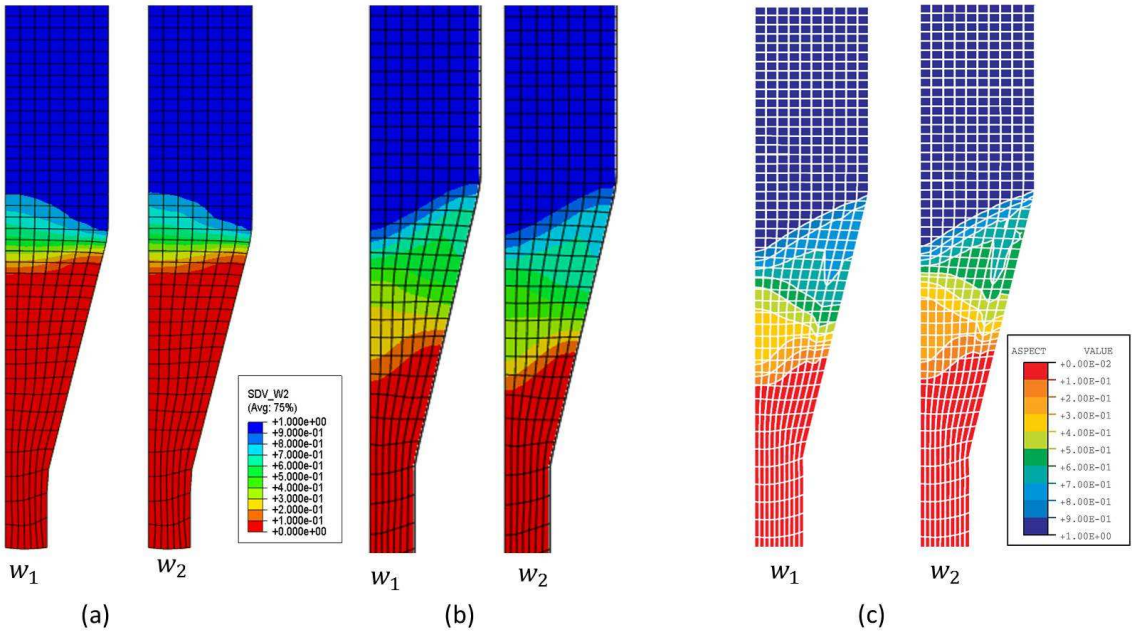

Fig. 2.5.8: Aspect ratios a) Older version of subroutine b)revised version of subroutine c) literature [42]

2.5.2 Extension of VUMAT Subroutine

2.5.2.1 Hardening laws

For any simulation involving plasticity, it is important to provide the behaviour of the material in plastic region to the FE program i.e. the right constitutive equation which describes the plastic behaviour of the material must be used. The constitutive equations can be broadly classified into power laws(Ludwick's law and Swift law) and saturation laws(Voce, Hockett-Sherby). Power laws tend to over predict the stresses at high strains, on the contrary, saturation laws under predict the stresses.

To increase the scope of the subroutine, various isotropic hardening laws were

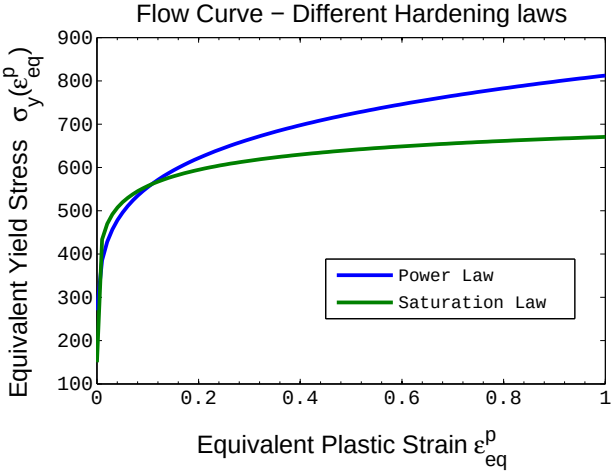

Fig. 2.5.9: Flow curves obtained from Power and Saturation hardening laws

implemented. In this study, only hardening laws which are independent of strain rate and temperature are considered. For the evolution of the internal variables, it is also important to provide the derivative of equivalent yield stress with respect to equivalent plastic strain. The following hardening laws were implemented.

a) Swift law

$$\sigma_y = A(\varepsilon_0 + \varepsilon^p_{eq})^n \tag{2.5.10}$$

$$\frac{\partial \sigma_y}{\partial \varepsilon^p_{eq}} = \frac{\sigma_y n}{\varepsilon_0 + \varepsilon^p_{eq}} \tag{2.5.11}$$

where A, ε_0 and n are material parameters.

b) Hockett and Sherby Law

$$\sigma_y = A - B\left[1 - \exp\left\{-C(\varepsilon^p_{eq})^n\right\}\right] \tag{2.5.12}$$

$$\frac{\partial \sigma_y}{\partial \varepsilon^p_{eq}} = B\left[1 - \exp\left\{-C(\varepsilon^p_{eq})^n\right\}\right]\left[C\, n\, (\varepsilon^p_{eq})^{(n-1)}\right] \tag{2.5.13}$$

where A, B, C and n are the material parameters.

c) Combination of Ghosh and Hockett-Sherby Law

$$\begin{aligned}\sigma_y = \alpha &\left[A - (A-B)\exp\left\{-C(\varepsilon^p_{eq})^n\right\}\right] \\ &+ (1-\alpha)\left[A_G(B_G + \varepsilon^p_{eq})^{n_G} - C_G\right]\end{aligned} \tag{2.5.14}$$

$$\begin{aligned}\frac{\partial \sigma_y}{\partial \varepsilon^p_{eq}} = \alpha &\left[(A-B)\exp\left\{-C(\varepsilon^p_{eq})^n\right\}\left(C\, n\, (\varepsilon^p_{eq})^{(n-1)}\right)\right] \\ &+ (1-\alpha)\left[A_G(B_G + \varepsilon^p_{eq})^{(n_G-1)} n_G\right]\end{aligned} \tag{2.5.15}$$

where α is the weighting factor

The material parameters in the hardening laws are obtained from experiments like uniaxial tensile test, upsetting test, etc.

2.5.2.2 Coalescence Criteria

Thomason based coalescence criteria as proposed by Pardoen and Hutchinson [56] and Benzerga [9] were implemented in the subroutine. As the coalescence criteria depends on aspect ratios, the critical value of the coalescence criteria were evaluated for aspect ratios w_1 and w_2, and equivalent aspect ratio w_{eq}. The critical value are mapped to State dependent variables (SDV) for ease of post-processing.

The Pardoen and Hutchinson based coalescence is given by,

$$C_t = \frac{\sigma^{Pr}_{max}/\sigma_y}{[1-\chi_i^2]\left[\alpha\left(\dfrac{1-\chi_i}{\chi_i w_i}\right)^2 + \beta\chi_i^{-1/2}\right]} \tag{2.5.16}$$

where

$$\chi_i = \left(\frac{3}{2} f \frac{\exp\left(\frac{3}{2}\varepsilon_{eq}^{p}\right)}{w_i} \right)^{1/3}, \quad \alpha = 0.1, \quad \beta = 1.2 \tag{2.5.17}$$

The Benzerga coalescence criteria is given by

$$C_b = \frac{\sigma_{max}^{Pr}/\sigma_y}{[1-\chi_i^2]\left[\alpha\left(\frac{\chi_i^{-1}-1}{w_i^2+0.1\chi_i^{-1}+0.02\chi_i^{-2}}\right)^2 + 1.3\chi_i^{-1/2}\right]} \tag{2.5.18}$$

Fig.(2.5.10) shows the distribution of critical values C_t and C_b in axisymmetric

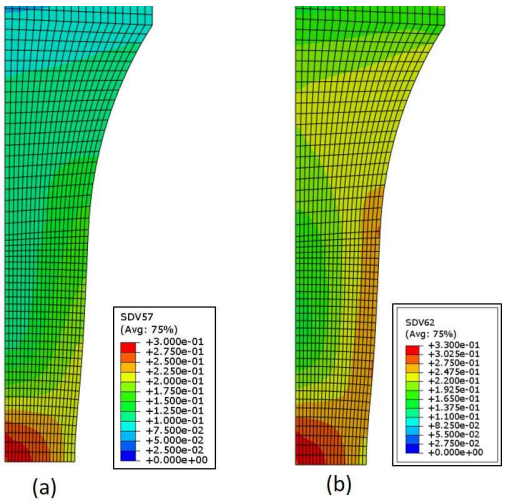

Fig. 2.5.10: Distribution of critical values of Thomason based void coalescence criteria in uniaxial tensile test (considering aspect ratio w_1 a) Pardoen and Hutchinson based formulation C_t b) Benzerga criteria C_b

uniaxial tensile test. It is to be noted that the critical values obtained from both the criterias are different and the field distribution is also different. However, the maximum values are predicted at the same location by both.

2.5.2.3 Modification of Void Nucleation

As we know, the strain controlled void nucleation is given by

$$\dot{f}_n = A\dot{\varepsilon}_{eq}^{p}, \quad A = \frac{f_N}{S_N\sqrt{2\pi}}\exp\left[-\frac{1}{2}\left(\frac{\varepsilon_{eq}^{p}-\varepsilon_N}{S_N}\right)^2\right] \tag{2.5.19}$$

The nucleation function depends on equivalent plastic strain and positive stress triaxiality. Usually the void nucleation parameters are identified from the uniaxial tensile test simulations where the stress triaxiality is always positive. In case of

pure compression loading (as in upsetting test), the stress triaxiality is negative initially. As the load increases, the triaxiality on the outer surface of the specimen increases purely due to friction in the tool. But, by the time stress triaxiality turns positive, the equivalent plastic strain is high. Due to high equivalent plastic strain, the amount of voids nucleated are less, as the nucleation function is towards the end of standard distribution curve. The shaded region in Fig.(2.5.11) describes the total number of voids nucleated. It is clear that the number of voids nucleated are few.

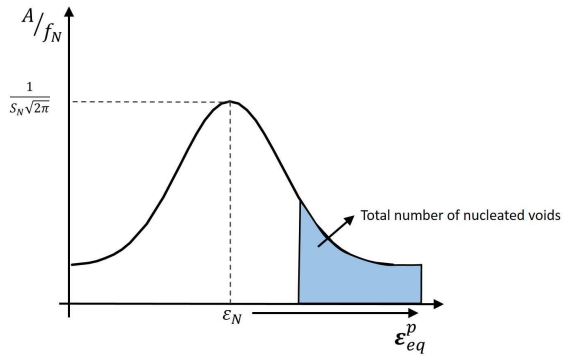

Fig. 2.5.11: Gauss distribution of void nucleation function. The figure shows that the number of voids nucleated are less when the equivalent plastic strain is high

To increase the number of nucleated voids, a new parameter called Nucleation equivalent plastic strain ε^p_{Neq} replaces the equivalent plastic strain in void nucleation function. ε^p_{Neq} starts accumulating only when stress triaxiality is positive. The increment of ε^p_{Neq} is zero when stress triaxiality is negative, and is equal to increment of equivalent plastic strain when stress triaxiality is positive.

$$\varepsilon^p_{Neq_{(n+1)}} = \varepsilon^p_{Neq_{(n)}} + \Delta\varepsilon^p_{Neq} \tag{2.5.20}$$

where

$$\Delta\varepsilon^p_{Neq} = \begin{cases} 0 & \text{when} \quad T \leq 0, \\ \Delta\varepsilon^p_{eq} & \text{when} \quad T > 0 \end{cases} \tag{2.5.21}$$

And the nucleation function is given by

$$\dot{f}_n = A\dot{\varepsilon}^p_{eq}, \quad A = \frac{f_N}{S_N\sqrt{2\pi}}\exp\left[-\frac{1}{2}\left(\frac{\varepsilon^p_{Neq} - \varepsilon_N}{S_N}\right)^2\right] \tag{2.5.22}$$

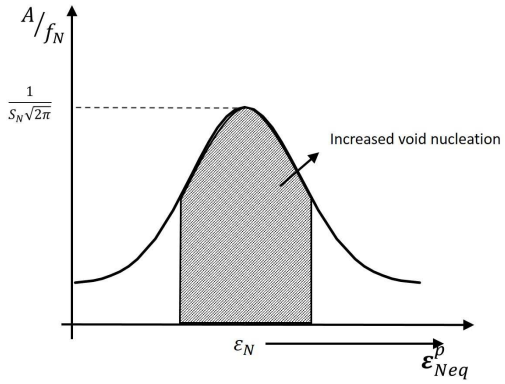

Fig. 2.5.12: Gauss distribution of void nucleation function with respect to Nucleation equivalent plastic strain. The figure shows that the number of voids nucleated are higher in comparison

Fig.(2.5.12) shows that the number of voids nucleated with this modification are higher. Fig.(2.5.13) depicts the improvement in void nucleation in a standard upsetting test. The new function predicts higher void volume fraction at right position.

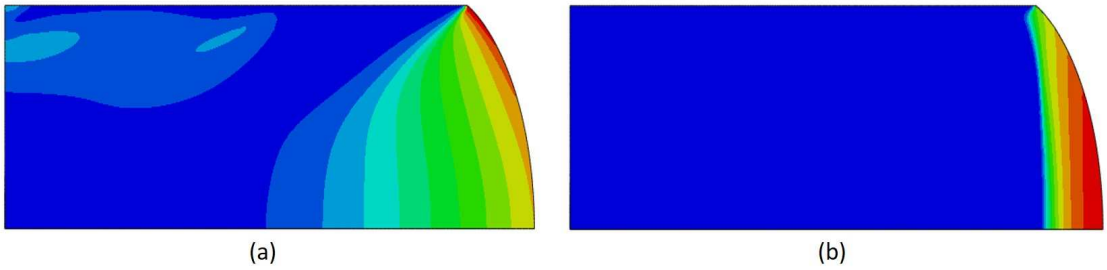

Fig. 2.5.13: Distribution of nucleated void volume fraction in upsetting test (a) with old nucleation function Eq.2.5.19 (b) New nucleation function Eq. 2.5.22

Chapter 3

Parameter identification and assessment of the material model

3.1 Identification of Hardening law parameters

The parameters of different hardening laws (implemented in the subroutine) are identified by fitting the curves to experimental flow curve. In this study, Steel 20MnCr5-GKZ is considered as this material is was studied at Fraunhofer IWM as a part of AIF Project - IGF 17678 N. This grade of steel is case hardened and used to manufacture gears, pinions, spindle, cams, etc. The material is subjected to GKZ(Gluehen nach Kugelformiger Zementit) soft annealing to obtain spherical cementite in the material structure, which makes it easier for machining and increases its resistance to wear. The chemical composition of the material is given in Table 3.1.1.

The following methodology is used to obtain the experimental flow curve.

Steel	C	Si	Mn	Cr	S	Others
20MnCr5	0.20	0.25	1.25	1.15	<0.035	(Pb)

Table 3.1.1: Chemical composition of 20MnCr5 Steel in % [28]

Steel	ρ (tonne/mm^3)	E (MPa)	ν	σ_y(MPa)
20MnCr5-GKZ	7.8×10^{-9}	200000	0.31	263.0

Table 3.1.2: Mechanical properties of 20MnCr5-GKZ Steel

1) True stress vs true strain data from uniaxial tensile test are used as a first approximation, until the region when the elongation is uniform (here uniaxial strain of 0.2).
The true stress and strain are calculated using the formula,

$$\boldsymbol{\sigma}_{true} = \boldsymbol{\sigma}_{eng}(1 + \varepsilon_{eng}), \quad \boldsymbol{\sigma}_{eng} = F/A_0, \quad \varepsilon_{eng} = \Delta l/l_0 \tag{3.1.1}$$

$$\varepsilon^{p}_{true} = \ln(1 + \varepsilon_{eng}) - \frac{\sigma_{true}}{E} \tag{3.1.2}$$

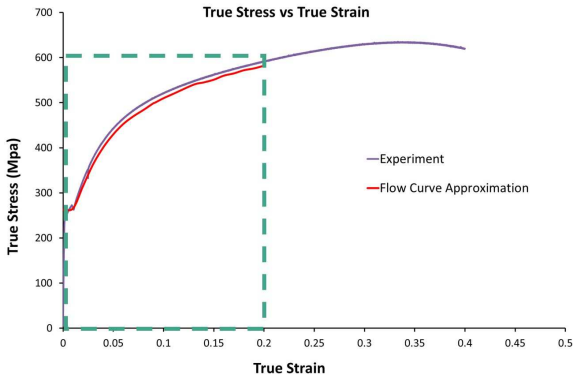

Fig. 3.1.1: First approximation of flow curve data from uniaxial tensile test

2) For strains between 0.2 and 1.5, the flow curve is adjusted to the experimental results of upsetting test by inverse simulation. In case of upsetting test, the force displacement curve is used, as it is difficult to measure the instantaneous cross section area of the specimen.

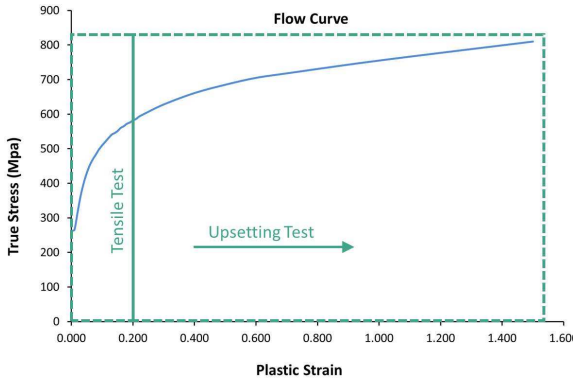

Fig. 3.1.2: Flow curve obtained from uniaxial tensile test and upsetting test results

3) The stress at higher values of strains for the flow curve were obtained by extrapolation of the experimental data using a logarithmic function. Here, the logarithmic function which was obtained by fitting the initial data is given by

$$\boldsymbol{\sigma}_{true} = 105 \ln(\varepsilon^{p}_{true}) + 760 \tag{3.1.3}$$

The tabulated experimental flow curve obtained using the above procedure was used to simulate tensile test, upsetting test and cylinder with notch test in ABAQUS, and it was observed that the numerical force displacement curve were in close agreement to the experimental force displacement curves.

The best fit for parameters in equations Eq.2.5.10, Eq.2.5.12 and Eq.2.5.14 were obtained using least square method. Apart from the three previously mentioned

hardening laws, the parameters for Ludwick law were also determined. Ludwick's hardening law is given by,

$$\sigma_y = A\left(1 + \frac{\varepsilon^p_{eq}}{A/E}\right)^{(1/x_N)} \tag{3.1.4}$$

Identified parameters are tabulated below.

A	x_N
263.0	6.486

Table 3.1.3: Parameters in Ludwick hardening law

A	ε_0	n
780.499	0.002	0.209

Table 3.1.4: Parameters in Swift hardening law

A	B	C	n
263	623.4	2.018	0.666

Table 3.1.5: Parameters in Hockett and Sherby hardening law

α	A	B	C	n	A_G	B_G	C_G	n_G
0.669	0.0	910.0	1.1	0.7163	9436.36	0.0221	0.0917	7708.509

Table 3.1.6: Parameters in Hockett and Sherby - Ghosh hardening law

From Fig.(3.1.3) it is clear that the best fit is given by the combination of Hockett-Sherby and Ghosh hardening laws. Hence, for further simulations Hockett-Sherby and Ghosh hardening law parameters will be used.

3.2 Micromechanical Parameter Identification

In case of VAR micromechanical model, the micromechanical parameters to be identified are

1. Initial Void Volume fraction - f_0
   The initial void volume fraction of the material is obtained by observing the specimen under SEM microscope at high resolution. It was observed that the initial void volume fraction of Steel-20MnCr5GKZ, was almost zero. For further simulations, f_0 is taken to be 1.5×10^{-4}

2. Void nucleation parameters

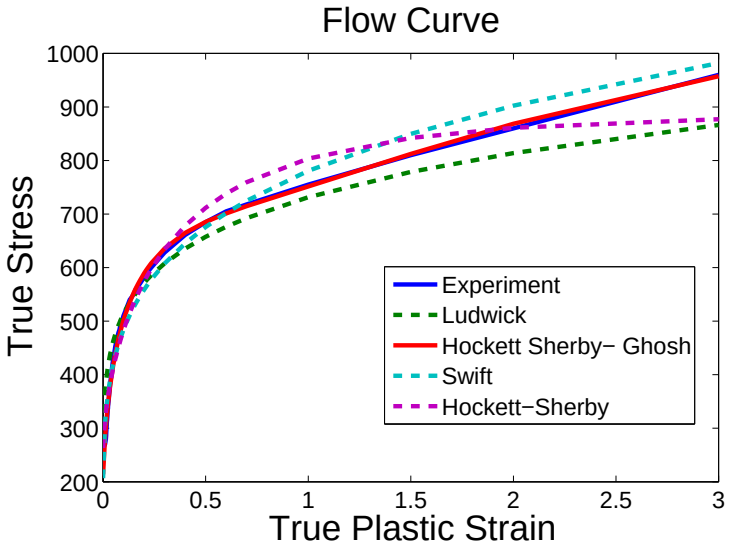

Fig. 3.1.3: Comparison of different flow curve approximations with the experimental flow curve

a) mean equivalent plastic strain for nucleation ε_N

b) standard deviation of distribution S_N

c) void volume fraction of nucleated voids f_N

These parameters are obtained by inverse simulation of uniaxial tensile test. The nominal stress-strain curve obtained from simulations are compared to the experimental nominal stress-strain curve to determine the parameters. Since 3 parameters are to be obtained from 1 curve, the system of equations is underdetermined. Hence multiple stationary solutions can be obtained i.e. the values of these parameters are not unique.

3. Void shape parameters

   a) Initial aspect ratio w_{10}

   b) Initial aspect ratio w_{20}

   For major part of the study, the voids are assumed to be initially spherical. i.e. $w_{10} = w_{20} = 1$

4. Void principal axes $\boldsymbol{n}^{(1)}$, $\boldsymbol{n}^{(2)}$ and $\boldsymbol{n}^{(3)}$ along the principal lengths of the void.

   i) For 3-dimensional simulations the voids are assumed to be oriented along the global Eulerian coordinate system.

$$\boldsymbol{n}_{(1)} = \boldsymbol{e}_1, \quad \boldsymbol{n}_{(2)} = \boldsymbol{e}_2, \quad \text{and} \quad \boldsymbol{n}_{(3)} = \boldsymbol{e}_3 \tag{3.2.1}$$

   ii) For Axisymmetric simulations, the void axes is assumed to be rotated by 270° about $\boldsymbol{n}^{(1)}$, such that $\boldsymbol{n}^{(3)}$ is oriented parallel to $\boldsymbol{e}_3$. This is done for ease of interpretation of the aspect ratios.

$$\boldsymbol{n}_{(1)} = \boldsymbol{e}_1, \quad \boldsymbol{n}_{(2)} = \boldsymbol{e}_3, \quad \text{and} \quad \boldsymbol{n}_{(3)} = -\boldsymbol{e}_2 \tag{3.2.2}$$

The parameters are identified by comparing the simulation results of axisymmetric uniaxial tensile test to the experimental results. The identified parameter set for an axisymmetric simulation is given in Table 3.2.1 and the stress strain curve comparison is given in Fig.(3.2.1).

f_0	ε_N	S_n	f_N	w_{10}	w_{20}
1.5×10^{-4}	0.5	0.1	0.065	1.0	1.0

Table 3.2.1: VAR model Parameters

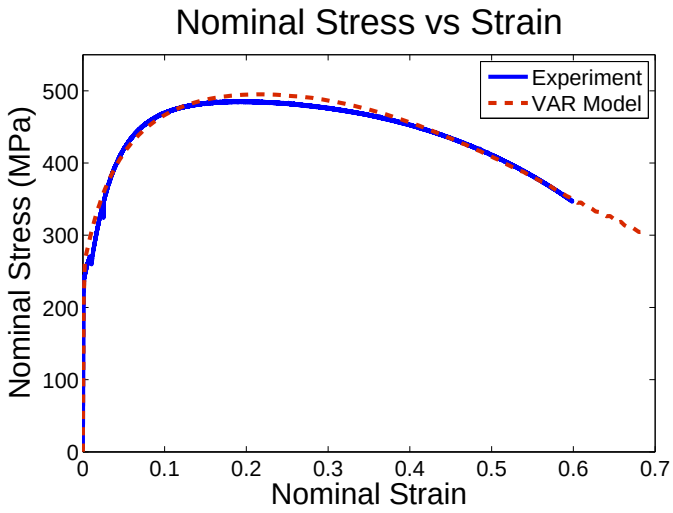

Fig. 3.2.1: Comparison of Nominal Stress-Strain curve obtained from experiment and VAR model of uniaxial tensile test

Since the numerical results from VAR model are to be compared to results from Gurson model as implemented in ABAQUS, the parameters of Gurson model should also be identified. The parameters to be identified are,

1) Initial void volume fraction f_0
   As stated in VAR model, the initial void volume fraction is take be 1.5^{-4}

2) Yield function coefficients as introduced by Tvergaard and Needleman - q_1, q_2 and q_3

   In literature, various possible values for the coefficients are mentioned. The most widely used values are $q_1 = 1.5$, $q_2 = 1$ and $q_3 = 2.25$, and $q_1 = 1$, $q_2 = 1$ and $q_3 = 1$. Recently, Dunand and Mohr [30] proposed the values $q_1 = 1$, $q_2 = 0.7$ and $q_3 = 1$. The influence of these values on the material behaviour is shown in Fig.(3.2.2). It is seen that the coefficients influence the drop in stress carrying capacity of the material, once it reaches maximum load. Hence, micromechanically it influences the void interactions.

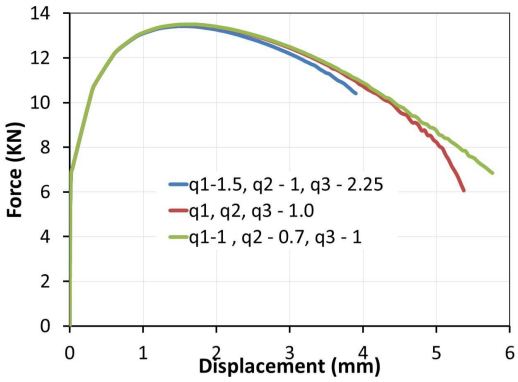

Fig. 3.2.2: Nominal Stress-Strain curve, Influence of yield function coefficients q_1 and q_2 - GTN Model

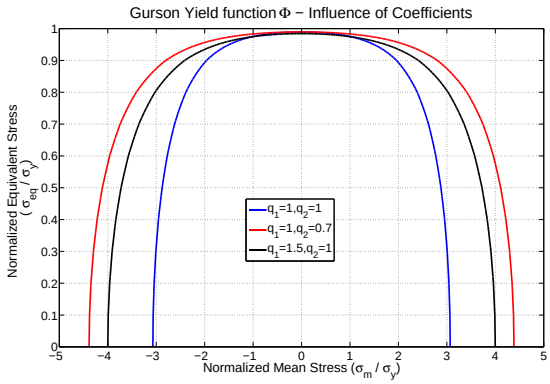

Fig. 3.2.3: Yield surface in σ_{eq} - σ_m plane, Influence of yield function coefficients q_1 and q_2 - GTN Model

Change in yield surface, with yield function coefficients is shown in Fig.(3.2.3). As seen, the yield surface for the coefficients proposed by Dunand and Mohr [30] deviates from the exact solution for pure hydrostatic stresses, and the model is much stiffer in comparison to the original Gurson model.

3) Void nucleation parameters ε_N, f_N, and S_N

4) Critical void volume fraction f_c and void volume fraction at failure f_f

Same procedure as VAR model is used to identify the parameters. The identified parameters are give in Table 3.2.2 and the corresponding stress strain curve in Fig.(3.2.4)

f_0	q_1	q_2	ε_N	S_n	f_N	f_C	f_N
1.5×10^{-4}	1	1	0.5	0.1	0.065	0.023	0.027

Table 3.2.2: GTN model parameters

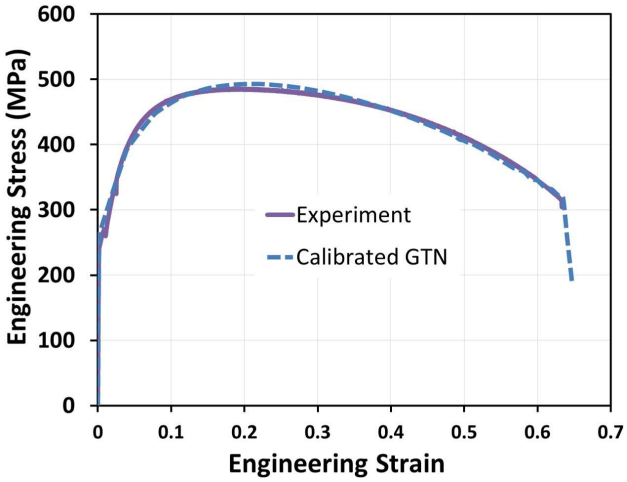

Fig. 3.2.4: Comparison of Nominal Stress-Strain curve obtained from experiment and Gurson model of uniaxial tensile test

3.3 Assessment of the constitutive model

3.3.1 Yield Surface

A comparison between the yield surface for spherical voids ($w_1 = w_2 = 1$)as predicted by VAR and Gurson model is shown in Fig.(3.3.1). The coefficients in Gurson model are taken to be $q_1 = q_2 = 1$, which corresponds to the original model proposed by Gurson [38]. The porosity is set at 1%. In forming process, the stress triaxility is usually in the range of $-1 \leq T \leq 1$, and in extreme cases it might extended upto 2. The difference between the two surfaces is narrow when the stress triaxiality is close to zero, and as the triaxiality increases the yield surface of VAR model gets broader.

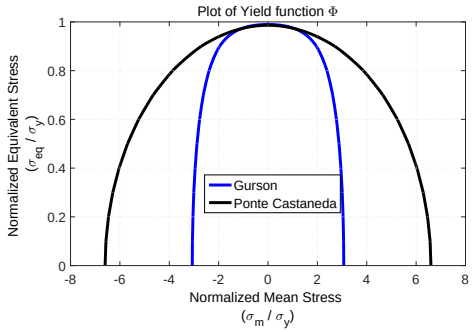

Fig. 3.3.1: Yield surface in σ_{eq} - σ_m - Comparison between VAR and Gurson model for spherical voids with $f = 1\%$

In the principal stress plane for a 2-D case, Fig.(3.3.2) shows a comparison between the yield surfaces obtained from von Mises material model, Gurson model and Ponte Castaneda (VAR) model. The void volume fraction in case of the latter 2 models is considered to be 5%. Due to the presence of voids, the yield surface

shrinks.

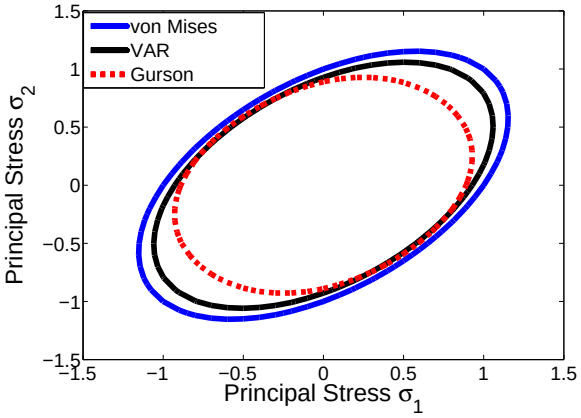

Fig. 3.3.2: Yield Surface in principal plane 2D case

For pure hydrostatic case, the yield surface of VAR model is stiffer which results in lesser void prediction. The yield surface of Gurson model is narrow and attains the analytical spherical shell solution [25]. Recalling Gurson yield function

$$\Phi = \left(\frac{\sigma_{eq}}{\sigma_y}\right)^2 + 2f\cosh\left(\frac{3\sigma_m}{2\sigma_y}\right) - 1 - f^2 \tag{3.3.1}$$

Using Taylor expansion for hyperbolic cosine term, and neglecting higher order terms, the yield function reduces to

$$\Phi = \frac{1}{(1-f)^2}\left(\frac{\sigma_{eq}}{\sigma_y}\right)^2 + \frac{9}{4}\frac{f}{(1-f)^2}\left(\frac{\sigma_m}{\sigma_y}\right)^2 - 1 \tag{3.3.2}$$

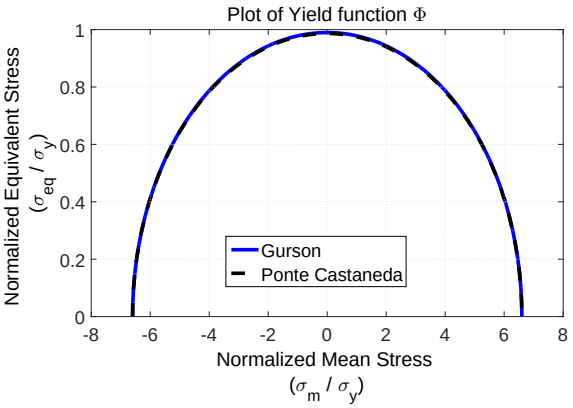

Fig. 3.3.3: Reduced Gurson yield surface according to Eq.3.3.2

On plotting the yield surface of the above reduced yield function (Fig.(3.3.3)), it is seen that for pure hydrostatic case, Gurson yield surface coincides with VAR yield surface. Hence, the last two terms in original Gurson yield function contribute

to obtain the analytical solution.

$$\Phi = \left(\frac{\sigma_{eq}}{\sigma_y}\right)^2 + \underbrace{2f\cosh\left(\frac{3\sigma_m}{2\sigma_y}\right) - 1 - f^2}_{\text{Term contributing to exact solution}} \tag{3.3.3}$$

With increase in void volume fraction, the material softens and looses its stress carrying capacity. This corresponds to shrinking of yield surface in σ_{eq}-σ_m plane. Fig.(3.3.4) depicts this behaviour of the yield function.

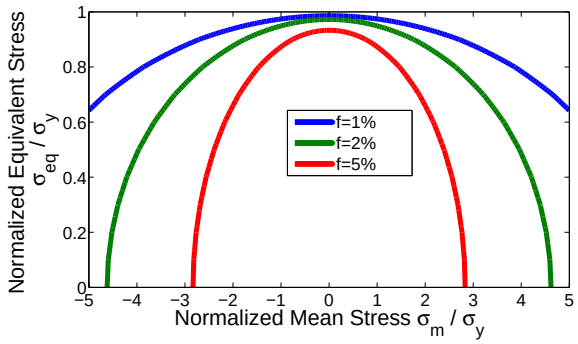

Fig. 3.3.4: Effect of f on yield surface

3.3.2 Void Growth

It is known that the evolution of void growth depends on the yield function Φ through the relation Eq.2.1.6. Due to the differences in yield function between Gurson and VAR model, the void evolution in both cases are totally different. To understand the behaviour of void evolution, a single 3-dimensional 8 noded hexahedral element is analysed. The voids are assumed to be spherical initially $w_{10} = w_{20} = 1$ with a void volume fraction of $f_0 = 1\%$, and the void nucleation terms are set to zero.

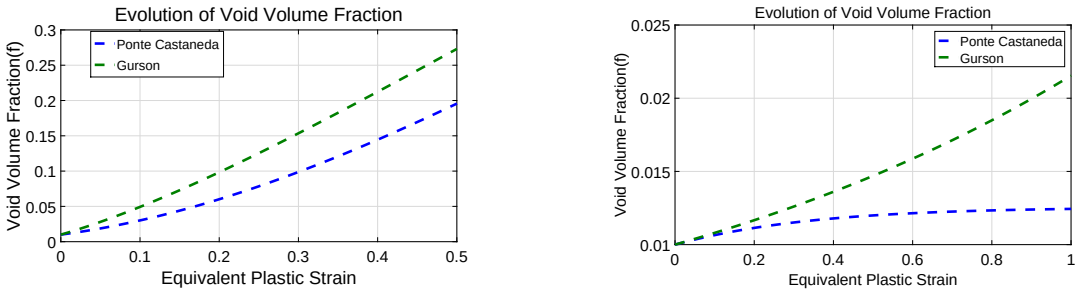

(a) Hydrostatic Tension **(b)** Uniaxial Tension

Fig. 3.3.5: Evolution of void volume fraction without considering void nucleation, in a single element test

Fig.(3.3.5a) shows the evolution of void under pure hydrostatic tension. As expected, it is seen that VAR model is overly stiff which results in underestimation of void growth. This can be correlated to wider yield surface of VAR model in pure

hydrostatic case. The void growth obtained by Gurson model is more realistic, because under pure hydrostatic loading voids grow due to dilatation, i.e. voids grow spherically.

Fig.(3.3.5b) shows the path traced by void evolution function under uniaxial tension ($T = 1/3$). VAR model predicts slower void growth in comparison to Gurson model, which is more physical. In case of uniaxial tension, the voids elongate in the direction of the loading and take the shape of a prolate ellipsoid. A sphere whose radius is equal to the major axis of a prolate void would occupy more volume in comparison to a prolate void, which is observed in case of uniaxial tension.

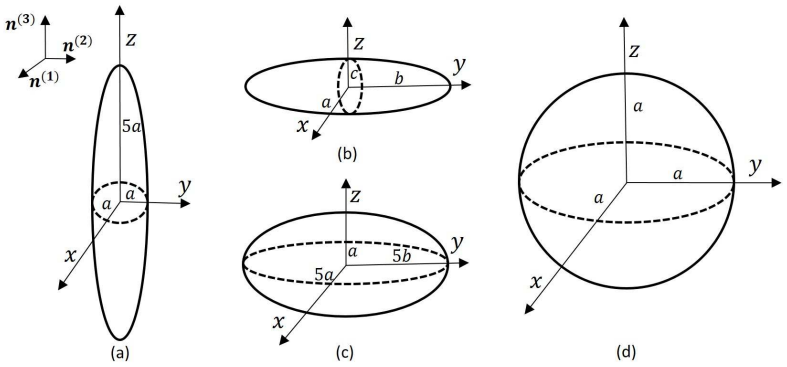

Fig. 3.3.6: Various possible void shapes a) Prolate void $w_1 = w_1 = 5$ b) Ellipsoidal void $w_1 = 5$ & $w_2 = 0.2$ c) Oblate voids $w_1 = w_1 = 0.2$ d)Spherical void $w_1 = w_1 = 1$

One of the advantages of VAR model is its capabilities to account for void shape. To understand the influence of initial void shape on evolution of void, uniaxial single element tensile test for different initial void shapes were studied. Fig.(3.3.7) describes the influence of initial void shape on void growth. It is observed that for a triaxiality of $T = 1/3$, prolate voids are stiffer than other shapes, and oblate voids are softer than others. The significant difference in void growths can be correlated to yield surface observations of Danas and Aravas [25], who observed that, for $-0.6 < \sigma_m < 1.2$ regime, the ellipsoidal voids are stiffer when compared to oblate voids for a VAR type yield function (MVAR).

3.3.3 Void Aspect Ratios

The evolution of void aspect ratio for different loading conditions are determined by carrying out single element test. Fig.(3.3.8a) shows the evolution of void aspect ratio in case of uniaxial tensile loading. The voids are assumed to be initially spherical and the element is loaded along $\boldsymbol{n}^{(3)}$ principal axes of the void. The aspect ratios w_1 and w_2 increase, as the voids elongate in the loading direction i.e. the length of semiaxis c increases, while the lengths of other two axis a and b reduce, resulting in increase of aspect ratio. Uniaxial tension results in prolate voids.

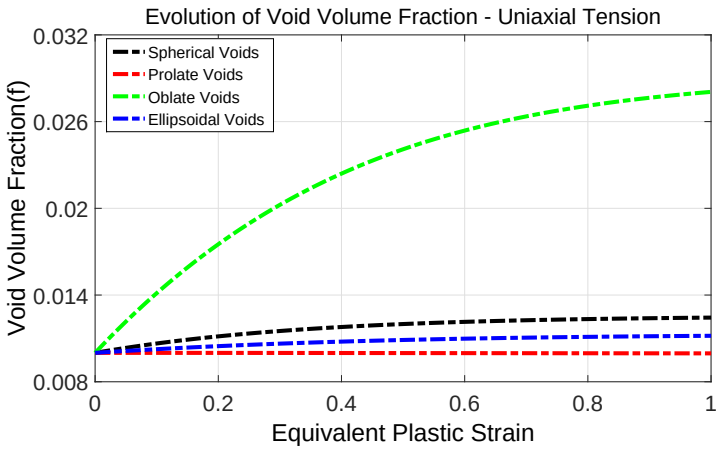

Fig. 3.3.7: Effect of initial void shape on void growth in uniaxial tensile test

Similarly, in case of uniaxial compression Fig.(3.3.8b), the aspect ratios reduce as the length of semi axis c reduces and the lengths of semi axis a and b increase. In uniaxial compression, voids grow to take oblate form. In physical sense, the behaviour of aspect ratios are as expected. This can be proved by unit cell simulations with voids under constant triaxiality. But, the unit cell simulations are not a part of this study.

For biaxial loading, the two loads are applied along $\boldsymbol{n}^{(1)}$ and $\boldsymbol{n}^{(2)}$ principal axes of

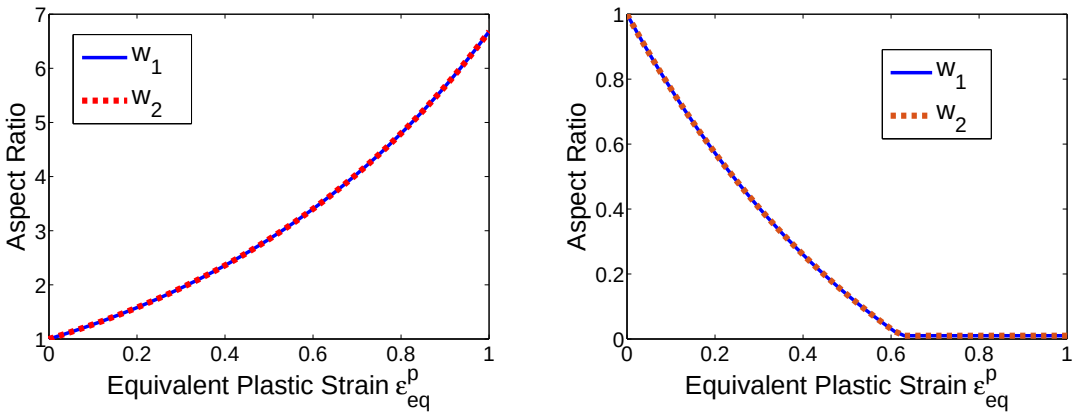

(a) Uniaxial Tension **(b)** Uniaxial Compression

Fig. 3.3.8: Evolution of void aspect ratio under uniaxial loading, as observed in single element test

the void. In biaxial tension, voids grow to take oblate form with increase in load and under compression load, the voids grow into prolate ellipsoids. The results of biaxial tension and biaxial compression single element tests are given in Fig.(3.3.9). In case of pure hydrostatic loading (triaxial load), the voids have to grow spherically, i.e. the aspect ratios should remain constant. This is evident in Fig.(3.3.10).

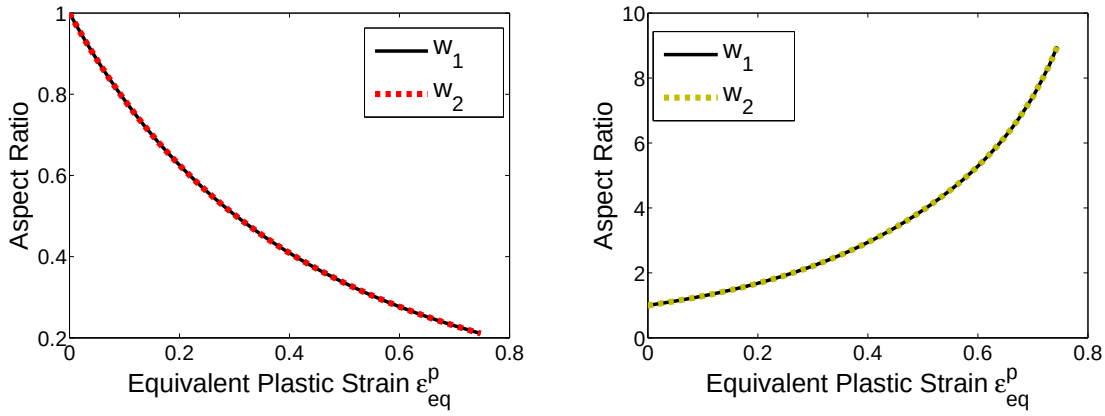

(a) Biaxial Tension **(b)** Biaxial Compression

Fig. 3.3.9: Evolution of void aspect ratio under biaxial loading, as observed in single element test

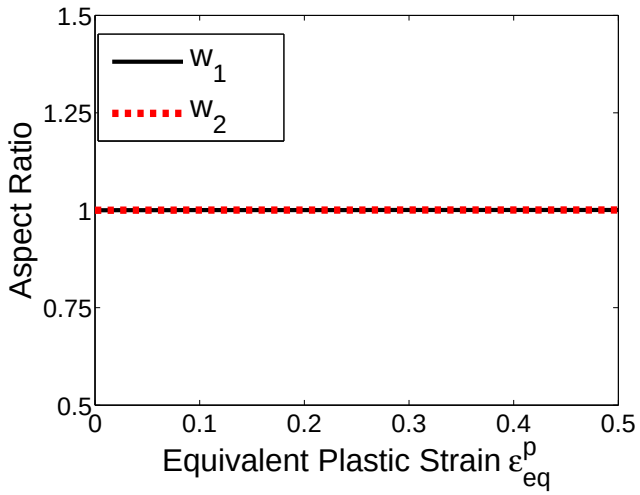

Fig. 3.3.10: Evolution of void aspect ratio - Pure hydrostatic tension, as observed in single element test

3.3.4 Void Nucleation

Strain controlled void nucleation function depends on 3 variables ε_N, f_N and S_N as described in Eq. 2.4.41. Based on observations of Chu and Needleman[23], the variable S_N is considered to be a constant $S_N = 0.1$. An optimum way to understand the influence of ε_N and f_N on material behaviour, is to study the variation of nominal stress-strain curve of a uniaxial tensile test.

f_N gives the total volume of nucleated voids. Fig.(3.3.11a) shows that with increase in f_N, the stress carrying capacity of the specimen reduces. This is because with increase in f_N, the number of voids nucleated increase, which makes the material softer. Higher the value of ε_N, later the voids would nucleate. As the voids nucleate late, the maximum stress shifts to the right in stress-strain curve. This could be observed in Fig.(3.3.11b). The shift is not quite significant when f_N is less.

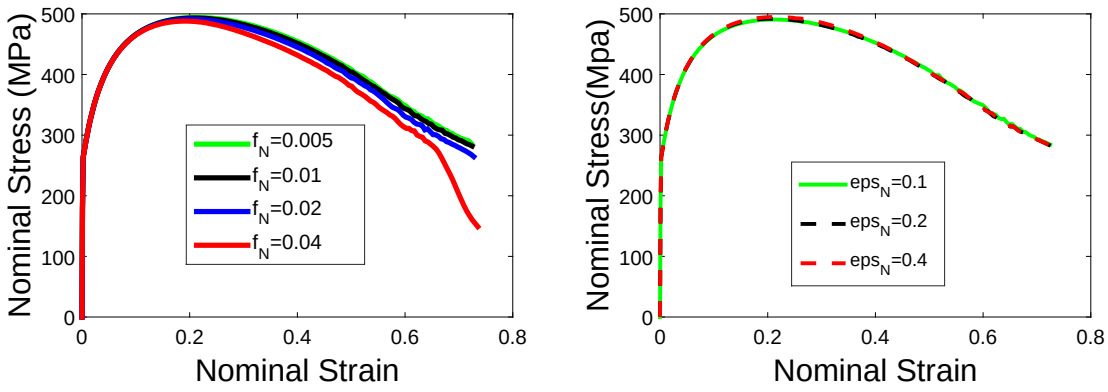

(a) Influence of f_N **(b)** Influence of ε_N

Fig. 3.3.11: Influence of void nucleation parameters - stress strain curve of uniaxial tensile test

3.3.5 Void Coalescence

Recalling Thomason based coalescence criteria, we have

$$C_t = \frac{\sigma_{max}^{Pr}/\sigma_y}{[1-\chi_i^2]\left[\alpha\left(\frac{1-\chi_i}{\chi_i w_i}\right)^2 + \beta\chi_i^{-1/2}\right]} \tag{3.3.4}$$

and Benzerga coalescence criteria

$$C_b = \frac{\sigma_{max}^{Pr}/\sigma_y}{[1-\chi_i^2]\left[\alpha\left(\frac{\chi_i^{-1}-1}{w_i^2+0.1\chi_i^{-1}+0.02\chi_i^{-2}}\right)^2 + 1.3\chi_i^{-1/2}\right]} \tag{3.3.5}$$

It is clear that the coalescence criteria depend on equivalent plastic strain ε_{eq}^p, aspect ratio w_i and void volume fraction f. To understand the behaviour of coalescence criteria, the variation of functions in the denominator of critical values are evaluated, i.e. R and S in Eq.3.3.6.

$$R = \frac{1}{[1-\chi_i^2]\left[\alpha\left(\frac{1-\chi_i}{\chi_i w_i}\right)^2 + \beta\chi_i^{-1/2}\right]} \tag{3.3.6a}$$

$$S = \frac{1}{[1-\chi_i^2]\left[\alpha\left(\frac{\chi_i^{-1}-1}{w_i^2+0.1\chi_i^{-1}+0.02\chi_i^{-2}}\right)^2 + 1.3\chi_i^{-1/2}\right]} \tag{3.3.6b}$$

Fig.(3.3.12) shows variation of R and S with equivalent plastic strain for spherical void with void volume fraction of 1%. It is important to note that, the functions

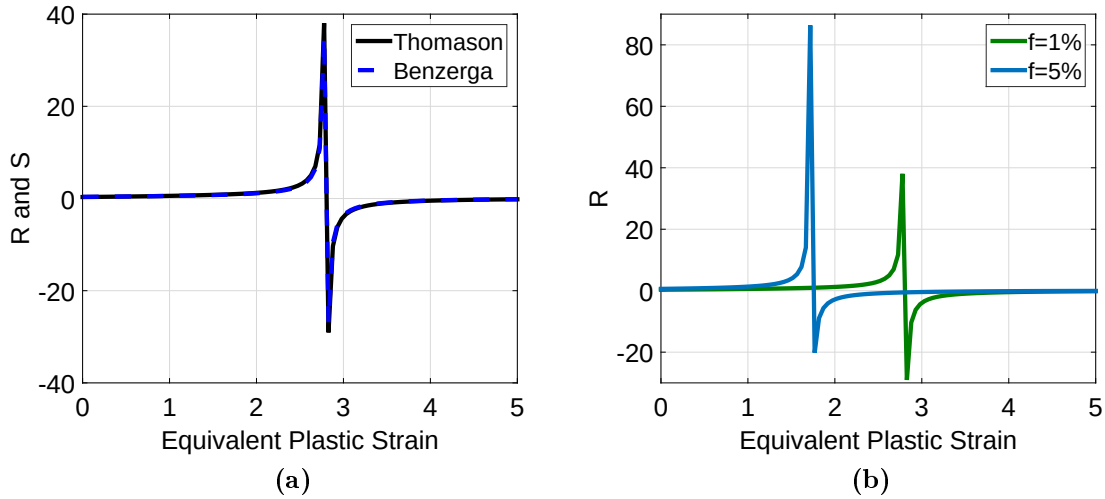

Fig. 3.3.12: Variation of R and S with equivalent plastic strain a) for void volume fraction $f = 1\%$ b) for void volume fraction $f = 1\%$ and $f = 5\%$

oscillate at certain plastic strain, which would lead to very high coalescence values. The occurrence of the oscillation is influenced by void volume fraction, as shown in Fig.(3.3.12b). The greater the void volume fraction, the earlier is the oscillation.

The variation of R and S with aspect ratio is described in Fig.(3.3.13). It is seen that the influence of smaller aspect ratios on void coalescence critical value is very high in comparison to the influence of larger aspect ratios. This analysis has been seldom carried out in literature to prove the observations through experiments. A detailed study in this regard has to be carried out in this context, which would not be a part of this study.

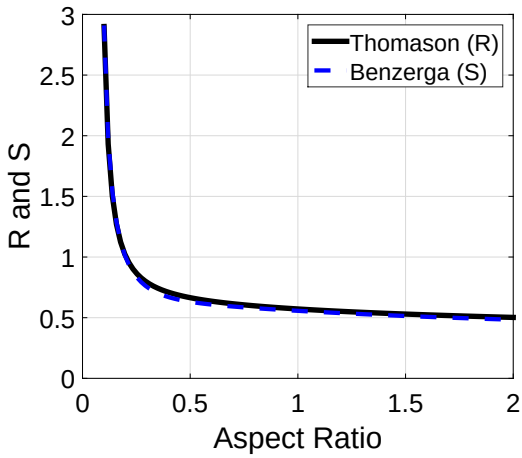

Fig. 3.3.13: Variation of R and S with aspect ratio for void volume fractions of $f = 1\%$

Chapter 4

Application of the constitutive model

In this section, the results obtained from simulation of bulk forming experiments using VAR model is described. The obtained results are later compared to experimental results and other damage models. The first three experiments in the following section were carried out at Fraunhofer IWM and the 4th example details were obtained from an industrial partner in the framework of AIF project - IGF 17678-N Schadensvorhersage in der Kaltmassivumformung, and the same results are used here.

4.1 Uniaxial Tensile Test

A round bar of 6 *mm* diameter is subjected to uniaxial tensile load. Fig.(4.1.1) outlines the dimension of the test specimen. An 8 *mm* extensometer is used to measure the displacement, and the experiment is carried out at close to zero strain rate and at room temperature. The micro-structure at the center axis of the specimen before fracture is shown in Fig.(4.1.2).

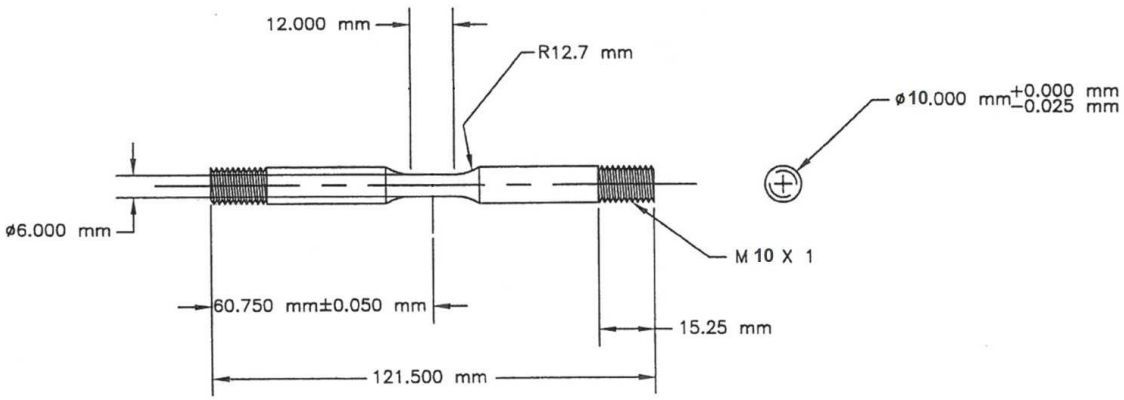

Fig. 4.1.1: Dimension of uniaxial tensile test specimen

Due to symmetry of the specimen about its axis and about its center plane, a quarter of the specimen is modelled using axisymmetric reduced integration elements as shown in Fig.(4.1.4). The results obtained from 3-dimensional numerical model

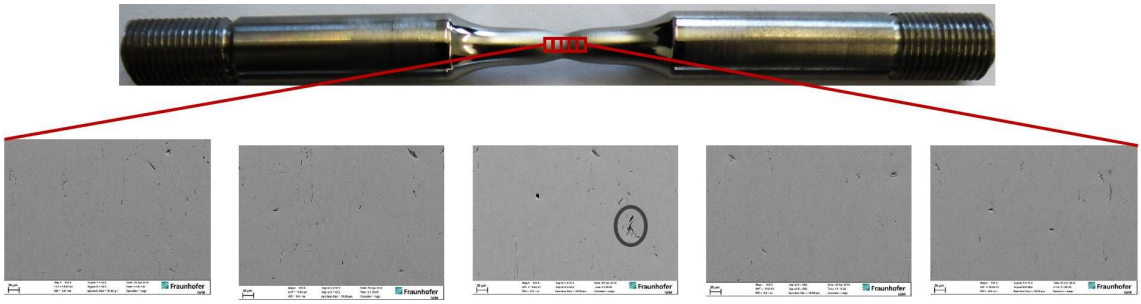

Fig. 4.1.2: Microstructure of the round bar in the necking region

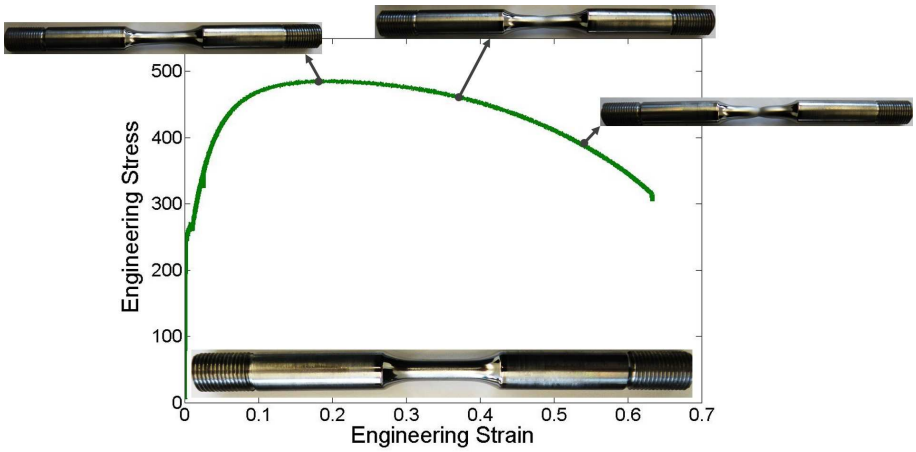

Fig. 4.1.3: Stress strain curve of tensile test

and axisymmetric model were analysed, and it was determined that they were similar. Hence, to save computation power, axisymmetric models were used. To avoid

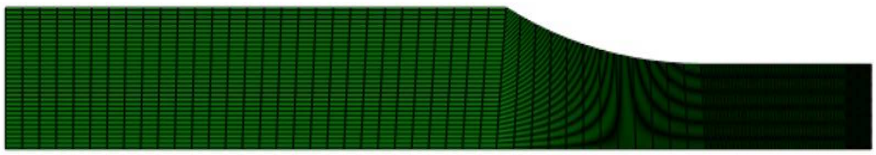

Fig. 4.1.4: Stress Strain curve of Tensile test

element localization towards the end of the simulation, a fine mesh with average element size of 0.1 mm is used in the necking region. It is observed that the stress-strain curve after maximum load is influenced by mesh size and mass scaling, hence it is important to use the same element size and mass scaling for all simulations.

For numerical simulations, the parameters identified in previous chapter are used. In case of VAR model, the voids are assumed to be initially spherical ($w_1 = w_2 = 1$) and the specimen is loaded in the direction of $\boldsymbol{n}^{(3)}$. For Gurson model, the critical void volume fraction f_c and void volume fraction at fracture f_f are not used, to allow the simulation to continue. Fig.(4.1.5) shows the agreement of stress strain curve of VAR model and Gurson model to the experimental results. The diameter of the specimen after necking measured from the experiments was closely in agreement with the numerical simulations. Fig.(4.1.6) gives the variation of the diameter along

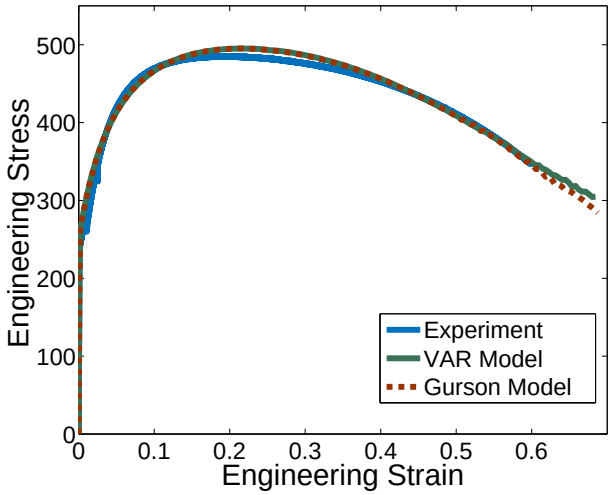

Fig. 4.1.5: Stress Strain curve as obtained from FE simulation

the loading path. The diameter after fracture was measured to be 3.15 mm. In the experiment, the specimen breaks at a strain of 0.61. The diameter of the specimen corresponding to this strain obtained from the numerical simulation (Fig.(4.1.6)) is found to be 3.1 mm.

The field distribution of equivalent plastic strain, von Mises stress and stress

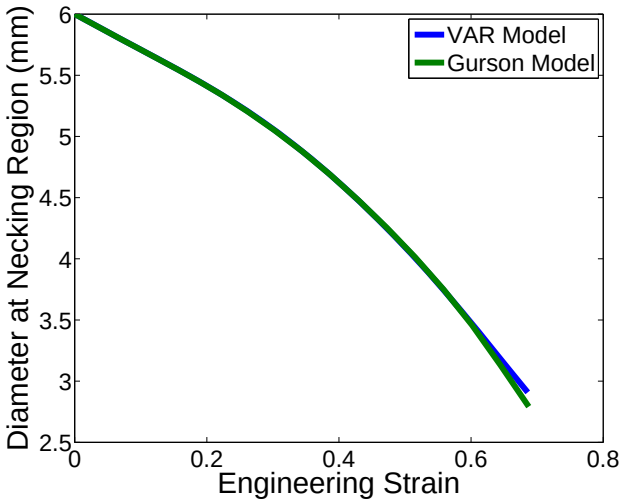

Fig. 4.1.6: Change in diameter of the specimen at the center as obtained from FE simulation

triaxiality is given in Fig.(4.1.7) and the distribution of total void volume fraction, void growth and void nucleation is given in Fig.(4.1.8). Maximum voids nucleate in the necking region due to high plastic strain and positive stress triaxiality.

A comparison of the critical damage parameter of various phenomenological damage models, Gurson model and VAR model is given in Fig.(4.1.9). It can be seen that, all damage models predict the location of damage at the center of the specimen, in agreement to the experiment. However, the void volume fraction predicted by VAR model is less compared to Gurson model and other models do not give the details

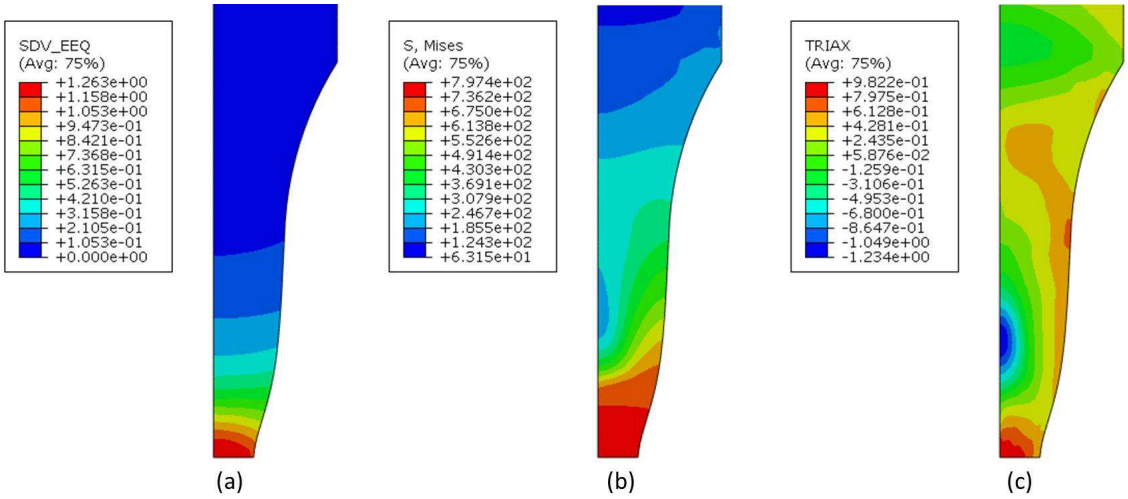

Fig. 4.1.7: a) Distribution of equivalent plastic strain ε^p_{eq} b) distribution of von Mises or equivalent stress $\boldsymbol{\sigma}_{eq}$ c) stress triaxiality T, as obtained from FE simulation using VAR model

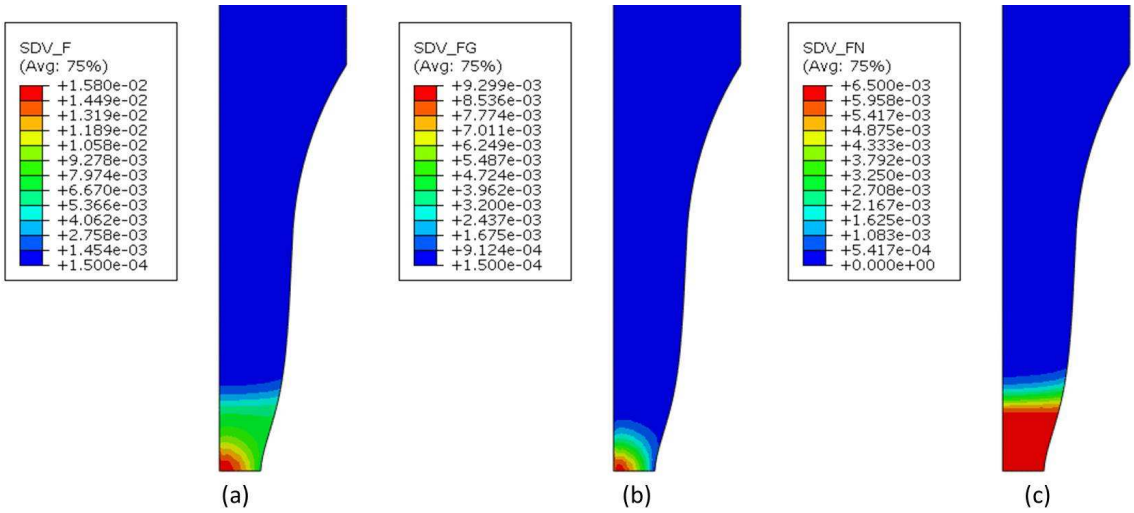

Fig. 4.1.8: a) Total void volume fraction b) void volume fraction due to growth c) nucleated void volume fraction as obtained from FE simulation using VAR model

about void shape, as opposed to VAR model.

A comparison of evolution of void volume fraction in an element at the center of the specimen as obtained from VAR and Gurson model is given in Fig.(4.1.11). The observations are in agreement to the conclusions from the yield surface analysis in previous section. The voids volume fraction predicted by VAR model is lower than Gurson model due to elliptical voids. Fig.(4.1.12) gives the increase in aspect ratio at center element and Fig.(4.1.13) shows the distribution of aspect ratios in the specimen. The voids elongate in the loading direction, and take the prolate shape. As the model is axisymmetric, the semi axes a and b evolve proportional.

Thomason coalescence criteria and Benzerga coalescence criteria are analysed. Fig.(4.1.14) shows the distribution of the critical values in the specimen. Since

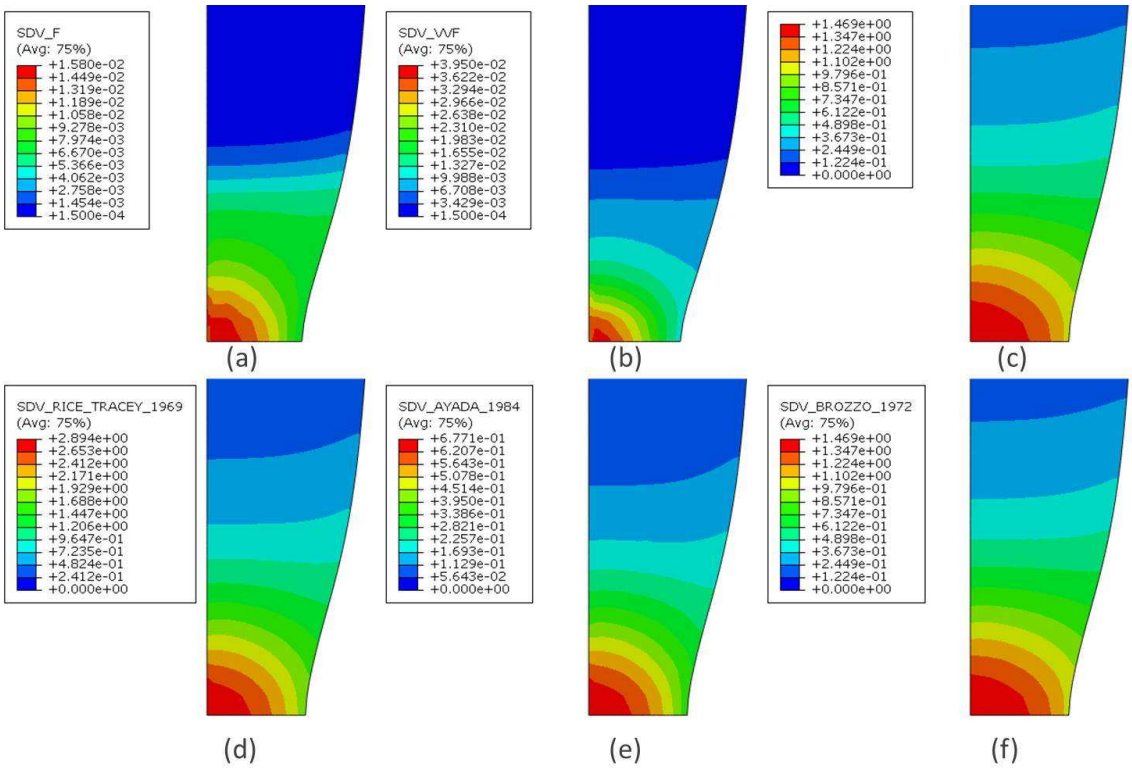

Fig. 4.1.9: a) void volume fraction of VAR model b) void volume fraction of Gurson model c) Cockroft Latham damage variable d) Rice and Tracy damage variable e) Ayada damage variable f)Brozzo damage variable

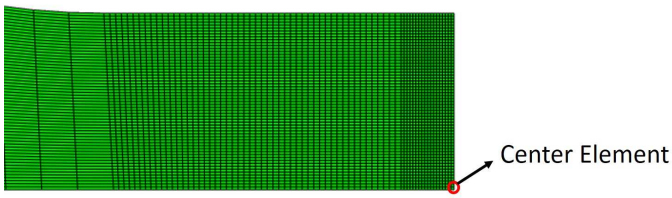

Fig. 4.1.10: Center element used for further analysis

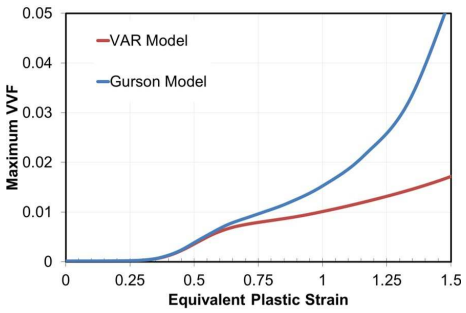

Fig. 4.1.11: Evolution of VVF at the center element

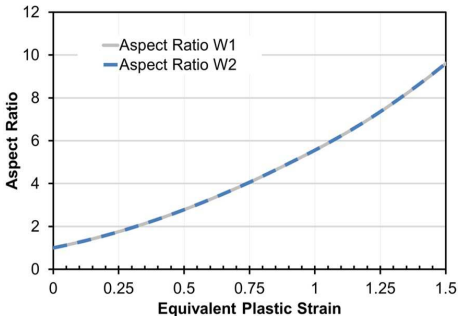

Fig. 4.1.12: Evolution of aspect ratio at the center element

$w_1 = w_2$, the critical values obtained from all three planes w_1, w_2 and w_{eff} are the same. Fig.(4.1.15) gives the variation of coalescence criteria in the center element. The plot gives the variation of the critical value obtained from Gurson model as

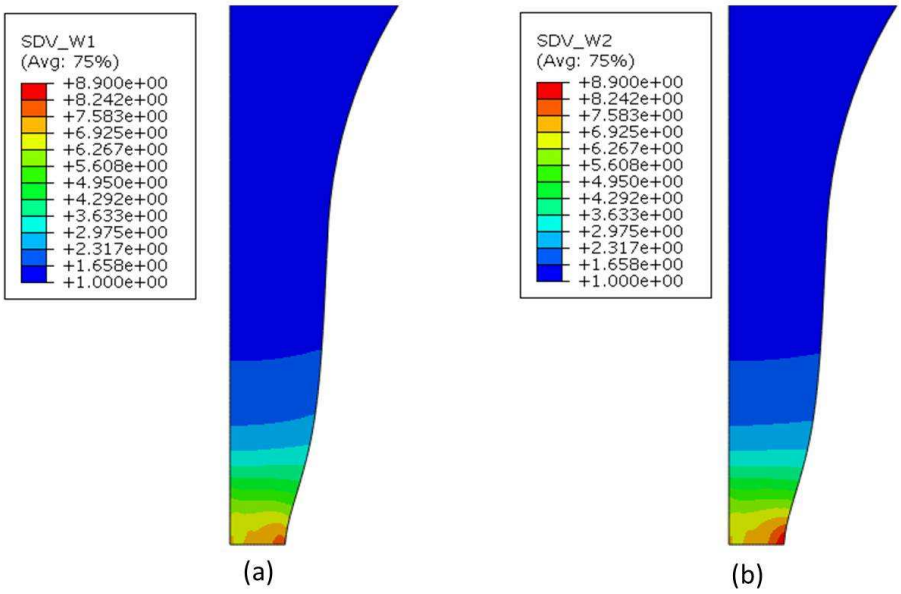

Fig. 4.1.13: Distribution a) Aspect ratio w_1 b) Aspect ratio w_2 obtained from VAR material model

well. The value obtained from Gurson model are higher as it predicts higher void volume fraction. Also, it can be observed that coalescence parameter C depends on stress triaxiality. It can be concluded that there is no one specific critical value which determines the void coalesce for VAR model. In the literature, the coalescence conditions are typically qualified using unit cell simulations and do not consider void rotation in 3-dimensional case. A need arises for a new coalescence model, which considers the void rotation and void shape appropriately.

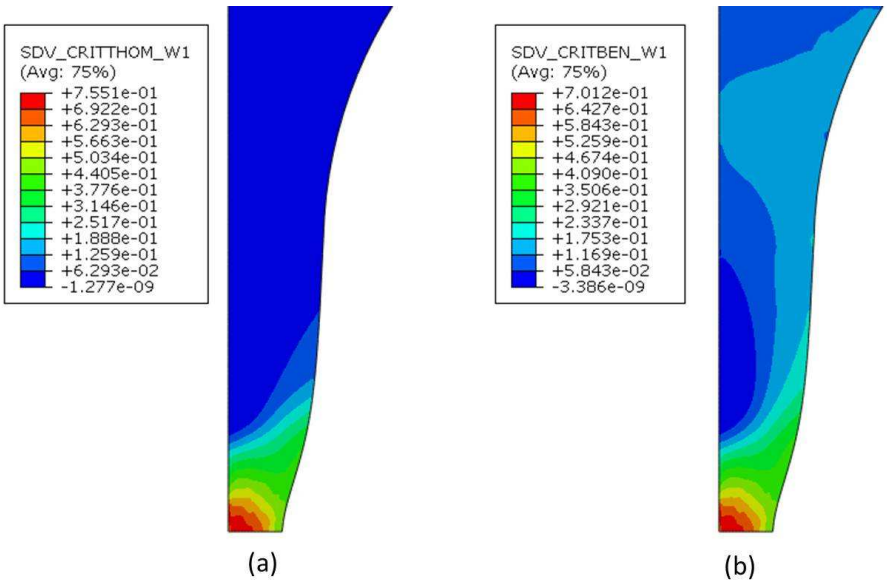

Fig. 4.1.14: Distribution of a) Thomason Coalescence Criteria b) Benzerga Colaescence criteria as obtained from VAR material model

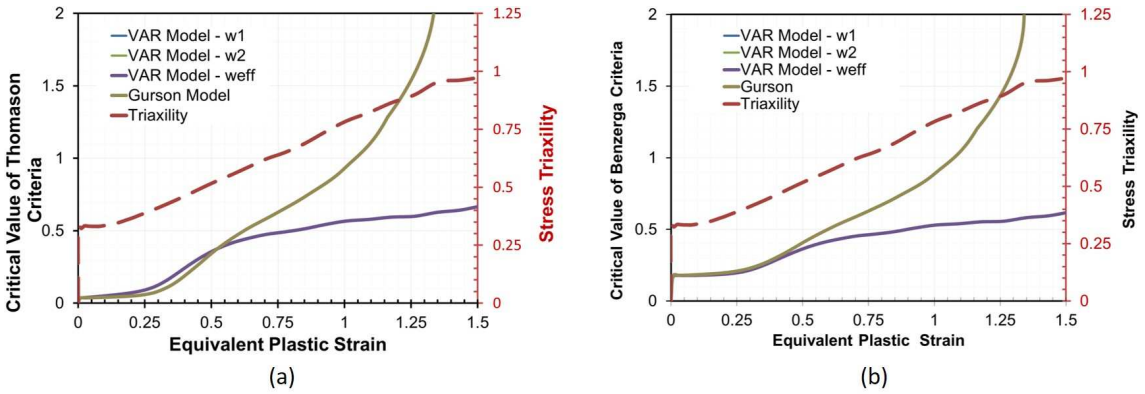

Fig. 4.1.15: Variation of a) Thomason Coalescence Criteria b) Benzerga Colaescence criteria of the center element

4.2 Uniaxial Compression Tests/ Upsetting Test

A round bar of 20 mm diameter and 45 mm height is subjected to compression loading in the testing machine. The displacement in the specimen is calculated from the machine displacement. First, the elasticity of the machine is determined by conducting a pseudo test without a specimen. The elasticity is used to calculate a corrector, which is later used to determine the specimen displacement from the machine displacement. An optical instrument is used to measure the instantaneous maximum diameter of the specimen throughout the experiment. The dimension of the specimen in outlined in Fig.(4.2.1). Due to symmetry, $1/4^{th}$ of the specimen is modelled using reduced axisymmetric elements in ABAQUS.

For numerical simulations, 4-nodded quadrilateral elements with an average mesh

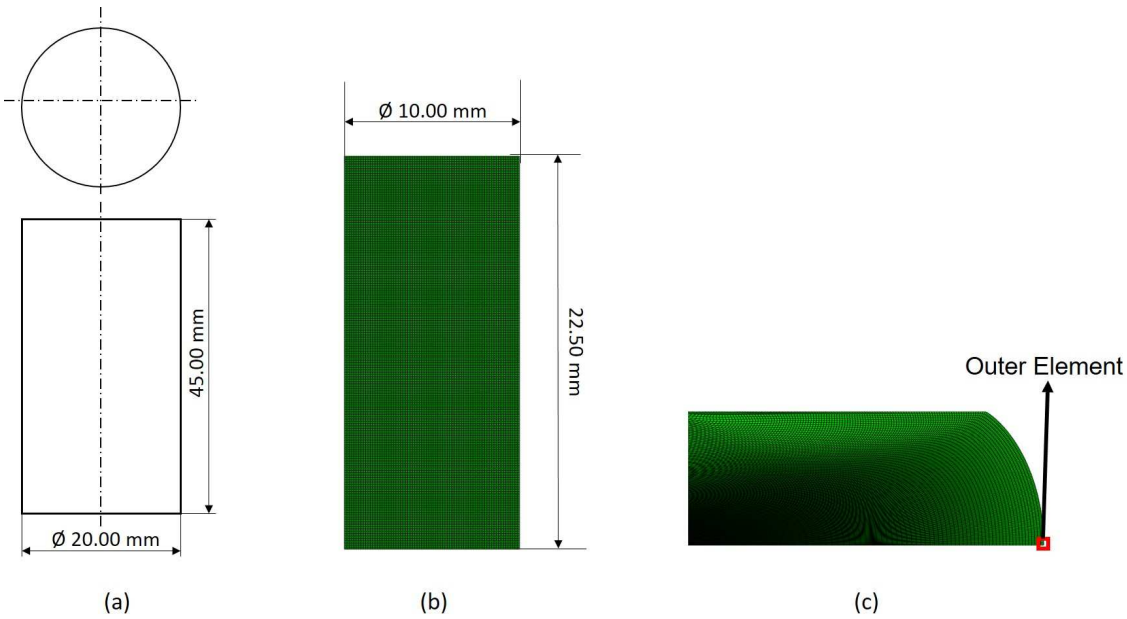

Fig. 4.2.1: Variation of a) Specimen Dimension b) Numerical model used for simulation c) The outer element used for further analysis

size of 0.1 is used. The punch is modelled as a rigid body with surface contact.

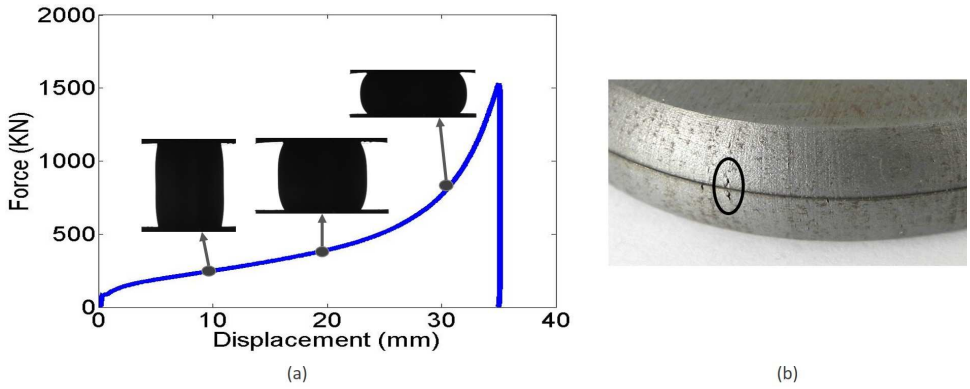

Fig. 4.2.2: a) Experimental Force-Displacement curve b) A minor crack on the surface of the specimen at the end of the experiment

Since no lubricant is used between the contact surfaces in the experiment, a coefficient of friction of 0.4 is used for the numerical simulation. It is to be noted that, the final shape of the specimen and the Force-Displacement curve is influenced by coefficient of friction. $\boldsymbol{n}^{(3)}$ principal axis of the void is aligned along y axes of the global axisymmetric coordinate system. The specimen is loaded along $\boldsymbol{n}^{(3)}$ axis of the ellipsoidal void.

Fig.(4.2.3) and Fig (4.2.4) shows the close agreement of the experimental results

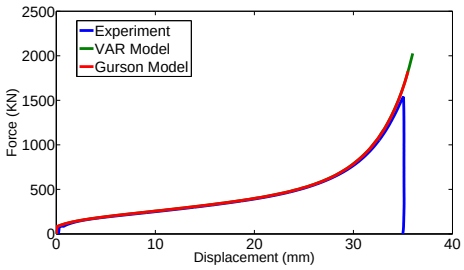

Fig. 4.2.3: Force-Displacement curve obtained from VAR and Gurson model

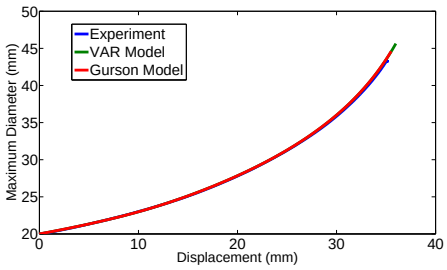

Fig. 4.2.4: Path of Maximum diameter through the experiment

to numerical results, including the maximum diameter of the specimen. Fig.(4.2.5) gives a comparison of the critical values of different damage models. The void volume fraction predicted by VAR and Gurson model are almost the same due to very low positive stress triaxiality on the surface, and the voids nucleate at very high equivalent plastic strains.

Fig.(4.2.7) gives the distribution of aspect ratios in the specimen. It shows that the voids at the top center of the specimen remain spherical. From Fig.(4.2.6) it is clear that the equivalent plastic strain and stress triaxiality experienced in this region is close to zero, due to which the voids do not alter their shape. However, the voids are elliptical towards the circumference of the specimen. The major axes of the void is along the circumference, due to which w_2 is smaller than w_1.

Fig.(4.2.9) shows the variation of aspect ratio of the outer element with loading. Due to compression, the length of c semi axis of void decreases, and a and b increases. Initially, a and b increase at same magnitude. However, when the specimen

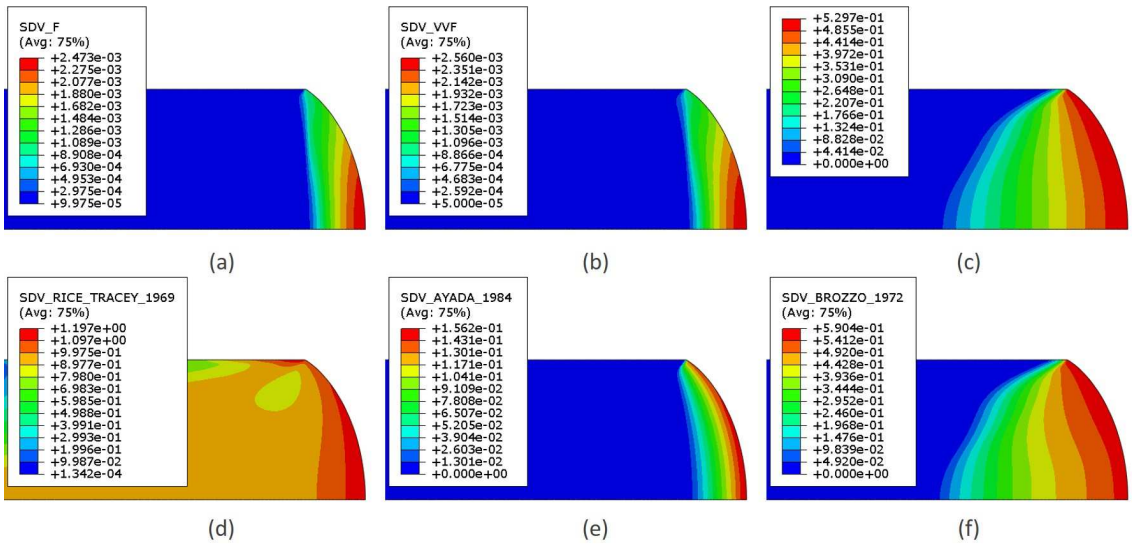

Fig. 4.2.5: a) void volume fraction of VAR model b) void volume fraction of Gurson model c) Cockroft Latham damage variable d) Rice and Tracy damage variable e) Ayada damage variable f)Brozzo damage variable

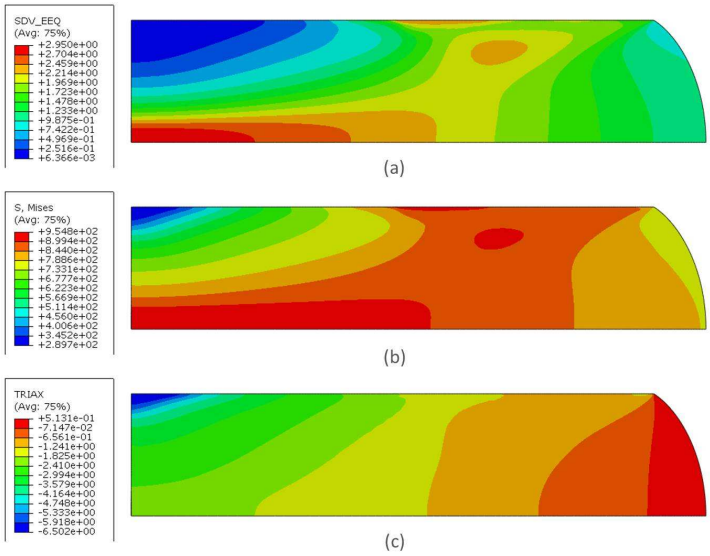

Fig. 4.2.6: Distribution of a) Equivalent plastic strain b) von Mises stress c) Stress triaxiality as obtained from VAR model

starts bulging due to friction, they diverge, and voids take the elliptical form. The aspect ratios do not evolve when the voids are assumed to be completely closed, which explains the horizontal curve in Fig.(4.2.9). Fig.(4.2.8) gives the variation of f in the outer element. The steep increase in VVF signifies nucleation of voids.

Fig.(4.2.10) and Fig.(4.2.11) show the distribution of coalescence criteria. Since the aspect ratios are different, the distribution of critical values are also different. The values obtained by Benzerga criteria is higher due to the additional quadratic term in the denominator. In comparison to uniaxial tensile test, the critical values obtained here are much smaller. This is due to lesser void volume fraction and low

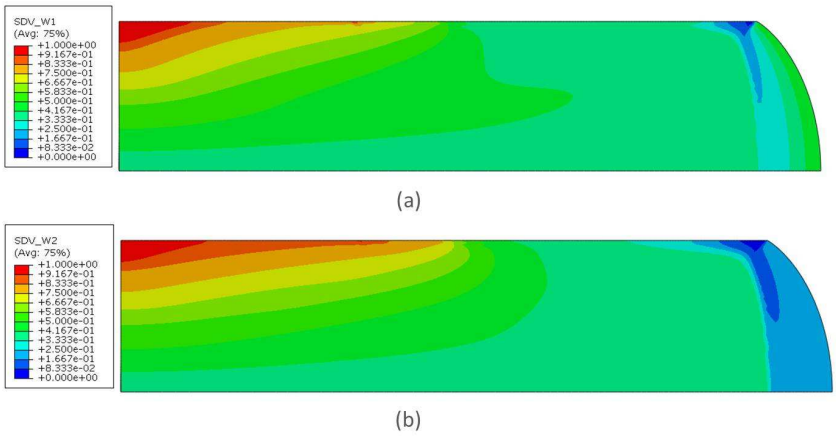

Fig. 4.2.7: Distribution of a) Aspect ratio w_1 b) Aspect ratio w_2 - VAR model

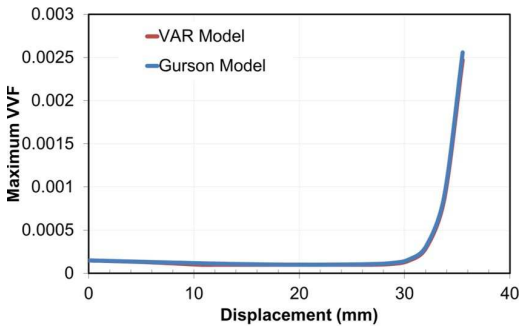

Fig. 4.2.8: Variation of f in the outer element

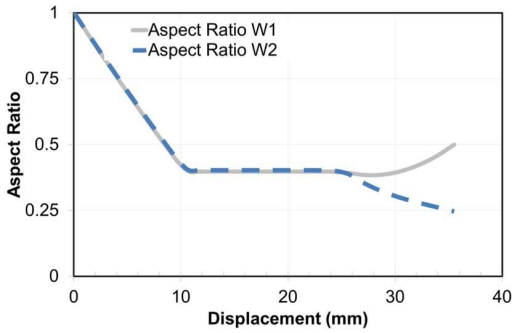

Fig. 4.2.9: Variation of aspect ratio in outer element

triaxiality.

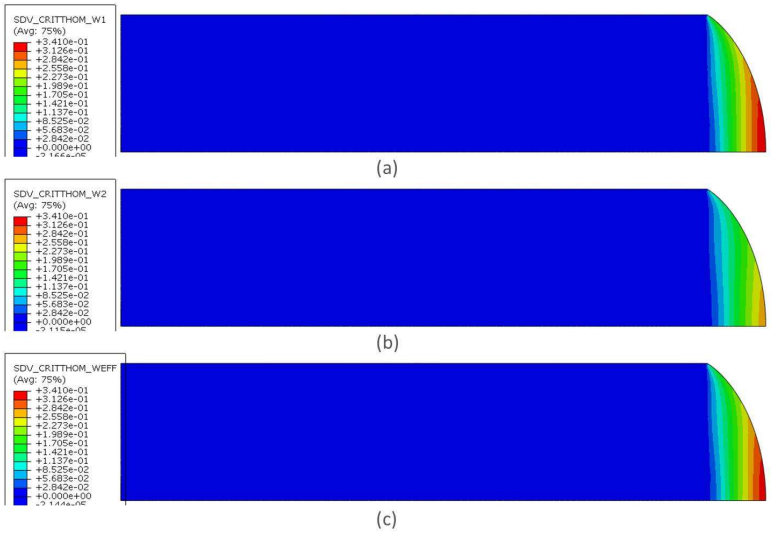

Fig. 4.2.10: Thomason Coalescence Criteria

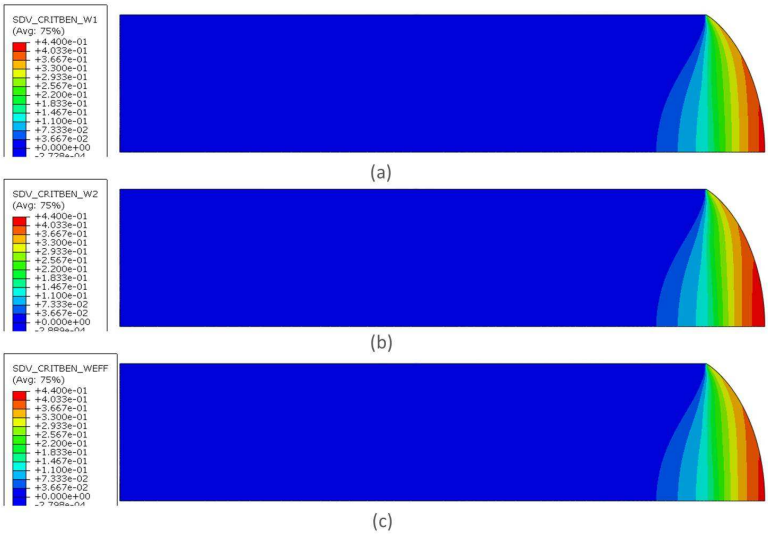

Fig. 4.2.11: Benzerga Coalescence Criteria

4.3 Cylinder with Notch

A round bar of 18 mm diameter and 27 mm height, with a notch as shown in Fig.(4.3.1), is subjected to compression loading. This experiment is advantageous as the region where damage occurs is known, the damage occurs in the notched region. This allows for tracking the first visible crack. A high resolution, high speed camera is used to capture the crack initiation. Due to symmetry, $1/4^{th}$ of the specimen is modelled. 3 dimensional elements are used, as the specimen is not axisymmetric.

For numerical simulations, 8-nodded hexahedron elements with an average mesh size of 0.1 is used. The punch is modelled as a rigid body with surface contact. Since no lubricant is used between the contact surfaces in the experiment, a coefficient of friction of 0.4 is used for the numerical simulation. It is to be noted that, the final shape of the specimen and the Force-Displacement curve is influenced by coefficient of friction. The void principal axes are aligned along the global Euler axes i.e. $\boldsymbol{n}^{(1)}$, $\boldsymbol{n}^{(2)}$ and $\boldsymbol{n}^{(3)}$ along x, y and z. The direction of loading is along $\boldsymbol{n}^{(3)}$ i.e z axis of the global coordinate system.

Fig.(4.3.2) describes the force displacement curve. The first visible crack was spotted at a displacement of 16.5 mm.

Fig.(4.3.3) shows the close agreement of the experimental results to numerical results. Fig.(4.3.4) gives a comparison of the critical values of different damage models.

Fig.(4.3.6) outlines the distribution of aspect ratios in the specimen. Similar to upsetting test, the voids at the top center of the specimen are more spherical. However, the voids are elliptical in the notch region. The major axis of the void are along the circumference of, due to which the aspect ratio w_1 is smaller. This implies that the void on the surface coalesce first, and the crack grows inwards with loading.

Fig.(4.3.8) shows the variation of aspect ratio of the outer element with loading. w_2 decreases initially and as the stress triaxiality increases, w_2 also increases. Fig.(4.3.9)

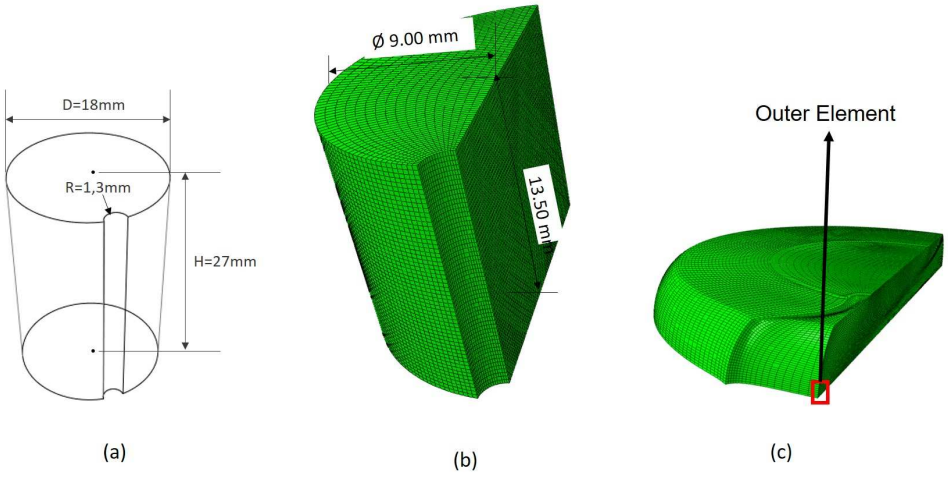

Fig. 4.3.1: Variation of a) Specimen Dimension [12] b) Numerical model used for simulation c) The outer element used for further analysis

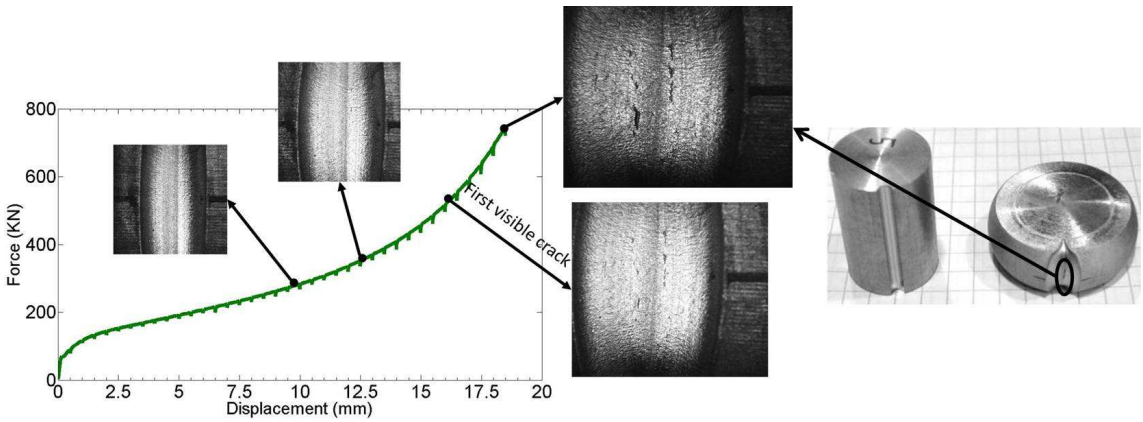

Fig. 4.3.2: Experimental Force-Displacement curve with images from the notch region

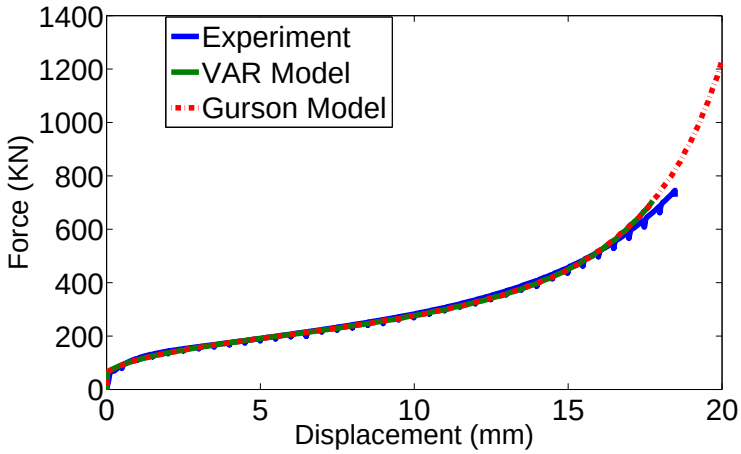

Fig. 4.3.3: Force-Displacement curve obtained from VAR and Gurson model

and Fig.(4.3.10) show the distribution of coalescence criteria critical condition. Since the aspect ratios are different, the distribution of critical values are also different.

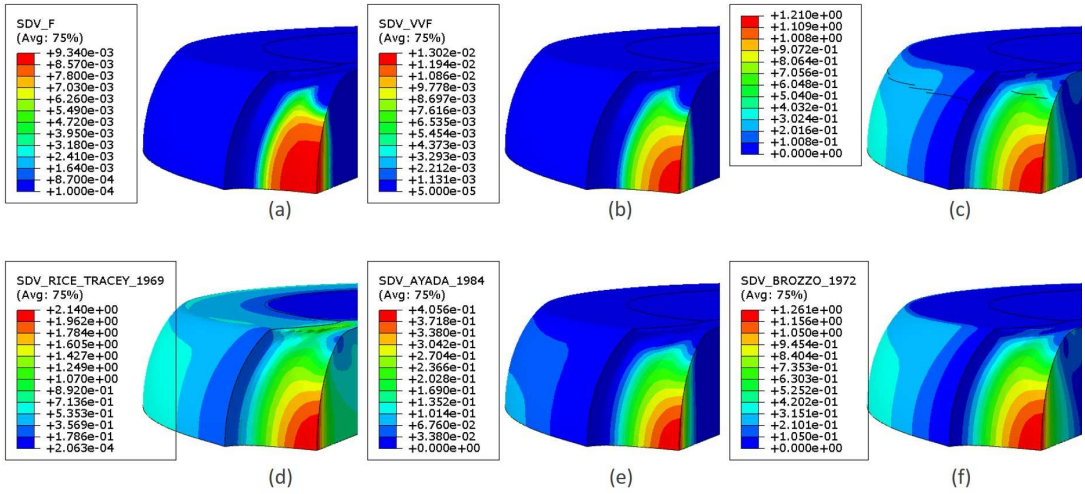

Fig. 4.3.4: a) void volume fraction of VAR model b) void volume fraction of Gurson model c) Cockroft Latham damage variable d) Rice and Tracy damage variable e) Ayada damage variable f)Brozzo damage variable

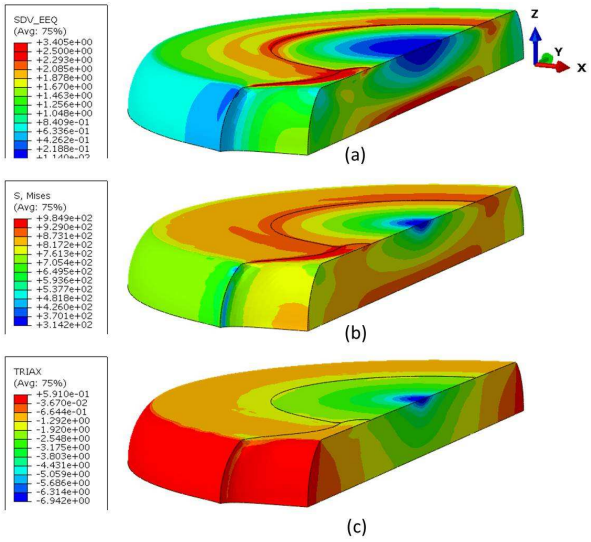

Fig. 4.3.5: Distribution of a) Equivalent plastic strain b) von Mises stress c) Stress triaxiality as obtained from VAR model

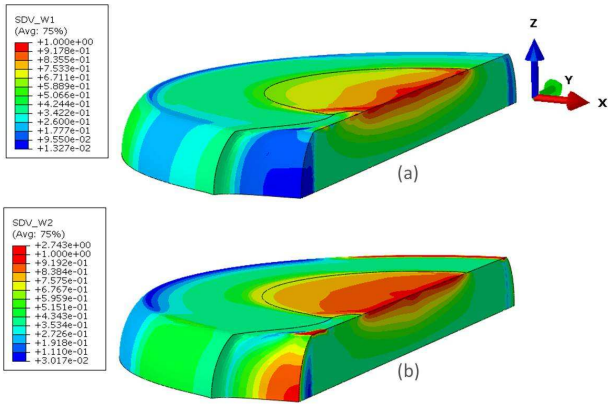

Fig. 4.3.6: Distribution of a) Aspect ratio w_1 b) Aspect ratio w_2 - VAR model

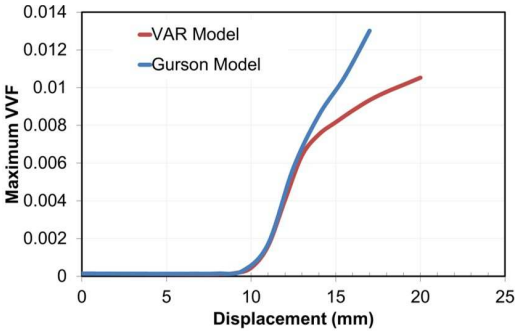

Fig. 4.3.7: Variation of f in the outer element

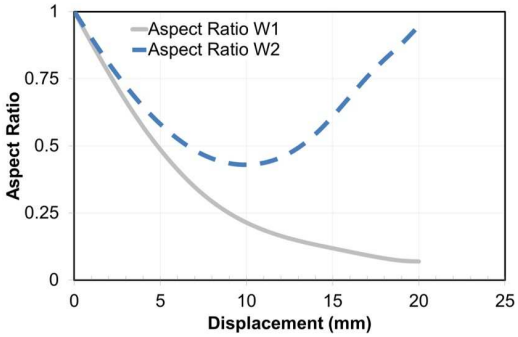

Fig. 4.3.8: Variation of aspect ratio in outer element

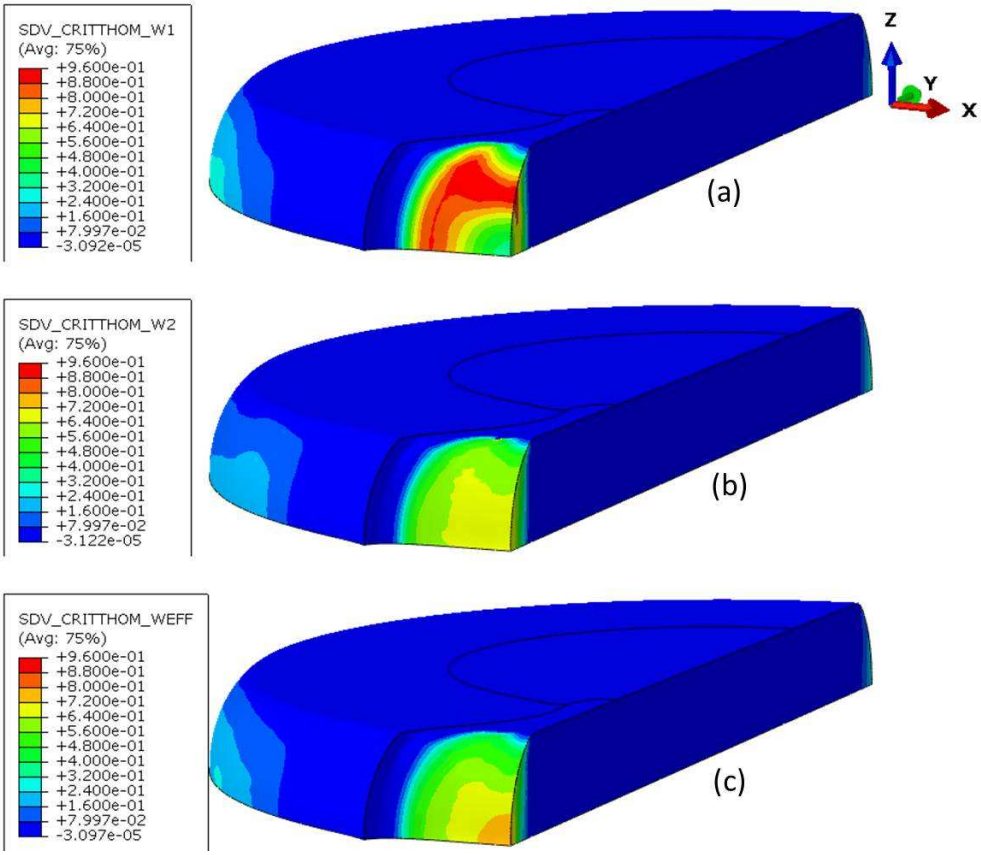

Fig. 4.3.9: Thomason Coalescence Criteria

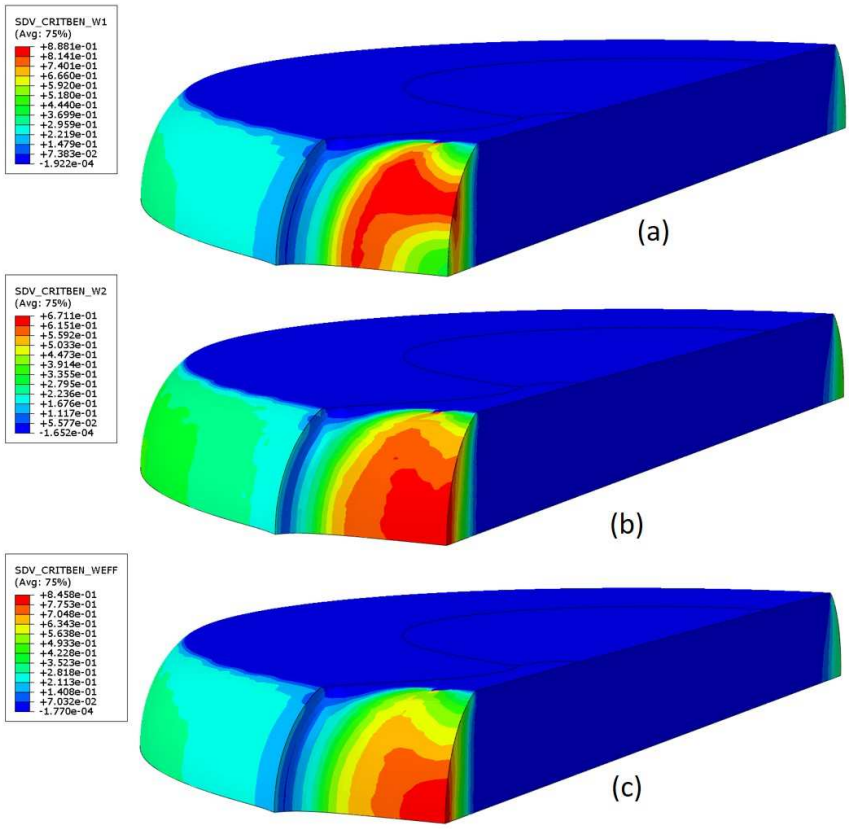

Fig. 4.3.10: Benzerga Coalescence Criteria

4.4 Industrial Example

The VAR model is used to simulate an actual cold bulk forming process to manufacture a shaft with flange as shown in Fig.(4.4.1). The manufacturing process consists of 4 steps. During the manufacturing process, it was observed that certain parts had developed cracks on the flange surface. Here, we observe if the damage models predict damage at the right location.

Since the part is axisymmetric, a 4 noded, quadrilateral reduced integration axisymmetric element is used for simulation. A contact pressure dependent friction model (Table 4.4.1) is used for the metal-die interface. The tools are modelled as rigid bodies and a penalty contact friction model is used for interface. Velocity boundary conditions are applied on the reference point of each tool. The various steps in numerical simulation is shown in Fig.(4.4.1).

Since the coalescence model is premature for VAR model, void volume fraction f

Coefficient of Friction(μ)	Contact pressure
0.12	0
0.12	500
0.1	550
0.08	600
0.06	650
0.04	700
0.02	750
0	800

Table 4.4.1: Pressure dependent coefficient of friction

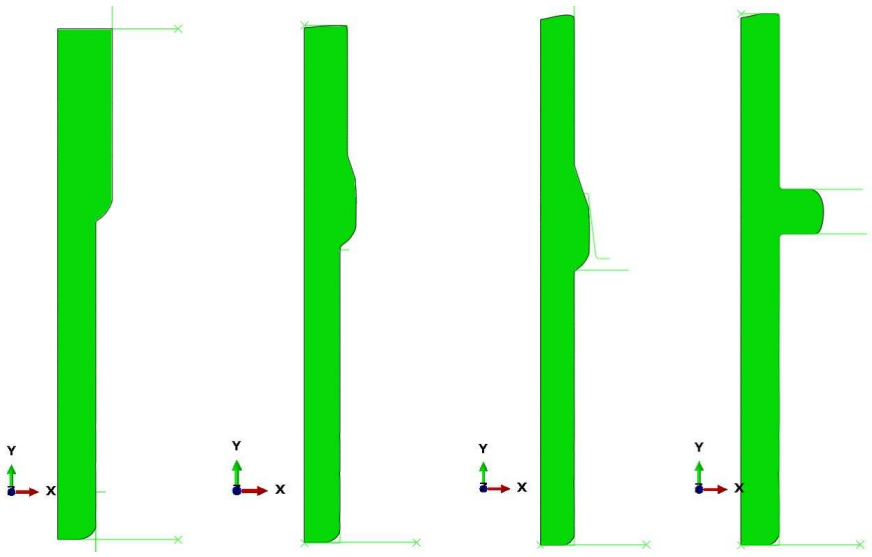

Fig. 4.4.1: The steps in manufacturing process

is taken as damage parameter for analyses. Fig.(4.4.2) describes the prediction of damage variables of various damage models. It can be seen that most damage models predict the location of higher damage in the upper portion of the shaft, where typically chevron cracks can form. But, this was not observed during the manufacturing process. VAR model predicts maximum damage on the circumferential surface of the flange, in line to manufacturing observations.

Since the top portion of shaft is crucial, the void volume fraction at the end of

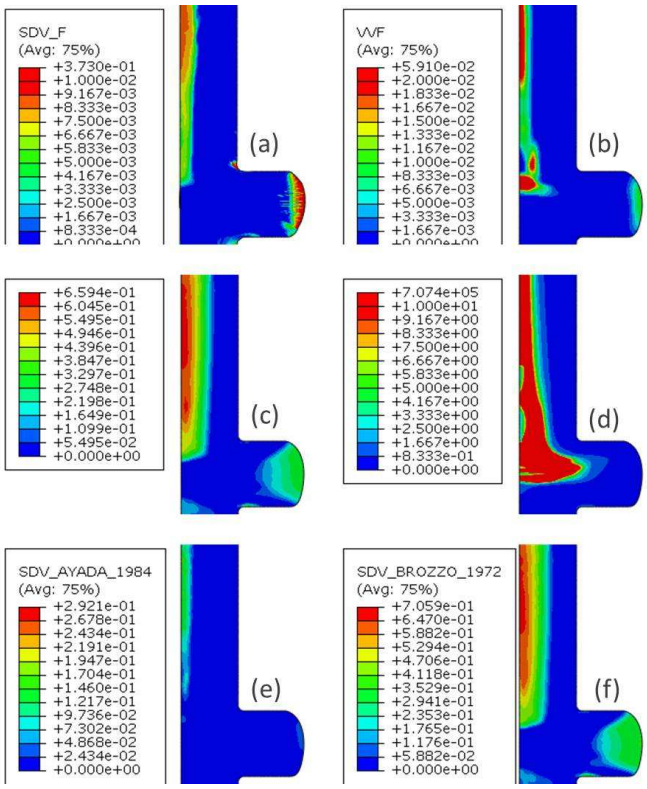

Fig. 4.4.2: a) void volume fraction of VAR model b) void volume fraction of Gurson model c) Cockroft Latham damage variable d) Rice and Tracy damage variable e) Ayada damage variable f)Brozzo damage variable

every step as obtained from VAR model is shown in Fig.(4.4.3). The void volume fraction starts increasing from Step-2 in the manufacturing process. But, the voids on the circumferential region nucleate in the last step.

The distribution of equivalent plastic strain and stress triaxiality is show in Fig.(4.4.4). It is evident that the stress triaxiality is higher in the flange region, which would facilitate void nucleation and hence increase damage.

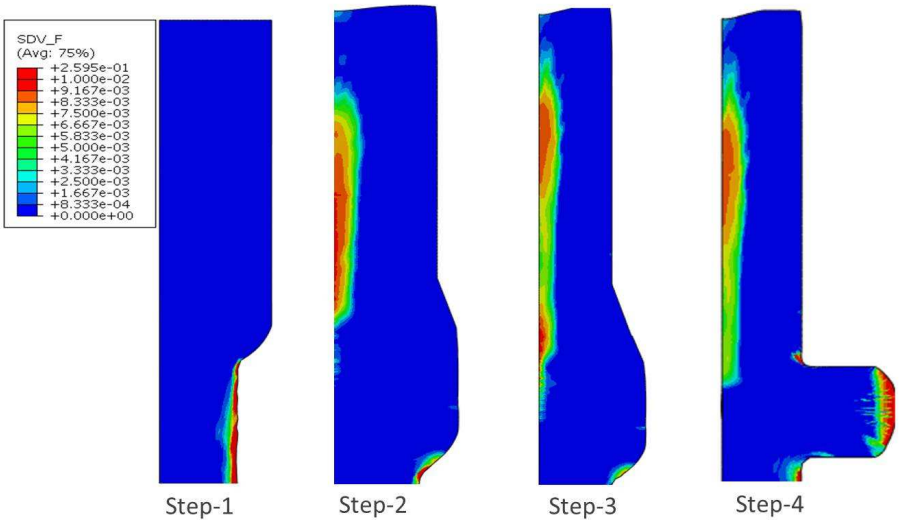

Fig. 4.4.3: Void Volume Fraction at the end each step as obtained from VAR model

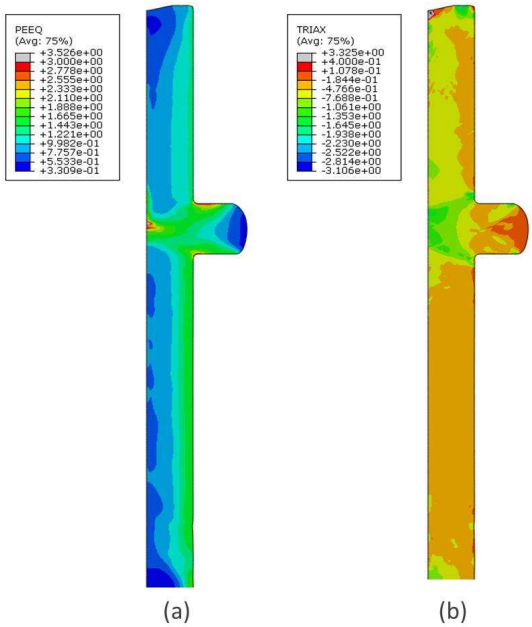

Fig. 4.4.4: a) Equivalent plastic strain b) Stress triaxiality

Chapter 5

Conclusion and future work

5.1 Conclusion

The primary focus of this thesis work was to simulate ductile damage in forming processes using micromechanically motivate VAR model proposed by Ponte Castañeda et. al. [42]. The first part of the work dealt with validation of VUMAT subroutine for forming simulations of materials with very low initial porosity.

Element closure phenomenon and non convergence of cutting plane algorithm were encountered when the subroutine was used for large plastic deformation simulations. The element closure phenomenon was linked to the calculation of Eshelby tensors. As discussed in Section 2.9.1, the element closure phenomenon could be resolved by limiting the evolution of voids once $f = 1 \times 10^{-4}$ and the evolution aspect ratios outside the bounds $10^{-2} < w < 10^{2}$. The latter issue of divergence of cutting plane algorithm was due to indeterminate numerical solutions. When any of the aspect ratios are equal to each other or equal to 1, the plastic spin tensor $\boldsymbol{W}^p$ becomes indeterminate. As proposed by Aravas [4], the spin tensor $\boldsymbol{W}^p$ is set to zero when the difference between any two aspect ratios is less than 10^{-2}. Also, the when the voids are spherical, the derived yield function in Section 2.8.2 is hard coded. These changes collectively could resolve the divergence of cutting plane algorithm. The revised subroutine was used to simulate a plane strain extrusion example described in Kailasam and Ponte Castañeda [42], and the obtained results were in agreement with the literature results. This assures that the modification does not alter the VAR constitutive equation.

The revised subroutine was further extended. Various isotropic hardening laws, namely - Swift Law, Hockett-Sherby hardening law, and a combination of Hockett-Sherby and Ghosh hardening law were coupled to the constitutive equation. Thomason coalescence criteria and Benzerga coalescence criteria were also implemented. The idea was to test the existing coalescence criteria for VAR model, as it has been seldom attended to in the literature. Also, to predict better void nucleation in negative triaxiality applications (upsetting test), the equivalent plastic strain in void nucleation function was replaced by a new nucleation plastic strain which accumulates only when triaxiality is positive. This modification improved the void

nucleation and the efficiency of the model in negative stress triaxiality regime.

The second part of the thesis work was to use the VAR model to simulate bulk forming experiments (uniaxial tensile test, upsetting test and cylinder with notch upsetting test) and an industrial example to understand the material model behaviour and its advantages over other damage models. Steel 20MnCr5-GKZ material was extensively studied at Fraunhofer IWM and hence this material was used for analysis. The flow curve of this material was obtained from Uniaxial tensile test upto a strain of 0.2 and upsetting test for strains 0.2-1.5. It was determined that the combination of Hockett-Sherby and Ghosh hardening law provided the best fit to the experimentally obtained flow curve.

Certain parameters of VAR model were taken from literature, and the void nucleation parameters were obtained by fitting the numerical stress-strain curve to experimental stress-strain curve of uniaxial tensile test of a round bar. For all simulations, the voids were initially assumed to be spherical, and $\boldsymbol{n}^{(3)}$ axis of the equivalent ellipsoidal void was assumed to be aligned to the direction of maximum load. Also, the parameters of Gurson model were identified using similar procedure.

The yield surfaces of VAR model and Gurson model in $\sigma_m - \sigma_{eq}$ plane was studied. In case of VAR model, the yield surface were wider for pure hydrostatic cases and seemed to deviate from the analytical spherical shell solution as opposed to Gurson model. Also, it was determined that the hyperbolic cosine term in Gurson yield function contributes to the exact solution at high stress triaxialities. The influence of initial void volume fraction on the yield surface was also studied. As expected the yield surface shrinks for higher void volume fraction, which signifies the loss of stress carrying capacity of the material.

The evolution of void volume fraction in case of uniaxial tensile load ($T = 1/3$) and hydrostatic tensile load ($T = \infty$) was understood from single element simulations. The void growth in Gurson model was larger in comparison to VAR model. In case of uniaxial tensile load, the results obtained from VAR model are more realistic. However, at high stress triaxiality the VAR model was much stiffer. Also, the influence of initial void shape on void growth was studied for a stress triaxiality of $T = 1/3$. In this stress triaxiality region, oblate voids grow much larger than other void shapes. The evolution of void shape i.e. the aspect ratios w_1 and w_2, at different triaxiality was studied and the obtained results were found to be intuitively realistic. Under uniaxial tensile load and biaxial compression load, initially spherical voids grow to take the prolate shape, and under uniaxial compression and biaxial tension, the voids took oblate shape. In pure hydrostatic case, the voids grow spherically i.e. the aspect ratios remain constant and equal to one. Also, the influence of void nucleation parameters on stress-strain curve and the behaviour of coalescence criteria with equivalent plastic strain and void aspect ratios were scrutinized in Chapter 3. Nucleation parameter f_N influenced the drop of the stress-strain curve after maximum load, and ε_N shifted the maximum stress location to left.

In Chapter 4, the results obtained from VAR model were compared to other damage models for practical experiments and manufacturing example. The numerical results obtained were in agreement with the experimental results. The shape of the deformed body, the von Mises stress profile, equivalent plastic strain profile, stress triaxiality profile and the distribution of void volume fraction demonstrate the correctness of the simulations and its applicability. It was also shown that, apart from void volume fraction, VAR model gives more details about the shape of the voids. In uniaxial tensile test damage is predicted at center of the specimen, in upsetting test at the surface in the center and in notched cylinder test at the center of notch. The damage location obtained from Gurson model and other phenomenological damage models agreed closely to VAR model and to experimental observations. It is to be noted that for these simple experiments, all damage models provide good results. However, in the simulation of Shaft with flange, VAR model predicted the damage location to be on the surface of the flange and other models predicted along the axis of the shaft. VAR model agreed closely to the experimental results. However, it will be premature to conclude that VAR model is most accurate with just one example.

The VAR model provides more details about the evolution of voids, its orientation and shape which is an important information to determine the anisotropy of the material after forming. However, due to high computation cost, the complexity of the constitutive equation and deviation of VAR model results at high stress triaxiality, raises questions about its applicability. Also, unavailability of a tested coalescence criterion which considers void rotation for 3-dimensional applications is a drawback. The VAR model also requires identification of more mircostructure parameters, in comparison to Gurson model. These parameters are difficult to identify using experiments. Based on VAR model, various other models [MVAR model (Danas and Aravas [25]), GVAR model (Cao et. al [14]) , Second order homogenization model (Ponte Castañeda et. al.)] are proposed in the literature which gives better results for pure hydrostatic loading conditions.

5.2 Future Work

1. The computation cost of VUMAT subroutine can be improved by using explicit equations proposed by Aravas and Ponte Castañeda [4] for calculation of Eshelby tensors.

2. The VAR model can be modified to account for changes proposed by Danas and Aravas [25] to improve its accuracy at high stress triaxiality.

3. A need arises to study the coalescence criteria, and develop a new criterion which considers void shapes and void rotation appropriately.

Appendices

Appendix A

Cutting Plane Algorithm [55]

Numerical solution of a rate independent elasto-plastic constitutive relation is based on an iterative solution of discretized form of balance of momentum equations. In the context of finite element analysis, consideration at two different levels are required - the global level and the material level. Typically the following steps are involved in the computation [59],

1) The discretized momentum equations generate incremental motion , which are used to calculate the incremental strain history using kinematic relations. This step occurs at the global level.

2) For the computed incremental strain history, new values for the incremental stress vector $\Delta\boldsymbol{\sigma}$ is obtained by integrating constitutive equation at each material point. The consistency condition (plasticity relations) are to be satisfied at the material level.

3) With the computed stresses, a check for violation of equilibrium condition is carried out. If violated, the iteration process continues by returning to step 1.

Step **2** is regarded as the central problem of computational plasticity and is a strain driven process, i.e., the state variables are computed for a given deformation history. Exact integration of the constitutive equations is possible in some cases of perfect plasticity, however most plasticity models require a numerical method [3]. The earlier numerical methods employed to calculate the incremental stress caused the final stress to gradually drift away from the yield surface, which necessitated a method to bring back the stresses to yield surface.
A powerful class of algorithms which accomplish this are the return mapping algorithms, also known as elastic predictor-plastic corrector algorithms. Pioneering work in this regard was published by Wilkins [67] who proposed the radial return algorithm for J2 plasticity. Most of the algorithms in return mapping class are particular cases of the trapezoidal and midpoint rules, which are generalized to satisfy the plastic consistency condition [54].Ortiz and Simo [55] pointed out that the scope of proposed methodologies by large are restricted to simple plasticity models and to constant isotropic elastic moduli. And, it also involves evaluation of the gradients of plastic flow direction, the normal to the yield surface, the plastic moduli and the elasticity tensor. The evaluation of these gradients are computationally expensive

and are best avoided.

Ortiz and Simo proposed an algorithm, known as cutting plane algorithm (CPA), within the framework of the operator splitting methodology, where the constitutve evolution equation are split into two parts - elastic and plastic. CPA is applicable to a general class of plastic and viscoplastic constitutive models exhibiting non-associative plastic flow, arbitrary yield criteria and hardening laws, and does not require the evaluation of gradients. The drawback of CPA is the difficulty in computing the consistent tangent operator. When the derivation of the gradients are complicated, CPA is a good choice. Also, when sufficiently small time steps are used, the accuracy and convergence of CPA are claimed to be higher.

The elastic part of the constitutive equation is first integrated to obtain the elastic predictor, which is taken as initial condition for the plastic equations. The stress trajectories during the return mapping phase should follow the steepest descent path corresponding to the yield function. In CPA, the relaxation process for stresses and plastic variables are carried out in a step-by-step fashion by linearizing the yield function around the current values of the state variables. The linearized yield function defines a straight intersection or a cut with the plane $\Phi = 0$ onto which the stress and plastic variables are projected to define the next iteration - hence the name *'Cutting Plane'*.

Since the constitutive model discussed in this study assumes associative flow rule with isotropic hardening, here a generic outline of the CPA for rate independent, associative elastoplastic material is described. The material can be characterized by the following set of constitutive equations,

$$\boldsymbol{\varepsilon} = \boldsymbol{\varepsilon^e} + \boldsymbol{\varepsilon^p} \tag{A.0.1}$$

$$\boldsymbol{\sigma} = \boldsymbol{\sigma}(\boldsymbol{\varepsilon^e}, \mathbf{q}) \tag{A.0.2}$$

$$\dot{\boldsymbol{\varepsilon}}^p = \dot{\Lambda}\mathbf{N}(\boldsymbol{\sigma}, \mathbf{q}) = \dot{\Lambda}\frac{\partial \Phi}{\partial \boldsymbol{\sigma}} \tag{A.0.3}$$

$$\dot{\boldsymbol{q}} = \dot{\Lambda}\mathbf{g}(\boldsymbol{\sigma}, \mathbf{q}) \tag{A.0.4}$$

$\boldsymbol{\varepsilon}$, $\boldsymbol{\varepsilon^e}$ and $\boldsymbol{\varepsilon^p}$ represent the total, elastic and plastic strain tensors, $\boldsymbol{\sigma}$ the Cauchy stress tensor, $\mathbf{q}$ is a set of plastic variable and $\dot{\boldsymbol{q}}$ is the evolution equation of plastic variables. Also, $\mathbf{N}$ is plastic flow direction and $\dot{\Lambda}$ is the plastic multiplier which is determined for the Kuhn-Tucker condition,

$$\Phi(\boldsymbol{\sigma}, \boldsymbol{q}) \leq 0 \qquad , \qquad \dot{\Lambda} \geq 0 \qquad , \qquad \Phi\dot{\Lambda} = 0 \tag{A.0.5}$$

Rephrasing Eq.(A.0.1) and Eq. (A.0.2) in rate form,

$$\dot{\boldsymbol{\varepsilon}} = \dot{\boldsymbol{\varepsilon}}^e + \dot{\boldsymbol{\varepsilon}}^p \tag{A.0.6}$$

$$\dot{\boldsymbol{\sigma}} = \boldsymbol{C}(\dot{\boldsymbol{\varepsilon}} - \dot{\boldsymbol{\varepsilon}}^p) \tag{A.0.7}$$

The constitutive equation can now be additively decomposed in to elastic and plastic part. The elastic part is deformation driven and is given by,

$$\dot{\boldsymbol{\varepsilon}} = \dot{\hat{\boldsymbol{\varepsilon}}} \tag{A.0.8a}$$

$$\dot{\boldsymbol{\sigma}} = \boldsymbol{C} : \dot{\boldsymbol{\varepsilon}} \tag{A.0.8b}$$

$$\dot{\boldsymbol{\varepsilon}}^p = 0 \tag{A.0.8c}$$

$$\dot{\boldsymbol{q}} = 0 \tag{A.0.8d}$$

And the plastic set of equations,

$$\dot{\boldsymbol{\varepsilon}} = 0 \tag{A.0.9a}$$

$$\dot{\boldsymbol{\sigma}} = -\boldsymbol{C} : \dot{\boldsymbol{\varepsilon}}^p \tag{A.0.9b}$$

$$\dot{\boldsymbol{\varepsilon}}^p = \dot{\Lambda}\mathbf{N} \tag{A.0.9c}$$

$$\dot{\boldsymbol{q}} = \dot{\Lambda}\mathbf{g} \tag{A.0.9d}$$

Substituting Eq. (A.0.9c) in Eq. (A.0.9b), one obtains,

$$\dot{\boldsymbol{\sigma}} = -\dot{\Lambda}\boldsymbol{C} : \mathbf{N} \tag{A.0.10}$$

Diving Eq. (A.0.10) and Eq. (A.0.9d) by $\dot{\Lambda}$,

$$\frac{d\boldsymbol{\sigma}}{d\Lambda} = -\boldsymbol{C} : \mathbf{N} \tag{A.0.11a}$$

$$\frac{d\boldsymbol{q}}{d\Lambda} = \mathbf{g} \tag{A.0.11b}$$

Eq. (A.0.11) defines a set of rate-independent relaxation equation which directs the

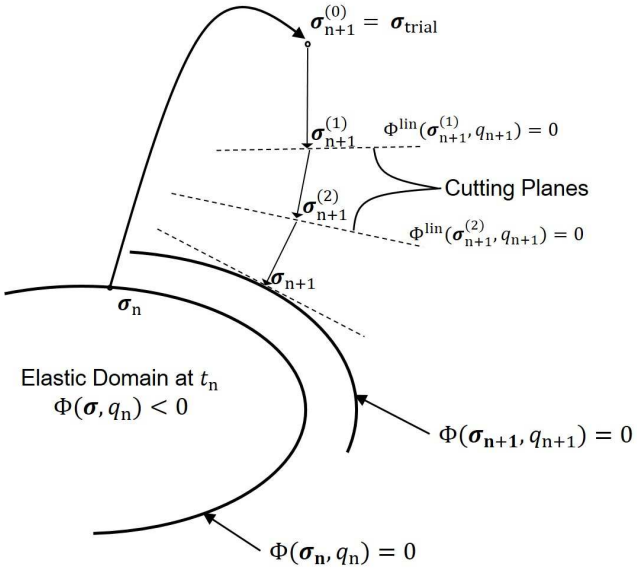

Fig. A.0.1: Geometric interpretation of cutting plane algorithm [55]

stress trajectories to follow the steepest descent paths corresponding to the yield

surface. Figure (A.0.1) shows the geometric interpretation of the cutting plane algorithm. In elastic equations (Eq. A.0.8), the inelastic response of the material is frozen, i.e., the plastic strains and the internal variables are taken to remain unchanged and all the prescribed deformation rate $\dot{\hat{\boldsymbol{\varepsilon}}}$ is assumed to strain the material elastically. In this scenario the elastic equations are directly integrable and the stresses are simply given by the elastic relation, while plastic strains and internal variables remain identically equal to their respective initial values. The yield function Φ is linearized around the current values of the state variables $\boldsymbol{\sigma}_{n+1}^{(i)}$, $\boldsymbol{q}_{n+1}^{(i)}$, to obtain,

$$\Phi_{n+1}^{(i+1)} \approx \Phi_{n+1}^{(i)} + \frac{\partial \Phi_{n+1}^{(i)}}{\partial \boldsymbol{\sigma}_{n+1}^{(i)}} : (\boldsymbol{\sigma}_{n+1}^{(i+1)} - \boldsymbol{\sigma}_{n+1}^{(i)}) + \frac{\partial \Phi_{n+1}^{(i)}}{\partial \boldsymbol{q}_{n+1}^{(i)}} . (\boldsymbol{q}_{n+1}^{(i+1)} - \boldsymbol{q}_{n+1}^{(i)}) \tag{A.0.12}$$

The discretized form of relaxation equations Eq. (A.0.11) in terms of incremental plastic multiplier $\Delta\Lambda$ is given as follows:

$$\boldsymbol{\sigma}_{n+1}^{(i+1)} - \boldsymbol{\sigma}_{n+1}^{(i)} = -\Delta\Lambda(\boldsymbol{C}_{n+1}^{(i)} : \boldsymbol{N}_{n+1}^{(i)}) \tag{A.0.13a}$$

$$\boldsymbol{q}_{n+1}^{(i+1)} - \boldsymbol{q}_{n+1}^{(i)} = \Delta\Lambda \boldsymbol{g}_{n+1}^{(i)} \tag{A.0.13b}$$

Substituting Eq. (A.0.13) in Eq. (A.0.12) and equating $\Phi_{n+1}^{(i+1)}$ to 0, gives the plastic increment multiplier $\Delta\Lambda$ as,

$$\Delta\Lambda = \frac{\Phi_{n+1}^{(i)}}{\boldsymbol{N}_{n+1}^{(i)} : \boldsymbol{C}_{n+1}^{(i)} : \boldsymbol{N}_{n+1}^{(i)} - \dfrac{\partial \Phi_{n+1}^{(i)}}{\partial \boldsymbol{q}_{n+1}^{(i)}} . \boldsymbol{g}_{n+1}^{(i)}} \tag{A.0.14}$$

The iteration continues until the plastic consistency is restored within a prescribed tolerance.

Algorithm 1 Cutting Plane Algorithm [55]

1: **Geometric Update:**

$$\boldsymbol{\varepsilon}_{n+1} = \boldsymbol{\varepsilon}_n + \nabla^s \boldsymbol{u}$$

2: **Elastic Predictor:**

$$\boldsymbol{\varepsilon}^{p(0)}_{n+1} = \boldsymbol{\varepsilon}^p_n$$

$$\boldsymbol{\varepsilon}^{e(0)}_{n+1} = \boldsymbol{\varepsilon}_{n+1} - \boldsymbol{\varepsilon}^{p(0)}_{n+1}$$

$$\boldsymbol{q}^{(0)}_{n+1} = \boldsymbol{q}_n$$

$$\boldsymbol{\sigma}^{(0)}_{n+1} = \boldsymbol{\sigma}(\boldsymbol{\varepsilon}^{e(0)}_{n+1}, \boldsymbol{q}^{(0)}_{n+1})$$

3: **Check for yielding:**

$$\textbf{if} \quad \Phi^{(0)}_{n+1} \leq 0$$

$$\textbf{then} \quad \boldsymbol{\varepsilon}^p_{n+1} = \boldsymbol{\varepsilon}^{p(0)}_{n+1}; \boldsymbol{\varepsilon}^e_{n+1} = \boldsymbol{\varepsilon}^{e(0)}_{n+1}; \boldsymbol{\sigma}_{n+1} = \boldsymbol{\sigma}^0_{n+1}; \boldsymbol{q}_{n+1} = \boldsymbol{q}^{(0)}_{n+1}; \textbf{exit}$$

$$\textbf{else} \quad i = 0$$

4: **Plastic correctors:**

$$\Delta\Lambda = \frac{\Phi^{(i)}_{n+1}}{\boldsymbol{N}^{(i)}_{n+1} : \boldsymbol{C}^{(i)}_{n+1} : \boldsymbol{N}^{(i)}_{n+1} - \frac{\partial \Phi^{(i)}_{n+1}}{\partial \boldsymbol{q}^{(i)}_{n+1}} . \boldsymbol{g}^{(i)}_{n+1}}$$

$$\boldsymbol{\sigma}^{(i+1)}_{n+1} = \boldsymbol{\sigma}^{(i)}_{n+1} - \Delta\Lambda(\boldsymbol{C}^{(i)}_{n+1} : \boldsymbol{N}^{(i)}_{n+1})$$

$$\boldsymbol{q}^{(i+1)}_{n+1} = \boldsymbol{q}^{(i)}_{n+1} + \Delta\Lambda \boldsymbol{g}^{(i)}_{n+1}$$

5: **Convergence check:**

$$\textbf{if} \quad |\Phi^{(i+1)}_{n+1}| \leq \textbf{TOL}|\Phi^{(0)}_{n+1}|$$

$$\textbf{then} \quad \boldsymbol{\sigma}_{n+1} = \boldsymbol{\sigma}^{i+1}_{n+1}; \boldsymbol{q}_{n+1} = \boldsymbol{q}^{(i+1)}_{n+1}; \boldsymbol{\varepsilon}^e_{n+1} = \boldsymbol{\varepsilon}^e(\boldsymbol{\sigma}_{n+1}, \boldsymbol{q}_{n+1}); \quad \boldsymbol{\varepsilon}^p_{n+1} = \boldsymbol{\varepsilon}_{n+1} - \boldsymbol{\varepsilon}^e_{n+1};$$

$$\textbf{else} \quad i = i + 1; \qquad \textbf{Go To step (4)}$$

Bibliography

[1] Failure Mechanism. http://www.slideshare.net/dhyun/ch9-failure-mechanisms. Accessed: 2015-12-27.

[2] Mechanics. *Lecture Notes, Facutly of Engineering - Engineering Science, The University of Auckland, New Zealand.*

[3] Annalingam Anandarajah. *Computational methods in elasticity and plasticity: solids and porous media.* Springer Science & Business Media, 2011.

[4] N Aravas and P Ponte Castañeda. Numerical methods for porous metals with deformation-induced anisotropy. *Computer methods in applied mechanics and engineering*, 193(36):3767–3805, 2004.

[5] AS Argon, J Im, and R Safoglu. Cavity formation from inclusions in ductile fracture. *Metallurgical Transactions A*, 6(4):825–837, 1975.

[6] Laurent Babout, Yves Brechet, Eric Maire, and Roger Fougeres. On the competition between particle fracture and particle decohesion in metal matrix composites. *Acta materialia*, 52(15):4517–4525, 2004.

[7] Yingbin Bao and Tomasz Wierzbicki. On fracture locus in the equivalent strain and stress triaxiality space. *International Journal of Mechanical Sciences*, 46(1):81–98, 2004.

[8] SC Baxter. Micromechanics of random heterogeneous materials. *equilibrium*, 3:1–7, 2004.

[9] AA Benzerga. Micromechanics of coalescence in ductile fracture. *Journal of the Mechanics and Physics of Solids*, 50(6):1331–1362, 2002.

[10] AAmine Benzerga and Jean-Baptiste Leblond. Ductile fracture by void growth to coalescence. *Advances in Applied Mechanics*, 44:169–305, 2010.

[11] Prof. Dr.-Ing. Joachim Bluhm. Continuum mechanics. *Lecture Notes, Institute of Mechanics, Universität Duisburg-Essen, Germany.*

[12] Pierre-Olivier Bouchard, Ludovic Bourgeon, Sebastien Fayolle, and Katia Mocellin. An enhanced lemaitre model formulation for materials processing damage computation. *International Journal of Material Forming*, 4(3):299–315, 2011.

[13] Prof. Allan F Bower. Applied mechanics of solids.

[14] T-S Cao, M Mazière, K Danas, and J Besson. A model for ductile damage prediction at low stress triaxialities incorporating void shape change and void rotation. *International Journal of Solids and Structures*, 63:240–263, 2015.

[15] Trong Son Cao. Models for ductile damage and fracture prediction in cold bulk metal forming processes: a review. *International Journal of Material Forming*, pages 1–33, 2015.

[16] P Ponte Castañeda. The effective mechanical properties of nonlinear isotropic composites. *Journal of the Mechanics and Physics of Solids*, 39(1):45–71, 1991.

[17] P Ponte Castañeda. New variational principles in plasticity and their application to composite materials. *Journal of the Mechanics and Physics of Solids*, 40(8):1757–1788, 1992.

[18] P Ponte Castañeda and JOHN R Willis. The effect of spatial distribution on the effective behavior of composite materials and cracked media. *Journal of the Mechanics and Physics of Solids*, 43(12):1919–1951, 1995.

[19] P Ponte Castañeda and M Zaidman. Constitutive models for porous materials with evolving microstructure. *Journal of the Mechanics and Physics of Solids*, 42(9):1459–1497, 1994.

[20] JL Chaboche. Anisotropic creep damage in the framework of continuum damage mechanics. *Nuclear engineering and design*, 79(3):309–319, 1984.

[21] J Chambert, Ph Bressolette, and A Vergne. Implementation of coalescence criteria into the gtn model application to work-hardening ductile materials. In *ECF13, San Sebastian 2000*, 2013.

[22] Zengtao Chen and Cliff Butcher. *Micromechanics modelling of ductile fracture*. Springer, 2013.

[23] CC Chu and A Needleman. Void nucleation effects in biaxially stretched sheets. *Journal of Engineering Materials and Technology*, 102(3):249–256, 1980.

[24] MG Cockcroft and DJ Latham. Ductility and the workability of metals. *J Inst Metals*, 96(1):33–39, 1968.

[25] Kostas Danas and N Aravas. Numerical modeling of elasto-plastic porous materials with void shape effects at finite deformations. *Composites Part B - Engineering*, 43(6):2544–2559, 2012.

[26] Kostas Danas and P Ponte Castañeda. A finite-strain model for anisotropic viscoplastic porous media: I–theory. *European Journal of Mechanics-A/Solids*, 28(3):387–401, 2009.

[27] Eduardo A de Souza Neto, Djordje Peric, and David Roger Jones Owen. *Computational methods for plasticity: theory and applications*. John Wiley & Sons, 2011.

[28] EN DIN. 10084 einsatzstähle–technische lieferbedingungen. *Ausg. Juni*, 1998.

[29] Dr.Dominik Brands Dr. Daniel Balzani. Effective properties of micro-heterogeneous materials. *Lecture Notes,Institute of Mechanics, University of Duisburg Essen, Germany*, 2014.

[30] Matthieu Dunand and Dirk Mohr. On the predictive capabilities of the shear modified gurson and the modified mohr–coulomb fracture models over a wide range of stress triaxialities and lode angles. *Journal of the Mechanics and Physics of Solids*, 59(7):1374–1394, 2011.

[31] JOHN D Eshelby. The determination of the elastic field of an ellipsoidal inclusion, and related problems. In *Proceedings of the Royal Society of London A: Mathematical, Physical and Engineering Sciences*, volume 241, pages 376–396. The Royal Society, 1957.

[32] Jonas Faleskog, Xiaosheng Gao, and C Fong Shih. Cell model for nonlinear fracture analysis–i. micromechanics calibration. *International Journal of Fracture*, 89(4):355–373, 1998.

[33] Mihai Gologanu, Jean-Baptiste Leblond, and Josette Devaux. Approximate models for ductile metals containing non-spherical voids:case of axisymmetric prolate ellipsoidal cavities. *Journal of the Mechanics and Physics of Solids*, 41(11):1723–1754, 1993.

[34] Mihai Gologanu, Jean-Baptiste Leblond, and Josette Devaux. Approximate models for ductile metals containing nonspherical voids:case of axisymmetric oblate ellipsoidal cavities. *Journal of Engineering Materials and Technology*, 116(3):290–297, 1994.

[35] Dietmar Gross and Thomas Seelig. *Fracture mechanics: with an introduction to micromechanics*. Springer Science & Business Media, 2011.

[36] John Gurland and J Plateau. The mechanism of ductile rupture of metals containing inclusions. Technical report, Brown Univ., Providence; Institut de Recherches de la Siderugie, St.-Germain-en-Laye, France, 1963.

[37] Joseph Gurland. Observations on the fracture of cementite particles in a spheroidized 1.05% c steel deformed at room temperature. *Acta Metallurgica*, 20(5):735–741, 1972.

[38] Arthur L Gurson. Continuum theory of ductile rupture by void nucleation and growth part i :yield criteria and flow rules for porous ductile media. *Journal of engineering materials and technology*, 99(1):2–15, 1977.

[39] RODNEY Hill. Continuum micro-mechanics of elastoplastic polycrystals. *Journal of the Mechanics and Physics of Solids*, 13(2):89–101, 1965.

[40] Rodney Hill. *The mathematical theory of plasticity*, volume 11. Oxford university press, 1998.

[41] Gordon R Johnson and William H Cook. Fracture characteristics of three metals subjected to various strains, strain rates, temperatures and pressures. *Engineering fracture mechanics*, 21(1):31–48, 1985.

[42] M Kailasam, N Aravas, and P Ponte Castañeda. Porous metals with developing anisotropy: Constitutive models, computational issues and applications to deformation processing. *CMES: Computer Modeling in Engineering & Sciences*, 1(2):105–118, 2000.

[43] M Kailasam and P Ponte Castañeda. A general constitutive theory for linear and nonlinear particulate media with microstructure evolution. *Journal of the Mechanics and Physics of Solids*, 46(3):427–465, 1998.

[44] N Kanetake, M Nomura, and T Choh. Continuous observation of microstructural degradation during tensile loading of particle reinforced aluminium matrix composites. *Materials science and technology*, 11(12):1246–1252, 1995.

[45] Srihari Kurukuri and Dipl-Ing S Eckardt. A review of homogenization techniques for heterogeneous materials. *Term paper. Advanced Mechanics of Materials and Structures, Graduate School in Structural Engineering, Germany*, 2004.

[46] S Kut. State of stress identification in numerical modeling of 3d issues. *Archives of Metallurgy and Materials*, 54:627–632, 2009.

[47] Jean Lemaitre. Coupled elasto-plasticity and damage constitutive equations. *Computer Methods in Applied Mechanics and Engineering*, 51(1):31–49, 1985.

[48] Jean Lemaitre. Local approach of fracture. *Engineering Fracture Mechanics*, 25(5):523–537, 1986.

[49] Frank A McClintock. A criterion for ductile fracture by the growth of holes. *Journal of applied mechanics*, 35(2):363–371, 1968.

[50] Frank A McClintock, Saul M Kaplan, and Charles A Berg. Ductile fracture by hole growth in shear bands. *International Journal of Fracture Mechanics*, 2(4):614–627, 1966.

[51] K Nahshon and JW Hutchinson. Modification of the gurson model for shear failure. *European Journal of Mechanics-A/Solids*, 27(1):1–17, 2008.

[52] A Needleman and JR Rice. *Limits to ductility set by plastic flow localization*. Springer, 1978.

[53] Kim L Nielsen, Jonas Dahl, and Viggo Tvergaard. Collapse and coalescence of spherical voids subject to intense shearing: studied in full 3d. *International journal of fracture*, pages 1–12, 2012.

[54] M Ortiz and Egor Paul Popov. Accuracy and stability of integration algorithms for elastoplastic constitutive relations. *International Journal for Numerical Methods in Engineering*, 21(9):1561–1576, 1985.

[55] M Ortiz and JC Simo. An analysis of a new class of integration algorithms for elastoplastic constitutive relations. *International Journal for Numerical Methods in Engineering*, 23(3):353–366, 1986.

[56] Thomas Pardoen and JW Hutchinson. An extended model for void growth and coalescence. *Journal of the Mechanics and Physics of Solids*, 48(12):2467–2512, 2000.

[57] J R Rice and Dennis Michael Tracey. On the ductile enlargement of voids in triaxial stress fields. *Journal of the Mechanics and Physics of Solids*, 17(3):201–217, 1969.

[58] F Scheyvaerts, PR Onck, Cihan Tekoglu, and Thomas Pardoen. The growth and coalescence of ellipsoidal voids in plane strain under combined shear and tension. *Journal of the Mechanics and Physics of Solids*, 59(2):373–397, 2011.

[59] Juan C Simo and Thomas JR Hughes. *Computational inelasticity*, volume 7. Springer Science & Business Media, 2006.

[60] PF Thomason. Three-dimensional models for the plastic limit-loads at incipient failure of the intervoid matrix in ductile porous solids. *Acta Metallurgica*, 33(6):1079–1085, 1985.

[61] PF Thomason. A view on ductile-fracture modelling. *Fatigue & Fracture of Engineering Materials & Structures*, 21(9):1105–1122, 1998.

[62] Viggo Tvergaard. Influence of voids on shear band instabilities under plane strain conditions. *International Journal of Fracture*, 17(4):389–407, 1981.

[63] Viggo Tvergaard and Alan Needleman. Analysis of the cup-cone fracture in a round tensile bar. *Acta metallurgica*, 32(1):157–169, 1984.

[64] ABAQUS Version. 6.7 user manual. *Inc. and Dassault systemes*, 2007.

[65] Arnaud G Weck. *The role of coalescence on ductile fracture*. 2007.

[66] Chris Weinberger, Wei Cai, and David Barnett. Lecture notes–elasticity of microscopic structures. 2005.

[67] Mark L Wilkins. Calculation of elastic-plastic flow. Technical report, DTIC Document, 1963.

[68] JR Willis. Bounds and self-consistent estimates for the overall properties of anisotropic composites. *Journal of the Mechanics and Physics of Solids*, 25(3):185–202, 1977.

[69] Liang Xue. Constitutive modeling of void shearing effect in ductile fracture of porous materials. *Engineering Fracture Mechanics*, 75(11):3343–3366, 2008.

[70] Fusahito Yoshida. Constitutive modeling of large-strain cyclic plasticity for anisotropic metals. *Lecture Notes, Department of Mechanical Science and Engineering Hiroshima University, JAPAN*.

[71] Jun Zhou, Xiaosheng Gao, James C Sobotka, Bryan A Webler, and Brian V Cockeram. On the extension of the gurson-type porous plasticity models for prediction of ductile fracture under shear-dominated conditions. *International Journal of Solids and Structures*, 51(18):3273–3291, 2014.